

1



2

Exploiting CVD diamond properties for particle detection and identification

3

4

5

Matevž Červ

6

Vienna University of Technology

7

A thesis submitted for the degree of

8

Doctor of technical sciences

9

Geneva 2016

¹⁰ Contents

¹¹ 1	Introduction	1
¹² 1.1	Fundamental research	2
¹³ 1.1.1	CERN	3
¹⁴ 1.1.2	Particle accelerators	4
¹⁵ 1.1.3	The ATLAS experiment	5
¹⁶ 1.1.4	Atominsttitut, Vienna	6
¹⁷ 1.1.5	n-ToF	7
¹⁸ 1.2	Particle detectors	8
¹⁹ 1.2.1	Semiconductor detectors	9
²⁰ 1.2.2	Diamond sensors	10
²¹ 2	Signal formation in diamond	13
²² 2.1	Principles of signal formation in semiconductors	14
²³ 2.1.1	Signal induction by moving charges	16
²⁴ 2.1.2	Radiation-induced electrical pulses	18
²⁵ 2.1.3	Signal charge fluctuations	19
²⁶ 2.2	Carrier transport in a diamond sensor	19
²⁷ 2.3	Electronics for signal processing	22
²⁸ 2.3.1	Signal preamplifiers	22
²⁹ 2.3.1.1	Current-sensitive amplifier	23
³⁰ 2.3.1.2	Charge-sensitive amplifier	24
³¹ 2.3.1.3	Analogue electronic noise	25
³² 2.3.2	Analogue-to-digital converters	25
³³ 2.3.3	Digital signal processing	26
³⁴ 3	Experimental results	
³⁵	<i>Diamond irradiation study</i>	28
³⁶ 3.1	Measurement setup	29
³⁷ 3.1.1	Preamplifiers	29
³⁸ 3.1.1.1	Calibration	30
³⁹ 3.1.2	Diamond samples	31
⁴⁰ 3.1.3	Readout devices	32
⁴¹ 3.1.4	Setup for the efficiency study using β particles	32
⁴² 3.1.5	Room temperature α -TCT setup	33

CONTENTS

43	3.1.6	Cryogenic α -TCT setup	33
44	3.2	Charged particle pulses and spectra	35
45	3.2.1	Noise limitations	35
46	3.3	Radiation limitations	37
47	3.3.1	Quantifying radiation damage in diamonds	38
48	3.3.1.1	Irradiation with a $\pi_{300 \text{ MeV}}$ beam	38
49	3.3.1.2	Charge collection efficiency and charge collection distance	39
50	3.3.1.3	Irradiation damage factor	40
52	3.3.2	Long-term measurement stability	41
53	3.3.2.1	β long-term stability	42
54	3.3.2.2	α long-term stability	43
55	3.4	Temperature limitations	47
56	3.4.1	Temperature-variant α -TCT before irradiation	49
57	3.4.2	Temperature-variant α -TCT after irradiation	51
58	3.4.2.1	Collected charge as a function of temperature	52
59	3.4.2.2	Charge trapping	54
60	3.5	Conclusion	58
61	4	Charge monitoring	
62		<i>The ATLAS Diamond Beam Monitor</i>	59
63	4.1	Luminosity measurements	60
64	4.2	Diamond pixel module	61
65	4.2.1	Sensors	62
66	4.2.2	Front-end electronics	63
67	4.3	Module assembly and quality control	65
68	4.3.1	Assembly	65
69	4.3.2	Testing	66
70	4.3.3	Installation and commissioning	67
71	4.4	Performance results	68
72	4.4.1	Source tests	68
73	4.4.2	Test beam results	69
74	4.5	Operation	72
75	4.5.1	Positioning	72
76	4.5.2	Data taking during collisions	73
77	4.6	Conclusion	76
78	5	Current monitoring	
79		<i>Real-time particle identification</i>	77
80	5.1	Motivation	78
81	5.2	Requirements	78
82	5.3	Device specifications	79
83	5.4	Pulse parameters	79

CONTENTS

84	5.5 Applications	81
85	5.6 Description of the firmware	82
86	5.6.1 Design constraints	82
87	5.6.2 Analysis module	83
88	5.6.3 Area and width measurement	85
89	5.6.3.1 Vector cleaning	86
90	5.6.3.2 Algorithm	87
91	5.7 Control and data interface	88
92	5.7.1 Software	89
93	5.7.2 Data readout	89
94	5.8 Performance results	90
95	5.8.1 Comparison between the charge- and current-sensitive spec-	
96	troscopy	91
97	5.9 Source calibration	94
98	5.9.1 Source measurements – scatter plots	96
99	5.9.1.1 ^{241}Am source	96
100	5.9.1.2 ^{90}Sr and ^{60}Co source	101
101	5.10 Applications in neutron instrumentation	105
102	5.10.1 Thermal neutron flux monitoring	105
103	5.10.1.1 Measurements	106
104	5.10.1.2 Results and discussion	107
105	5.10.1.3 Conclusion	107
106	5.10.2 Fusion power monitoring	107
107	5.10.2.1 Measurements	108
108	5.10.2.2 Results and discussion	109
109	5.10.2.3 Conclusion	109
110	5.10.3 Fast and thermal neutron monitoring	111
111	5.10.3.1 Measurements	111
112	5.10.3.2 Results and discussion	113
113	5.10.3.3 Conclusion	113
114	5.11 Conclusion	114

¹¹⁵ List of Figures

¹¹⁶ 1.1	Standard model [22]	3
¹¹⁷ 1.2	The Large Hadron Collider [20]	5
¹¹⁸ 1.3	The ATLAS Experiment [38]	6
¹¹⁹ 1.4	The TRIGA MARK II neutron reactor [15]	7
¹²⁰ 1.5	The calorimeter in the n-ToF area [19]	8
¹²¹ 1.6	The Insertable B-Layer – a silicon particle tracker installed in the ATLAS experiment in 2014 [34]	10
¹²² 1.7	A pCVD diamond pad detector [23]	11
¹²⁴ 2.1	In the equivalent electrical circuit diagram, electron-hole creation and drift can be modelled as a current source with a capacitor in parallel	15
¹²⁵ 2.2	Stopping power for muons according to the Bethe-Bloch formula []	16
¹²⁶ 2.3	A point-like charge inducing current in a conductive plane	17
¹²⁷ 2.4	Charge carrier drift in diamond for β/γ and for α particles	18
¹²⁸ 2.5	Calculated intrinsic energy resolution for silicon and diamond	20
¹²⁹ 2.6	Introduction of space charge in the diamond bulk. The induced current signal is proportional to the effective electrical field. d is the thickness of the diamond sensor.	21
¹³⁰ 2.7	Introduction of impurities and non-uniformities into the crystal lattice due to radiation damage.	22
¹³¹ 2.8	Simplified equivalent circuits of a current and charge amplifier	23
¹³² 2.9	Input and output signal of the current amplifier	24
¹³³ 2.10	Input and output signal of the charge amplifier	24
¹³⁴ 2.11	Input signal digitisation and quantisation error	26
¹³⁵ 2.12	An example of an FPGA and an ASIC chip	27
¹⁴⁰ 3.1	Diagram of a diamond detector readout chain.	29
¹⁴¹ 3.2	Amplifiers used for the charge and current measurements	30
¹⁴² 3.3	Two scCVD diamond samples: A IIa 1scdhq (left) and an E6 S37 (right)	31
¹⁴³ 3.4	Positioning of the α -source on top of the sensor carrier	34
¹⁴⁴ 3.5	Superimposed and averaged pulses (a, b and c, current amplifier) and distributions of deposited energy (d, e, f, charge amplifier) for three types of radiation. Note the scale on the X axis of the distributions. .	36

LIST OF FIGURES

147	3.6	Diamond radiation damage - a model based on displacements per atom [26]. Added are data points for protons and pions by RD42 [35] and one data point for pions measured in the scope of this thesis.	39
148	3.7	First figure shows the CCD for S37, S79 and S52 at a range of bias voltage settings. The charge collection distance at 1 V/ μm bias voltage for the three diamond samples is then compared to the RD42 data for pion irradiation in the second figure. The data points are about 15–25 % lower than expected from the RD42 data [35].	41
149	3.8	Relative increase of charge collection over time due to priming with the ^{90}Sr radioactive source. The bias voltage for this measurement is 1 V/ μm	43
150	3.9	Relative decrease of collected charge with time for non-irradiated and irradiated diamond samples.	44
151	3.10	The signal of the irradiated and primed S79 deteriorates with time for both polarities. Every plot contains 60 superimposed pulses.	45
152	3.11	Deterioration of the pulse shapes with time	46
153	3.12	Five procedures for the “healing” process for an irradiated diamond that was exposed to α radiation at bias voltage switched on for at least 30 minutes at a rate of 10^4 s^{-1}	48
154	3.13	Varied bias voltage at a fixed temperature	49
155	3.14	Several data points between 4 K and 295 K at a bias voltage of $\pm 500 \text{ V}$	50
156	3.15	Varied bias voltage at a fixed temperature for an irradiated sample .	52
157	3.16	After irradiation: several data points between 4 K and 295 K at a bias voltage of $\pm 500 \text{ V}$	53
158	3.17	Collected charge as a function of temperature	55
159	3.18	Charge carrier lifetime decreases with irradiation, but is stable across the range of temperatures between 4 K – 75 K and 150 K – 295 K. The first figure shows the carrier lifetime s a function of temperature whereas the second figure depcits the carrier lifetime averaged over all temperatures and plotted against the π irradiation dose	57
160	4.1	Diamond detectors installed in high-energy physics experiments in the last decade, sorted by the active sensor area. The first four detectors from the left are radiation monitors whereas the right two are pixel trackers.	60
161	4.2	DBM module, top-down view. Visible is the flexible PCB with signal and power connections, the silicon sensor and a part of the FE-I4. Wire bonds from the PCB to the FE-I4 and to the sensor are also visible. .	61
162	4.3	A pCVD wafer. The golden dots on the surface are the electrodes that are applied during the qualification test. The wafer is measured across the surface to find the regions with the highest efficiency.	62

LIST OF FIGURES

187	4.4	FE-I4 layout, top-down view. The pink area are pixels grouped into columns, the green area below is the common logic and the red strip at the bottom are the wire bond pads.	63
188	4.5	Schematic of an analog pixel. Courtesy of the FE-I4 collaboration. . .	64
189	4.6	Module production with time	67
190	4.7	Occupancy and pseudo-efficiency scans for the silicon (left) and diamond sensor (right) to check for disconnected regions and estimate the sensor's efficiency. Shadows of the electronic components are clearly visible because fewer electrons were able to traverse through such a higher amount of material.	70
191	4.8	Measurements of pseudo-efficiency and disconnected regions for all modules that went through the QC procedure	71
192	4.9	An efficiency study of a prototype DBM diamond module in a test beam. The statistics are low (~ 10 hits/pixel) as the data was collected during a short run.	71
193	4.10	This photo highlights four telescopes installed onto the nSQPs and around the pipe	72
194	4.11	Position of the DBM in the ATLAS experiment	73
195	4.12	Occupancy of individual modules during collisions. Only 16 modules were taking data.	74
196	4.13	A diagram showing the radial distance R_0 and longitudinal distance Z_0 of the trajectory from the interaction point at the minimal distance d . Z is the axis along the beam line. Three module planes intercept a particle and reconstruct its trajectory.	74
197	4.14	These two plots show two parameters of particle tracks recorded by one of the DBM telescopes: radial and longitudinal distance of the projected tracks from the interaction point.	75
198	5.1	A pulse and its parameters	80
199	5.2	Form Factor is the ratio between the measured area (a) and the calculated area ($A \times BW$) of the pulse. The calculated area is significantly larger than the measured area for a triangular triangular pulse, but less so for the rectangular one. The red and blue dot in the right plot are the value entries of the two pulses shown. The red and blue oval shapes depict the regions for the values expected from triangular and rectangular pulses. By carefully choosing the linear qualifier (dashed line) and taking only the entries below the cut rectangular pulses can be identified.	80
200	5.3	Firmware design structure	82
201	5.4	Code design plan	83

LIST OF FIGURES

226	5.5	A sample pulse. The first vector shows which samples are above the width measurement height. The second vector is a clean vector. The third line shows the position of the maximum amplitude. The vector cleaning algorithm starts from the maximum amplitude and continues in both ways along the vector.	86
227	5.6	This block counts the remaining binary ones in the clean vectors and outputs this value as the pulse width.	86
228	5.7	This block masks the input data with the clean vector and sums the remaining samples.	87
229	5.8	Vector cleaning routine outputs two vectors - one forward in time and one back in time from the peak of the pulse.	87
230	5.9	One logic step in the algorithm chain before and after Karnaugh minimisation.	88
231	5.10	Vector is divided into two 16-bit logic chains. The algorithm logic is then run on the two chains separately. The results are then merged into one 32-bit clean vector by using a set of AND gates.	88
232	5.11	Abstraction levels of the controller software	89
233	5.12	This figure shows the capability of the device to analyse all arriving pulses for a range of input frequencies. The highest achievable rate with zero lost pulses is 5×10^6 s $^{-1}$	91
234	5.13	These diagrams show the linearity of the measurements and their stability with respect to analog noise.	92
235	5.14	Spectrum of a $^{148}\text{Gd}^{239}\text{Pu}^{241}\text{Am}^{244}\text{Cm}$ source using a Cx and a C2 amplifier	93
236	5.15	Accumulated pulses for all runs	95
237	5.16	^{241}Am , e $^-$ collection. Qualifier: FWHM. Optional qualifiers: Amplitude, Form Factor.	98
238	5.17	^{241}Am , h $^+$ collection. Qualifier: FWHM.	99
239	5.18	^{241}Am area histograms for electron and hole collection.	100
240	5.19	^{90}Sr scatter plots	102
241	5.20	^{60}Co scatter plots	103
242	5.21	Energy distributions for γ and β particles.	104
243	5.22	Thermal neutrons, photons. Qualifier: FWHM.	107
244	5.23	Energy spectrum after applied qualifiers reveals the tritium and α peak	108
245	5.24	^{239}Pu Be. Qualifiers: BW-FWHM, FWHM, Form Factor	110
246	5.25	^{239}Pu Be, energy distribution of the neutrons interacting in the ballistic centre.	111
247	5.26	Fast neutrons, thermal neutrons, photons. Qualifiers: BW-FWHM, FWHM, Form factor, Slope.	112
248	5.27	Energy spectrum in CROCUS before and after applied qualifiers	113

LIST OF FIGURES

²⁶⁶ **Chapter 1**

²⁶⁷ **Introduction**

²⁶⁸ The aim of the thesis is to present and discuss applications of diamond based particle
²⁶⁹ detectors.

²⁷⁰ The introductory chapter paints a picture of the current state of particle physics
²⁷¹ research. It presents some of the research institutes that are active in this field,
²⁷² pushing the boundaries of human knowledge further. It explains their goals and the
²⁷³ means with which they are achieving them. Next section describes particle detectors
²⁷⁴ in a broad sense – their history and the types existing now. One type in particular –
²⁷⁵ a diamond detector – is then described more in detail.

²⁷⁶ Second chapter discusses the properties of diamond detectors. Dissecting the
²⁷⁷ detector chain into individual parts and describing them in detail – sensors, amplifiers,
²⁷⁸ digitisers and signal processing units. We learn about energy resolution in diamond,
²⁷⁹ analog and digital noise contribution etc. Principles of signal formation are presented,
²⁸⁰ starting with the famous Shockley-Ramo theorem and building from there. We will
²⁸¹ see that different types of radiation induce different electrical signals.

²⁸² The base laid down in the second chapter is complemented in the third where the
²⁸³ measurements are presented and the results discussed. The focus is on diamond's
²⁸⁴ measurement stability with respect to irradiation damage. To carry out this study,
²⁸⁵ two diamond sensors were irradiated to two different doses, with the measurements
²⁸⁶ carried out before and after irradiation.

²⁸⁷ Building on the understanding of the behaviour of the diamond, two applications
²⁸⁸ were developed. The fourth chapter describes the Diamond Beam Monitor, a detec-
²⁸⁹ tor that makes use of the diamond's charge measurement capabilities and its high
²⁹⁰ radiation hardness. This detector has been installed in one of the largest particle
²⁹¹ physics experiments in the world and is currently taking data. Here, its development
²⁹² process is presented: the quality control procedures during assembly and installation,
²⁹³ its performance in the test environment and some recent experimental data.

²⁹⁴ The final and most important chapter describes the real-time application for par-
²⁹⁵ ticle identification. Here the shape of the electrical signal of the diamond sensor is
²⁹⁶ used to discriminate different types of radiation in real time and dead time free. The
²⁹⁷ chapter includes the description of the device's logic and algorithms, lab test results
²⁹⁸ and the application in neutron monitoring.

²⁹⁹ 1.1 Fundamental research

³⁰⁰ This section gives a short overview of the institutes and collaborations carrying out
³⁰¹ fundamental physics research. The facilities were used for the research carried out in
³⁰² this thesis.

³⁰³ The aim of fundamental (even pure or basic) research is to improve the scientific
³⁰⁴ theories and verify them to improve our understanding of the universe. It does not
³⁰⁵ in itself focus on applying this research by developing products and is not meant to
³⁰⁶ create a direct return on investment. Instead, it expands the overall knowledge of the
³⁰⁷ human kind - by making the results freely available to the general public.

³⁰⁸ Particle physics research peers into the smallest constituents of the universe, dis-
³⁰⁹ secting the atoms into quarks and electrons, catching cosmic rays and figuring out
³¹⁰ what dark matter is made up of. Particle physicists want to explain the phenomena
³¹¹ surrounding us by studying the fundamental particles and the mechanisms governing
³¹² their interactions. By understanding this, we would be able to answer difficult ques-
³¹³ tions; How did the universe begin? What is the invisible force (dark matter, dark
³¹⁴ energy) pushing the galaxies apart from each other? Where does mass come from?
³¹⁵ Why is there almost no antimatter in the universe? In this effort, scientists have
³¹⁶ formed several theories. One of them, the Standard Model of particles, is currently
³¹⁷ the best theory to describe the visible universe.

³¹⁸ **The Standard Model** (SM) is a physics theory developed in the 1970's [37]. It
³¹⁹ was designed to explain the current experimental results. As such, it was also able to
³²⁰ predict new discoveries and was a driving force for the scientists to invest time and
³²¹ money in developing new experiments. To date, it is by far the most established and
³²² verified physics theory. It explains how the basic building blocks of matter – *fermions*
³²³ – interact with each other via mediators of interactions called *bosons*. There are two
³²⁴ main families of fermions - *quarks* and *leptons*, as shown in diagram 1.1. Each group
³²⁵ consists of six members divided into three *generations*, the first being the lightest and
³²⁶ most stable and the last the heaviest – unstable. The nature around us is made up
³²⁷ of the stable particles – those from the second or third generations can only be found
³²⁸ in cosmic rays or produced artificially using particle accelerators.

³²⁹ Quarks have a spin of 1/2 and a charge of either +2/3 (up, charm, top) or -1/3
³³⁰ (down, strange, bottom) while the leptons have a spin of 1/2 and a charge of either 1
³³¹ (electron, muon, tau) or 0 (electron neutrino, muon neutrino, tau neutrino). Leptons
³³² only exist individually – they do not cluster. Quarks, however, immediately form a
³³³ cluster of either two (unstable), three (more stable) or five (unstable). Two up and
³³⁴ one down quark make up a proton whereas two down and one up quark make up a
³³⁵ neutron.

³³⁶ In addition to fermions, each particle has its corresponding antiparticle – a particle
³³⁷ with the same mass but the opposite charge. If an antiparticle hits a particle, they
³³⁸ annihilate each other, producing energy in form of photons.

³³⁹ Bosons are the carriers of force, mediating weak (W^+ , W^- and Z bosons), strong

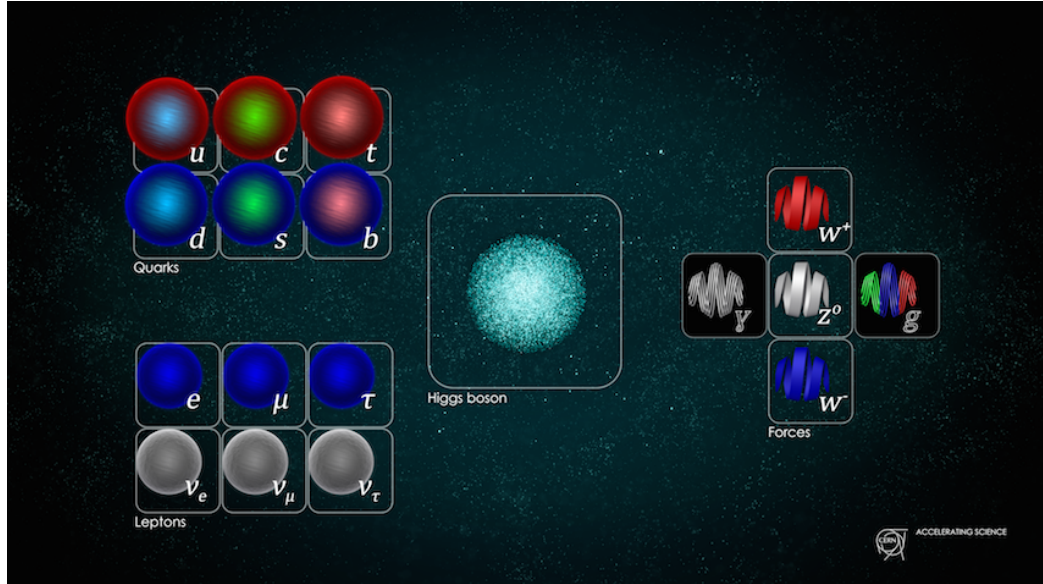


Figure 1.1: Standard model [22]

(gluons) and electromagnetic (photons) interactions. The weak interaction is responsible for the radioactive decay of subatomic particles, thus playing an essential role in nuclear fission – a process taking place in the stars. The electromagnetic interaction works at a macroscopic level – it allows particles to interact via electric and magnetic fields. The strong interaction is effective at distances of a femtometer and it governs how quarks interact and bind with each other. An additional boson is the Higgs boson and was discovered at CERN in 2012 [6]. It is a representation of the Higgs mechanism, which gives rise to the mass (or lack thereof) of all the particles in the Standard Model.

1.1.1 CERN

CERN (European Centre for Nuclear Research) [6] is a nuclear research institute housing the largest particle physics laboratory in the world. It straddles the Swiss-French border just outside Geneva. It was established in 1954 to bring the war-torn Europe together by means of fundamental scientific research. Today, it has 22 member state countries and several observer states. More than 10000 scientists, engineers, technicians, students and others from all around the globe work at CERN on many projects in research fields ranging from particle to nuclear physics. The scope is to probe the fundamental structure of the universe and to understand the mechanisms governing it. Therefore CERN's main function is to provide the infrastructure for high-energy physics experiments. These are carried out using large machines called particle accelerators. These instruments boost beams of particles to high energies before making them collide with each other or with stationary targets. The resulting collisions are recorded by particle detectors and later analysed by physicists. To carry out research on the smallest constituents of matter, their dynamics and struc-

1.1. FUNDAMENTAL RESEARCH

ture, very high energies are needed. This is why the most powerful accelerators are used for fundamental research. The largest accelerators at CERN are the Proton Synchrotron [], the Super Proton Synchrotron [36] and the Large Hadron Collider [].

1.1.2 Particle accelerators

A particle accelerator is a machine that accelerates beams of charged particles like protons, electrons, ions etc. It generates electric fields that add kinetic energy to the particles, speeding them up. It then uses magnets to retain them within a defined trajectory and inside the evacuated beam pipe. The trajectory can be either linear (linear accelerators) or circular (circular or cyclic accelerators). The advantage of the latter ones is that they can accelerate particles many times while keeping them in orbit.

Particle accelerators are used in numerous fields ranging from fundamental and material research, cancer treatment to industrial applications, such as biomedicine and material processing. There are several types of accelerators existing: electrostatic accelerators, linear accelerators (LINACs), cyclotrons, synrocyclotrons, synchrotrons, synchrotron radiation sources and fixed-field alternating gradient accelerators (FFAGs).

The Large Hadron Collider (LHC, figure 1.2) at CERN is the largest particle collider in the world. It is a 27 km long circular machine set up in a tunnel deep under the surface (ranging from 50 to 175 m). It accelerates two proton beams to the energy of 6.5 TeV per beam before it makes them to collide with each other at four different points around its circumference. The LHC was build between 1998 and 2008 and was first successfully started in 2010 and operated stably until 2013 when it underwent a two years long upgrade. They restarted its operation at the beginning of 2015. The hair-thin particle beams travel inside two evacuated pipes with a \sim 5 cm radius. Coils made up of a superconductive material are wound up around the pipes in special patterns. When they are cooled down to -271 °C using liquid helium, they become superconductive - the resistivity of the material drops significantly, minimising the heat dissipation despite high electric currents. These produce strong magnetic fields which bend the particles and keep them in a circular trajectory. The particles are accelerated when traversing the radiofrequency (RF) cavities with the RF frequency of 400 MHz. This oscillating frequency creates buckets – compartments for bunches of highly energetic particles – which are 2.5 ns long. Only one out of ten buckets is being filled, so the bunches are spaced at 25 ns. This defines the machine's clock as well as the maximum rate of collisions - the bunches travelling in the opposite direction will cross at the intersections up to 40 million times per second. Currently around 20 collisions occur during every bunch crossing, making the maximum collision rate of 10^9 per second. The number of collisions will further increase in the next years, when they will increase the number of particles in every bunch and decrease the transverse spread of the bunches – squeeze them, therefore increase their density and the collision probability.

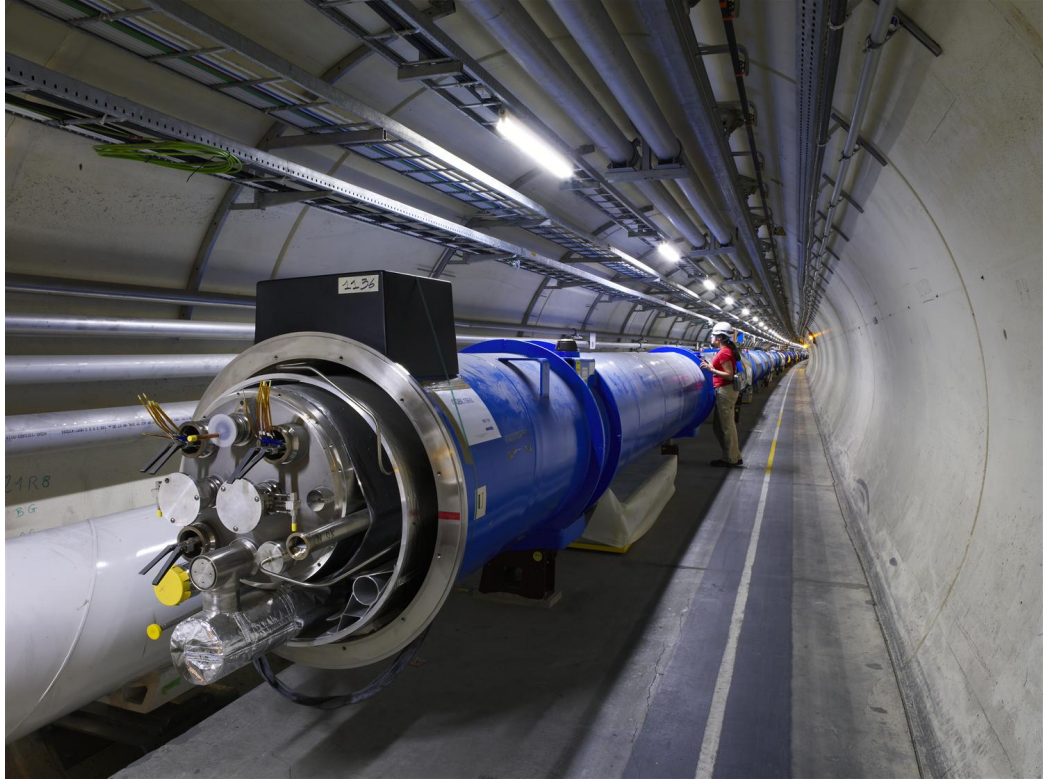


Figure 1.2: The Large Hadron Collider [20]

405 1.1.3 The ATLAS experiment

406 ATLAS (short for A Toroidal Lhc ApparatuS, figure 1.3) [] is a particle physics
407 experiment at CERN. Its purpose is to verify current theories and search for new
408 discoveries by observing and analysing high energy proton-proton collisions produced
409 by the LHC. It is the biggest experiment at CERN by dimensions (45 m in length and
410 26 m in height) and the number of people involved (more than 3000 physicists and
411 engineers). The ATLAS detector consists of many detectors, each designed to measure
412 a specific property of the particles and photons produced during the collision. The
413 closest to the collision point is the Inner Detector (ID), which consists of several layers
414 of highly spatially segmented semiconductor sensors. These can record the path of the
415 individual particles and photons. In addition, a strong magnetic field of 2 T curves the
416 paths of the charged particles, which in turn allows the ID to identify an individual
417 particle's charge and momentum. The next two parts are the electromagnetic and tile
418 calorimeter. These detectors weigh a few thousand tonnes and measure the energy of
419 the particles that are stopping in the bulk. The only particles that make it through
420 the calorimeters are muons. These are detected by the Muon Spectrometer, a set of
421 large plates placed all around the inner layers. Last is the superconductive magnet,
422 which provides the magnetic field through the whole of ATLAS except the ID, which
423 already has its own magnets. To sum up, the Inner Detector measures the charge and
424 momenta of the particles and photons, the calorimeters measure their energies, the

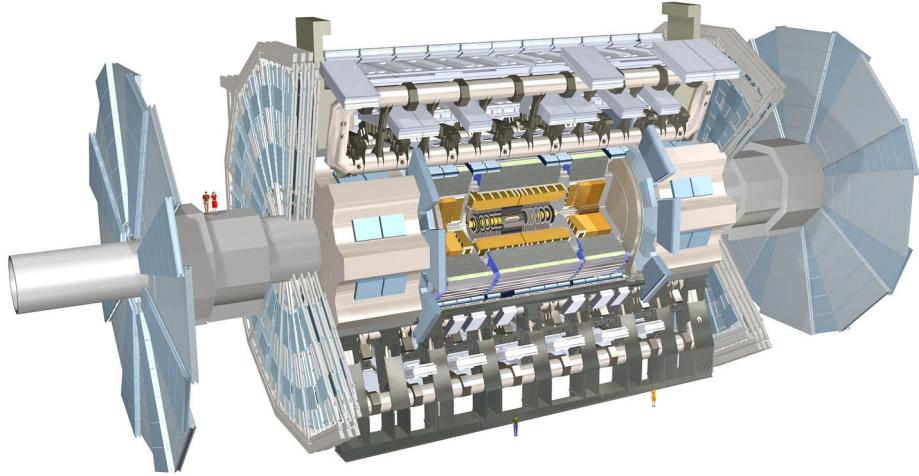


Figure 1.3: The ATLAS Experiment [38]

425 Muon Spectrometer measures muons and the magnets provide magnetic fields, which
426 curve the trajectories of the charged particles, facilitating the charge and momentum
427 measurements.

428 A complex Trigger and Data Acquisition system (TDAQ) is in place to distribute
429 the clock signal, configure the detectors, trigger them and handle the output data.
430 They are then stored at the CERN computer centre and distributed across the globe
431 by means of the GRID – a cloud-like distributed data system.

432 The ATLAS detector has been designed to measure every collision taking place in
433 its core. With 25 ns between collisions, this makes up 40 million collisions per second.
434 In reality, the maximum achievable rate is about 300 kHz. The recorded collision
435 is called an event. Every event holds information from all the detector channels
436 within ATLAS. With $\sim 10^6$ channels, an event size is approximately 10 MB. At the
437 maximum achievable rate this means a data rate of up to 3 TB/s. Unfortunately
438 no supercomputer existing today is capable of reading in and saving such a huge
439 amount of data. This is where the trigger logic comes into play. It is programmed to
440 decide in the order of tens of nanoseconds after an event whether this is a potentially
441 interesting event or not. If so, it triggers the readout of the whole detector. This way,
442 the recorded event rate is reduced from 300 kHz to ~ 500 Hz, which is already within
443 the limits of the computing centre's capabilities.

444 1.1.4 Atominsttitut, Vienna

445 Atominsttitut (ATI) [2], an institute for atomic and subatomic physics, was estab-
446 lished in 1958 in Vienna as an inter-university institute. It currently houses around

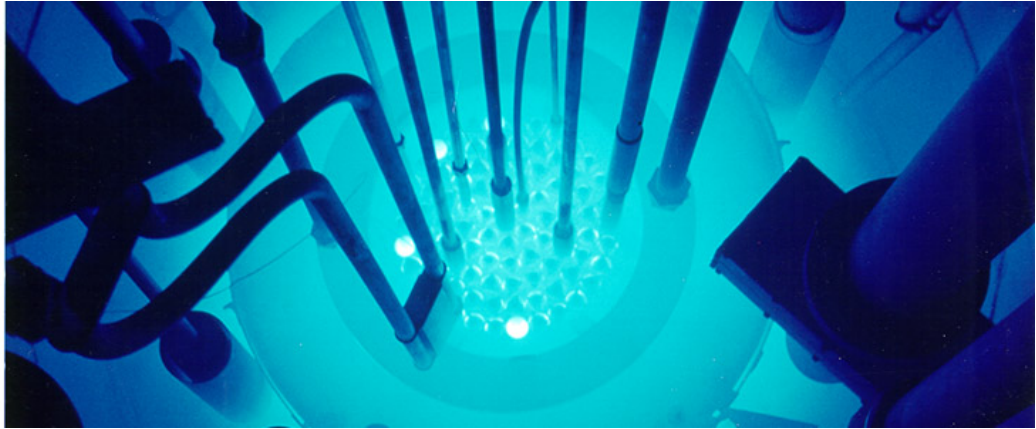


Figure 1.4: The TRIGA MARK II neutron reactor [15]

⁴⁴⁷ 200 people involved in a broad range of research fields: quantum, particle, neutron,
⁴⁴⁸ nuclear, radiation and reactor physics, quantum optics etc. Its central facility is a
⁴⁴⁹ TRIGA MARK II neutron reactor (described in detail below).

⁴⁵⁰ As of 2002 the ATI is part of the University of Technology in Vienna.

⁴⁵¹ **TRIGA MARK II neutron reactor** [12] is a reactor of a swimming-pool type
⁴⁵² used for training, research and isotope production. It is one of 40 such reactors
⁴⁵³ worldwide, produced by an californian company General Atomic in the early 60's. It
⁴⁵⁴ is capable of continuous operation at a maximum output power of 250 kW. The reactor
⁴⁵⁵ core consists of 3 kg of 20 % enriched uranium (^{235}U). The fuel moderator rods are
⁴⁵⁶ mostly made up of zirconium with low percentage of hydrogen and uranium. Both the
⁴⁵⁷ core and the rods are immersed in a pool of water as shown in figure 1.4 for the purpose
⁴⁵⁸ of cooling and radiation protection. The surrounding concrete walls are 2 m wide
⁴⁵⁹ with an added graphite layer for improved shielding. Four main experimental beam
⁴⁶⁰ holes are placed radially through the walls. All exits are heavily shielded to prevent
⁴⁶¹ radiation damage to people, but still leaving enough space to set up experiments.
⁴⁶² Apart from the beam holes, there are several other exits and components, e.g. a
⁴⁶³ thermal column for generation of thermal (low energetic) neutrons.

⁴⁶⁴ 1.1.5 n-ToF

⁴⁶⁵ n-ToF (or neutron time-of-flight) [9] is a scientific collaboration with the aim of studying
⁴⁶⁶ neutron-nucleus interactions. Over 30 institutes and universities are currently
⁴⁶⁷ active members of this collaboration, among them Atominstitut in Vienna. n-ToF
⁴⁶⁸ is also a facility at CERN where the experiments are carried out in a 200 m long
⁴⁶⁹ experimental area. The knowledge stemming from the experimental results can then
⁴⁷⁰ be applied in various fields ranging from nuclear technology and cancer therapy to
⁴⁷¹ astrophysics.

⁴⁷² A pulsed beam of highly energetic protons (20 GeV/c) is produced by the Proton
⁴⁷³ Synchrotron (PS) and aimed at a fixed lead spallation target. Each proton hitting

1.2. PARTICLE DETECTORS

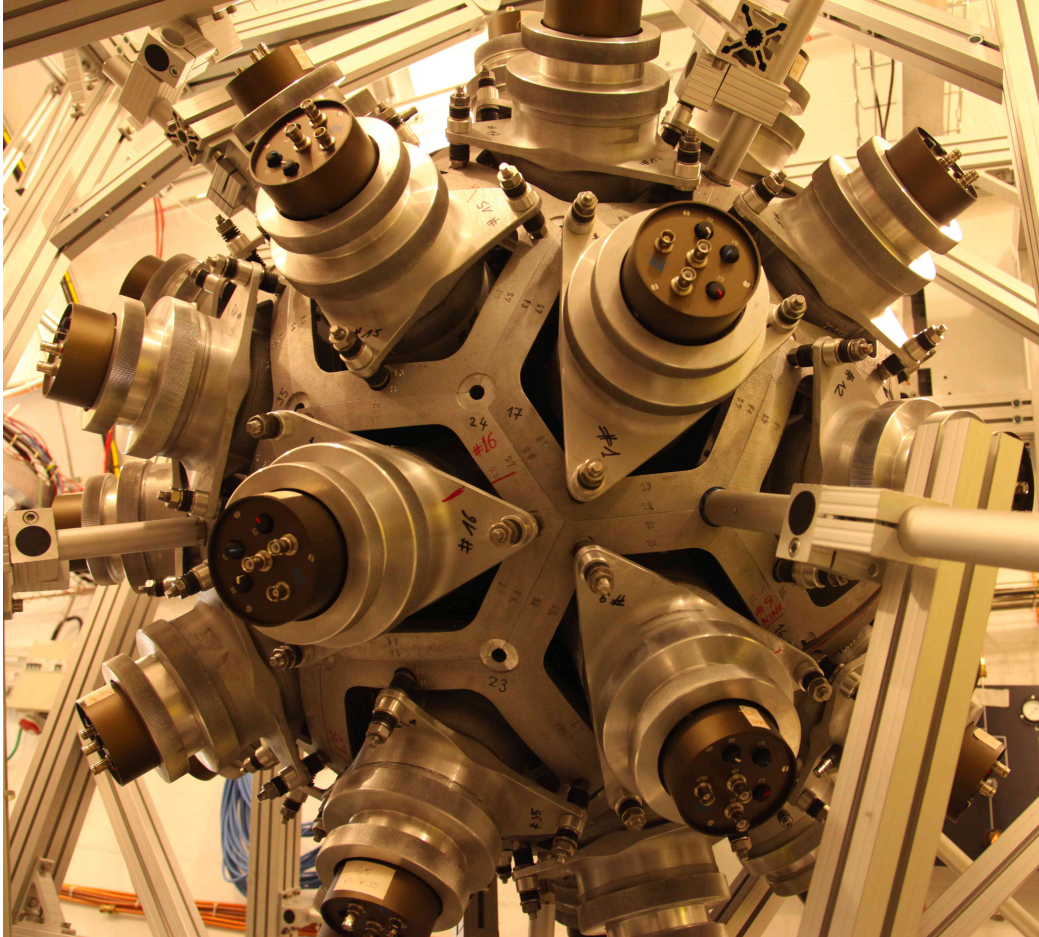


Figure 1.5: The calorimeter in the n-ToF area [19]

474 the target produces around 300 neutrons of various energies. Initially highly energetic
475 neutrons are slowed down by the target and by a slab of water placed behind it. This
476 broadens their energy spectrum, which then ranges from meV (thermal neutrons) to
477 GeV (fast neutrons). The neutrons are then collimated and sent through a 185 m
478 long evacuated pipe to the experimental area, where they are made to collide with
479 another target or a sample. The radiation resulting from the collisions is detected by
480 a set of dedicated detectors around the interaction point (seen in figure 1.5). Having
481 different energies, neutrons travel with different speeds, highly energetic ones reaching
482 the target faster than those with low energies. Analysis of the collisions with a precise
483 timing allows us to determine the interaction probability with sample material as a
484 function of incident neutron energy.

485 1.2 Particle detectors

486 Particle detectors, or radiation detectors, have first come into use at the end of the
487 19th century. At that time Wilhelm Röntgen used a photographic plate onto which

he shone X-rays. Soon after, in 1912, Victor F. Hess discovered cosmic rays during a balloon flight. This paved the way for development of particle detectors. A cloud chamber was designed – a chamber filled with a supersaturated vapour of water or alcohol. If a highly energetic particle traversed the chamber, the mixture ionised, creating condensation nuclei. These traces were visible and were photographed. All the subsequent particle detectors relied on the same principle of interaction between the particles – ionisation. The bubble chamber invented in 1952 used a superheated transparent liquid – a liquid heated just below its boiling point. A particle ionised the liquid, forming microscopic bubbles along its trajectory. Then followed the spark chamber and the wire chamber where the particle ionised the gas, causing a spark between two parallel plates at a high potential difference. These are nowadays used in museums as showcases. Next were ionisation chambers, which measured the induced current of the free ionised charges moving in an externally applied electric field. Finally in the 1960s, semiconductor detectors were introduced. Their principle of operation is similar to that of an ionisation chamber, with the difference that a semiconductive material is used as an ionisation medium instead of gas. Every technology has its advantages and disadvantages. Nowadays an ensemble of several types of detectors is used as a single detector system. There are many considerations that need to be taken into account when designing such a system: detector geometry, segmentation, event rate, efficiency, readout, support structures, cabling, cooling, cost etc.

On large, particle detectors can be divided in two groups: tracking detectors and calorimeters. The former are designed to measure trajectories (momentum) of particles and photons with a minimal impact on their flight path or energy. They must be built with a high spatial resolution and lightweight. Typically they are semiconductor detectors. The calorimeters, on the other hand, measure the energy of the particles/photons by stopping them. This means they need to be heavy and dense. A typical physics experiment nowadays would consist of a tracking detector enclosed by a calorimeter. This way both the momentum and energy are derived, measuring energy, charge and trajectory of every particle/photon.

1.2.1 Semiconductor detectors

Semiconductor particle detectors are devices that use a semiconductor for detecting radiation. They work on the principle of an ionisation chamber. An incident particle or a photon ionises the atoms in the crystal lattice. The freed charges start drifting in an externally applied electric field, inducing current on the electrodes. The charges are freed if the deposited energy is higher than the energy band gap. There are many semiconductor materials currently existing, each with a different band gap. Germanium (Ge), for instance, has a band gap of 0.67 eV, which means that most of the electrons at the room temperature will already be in an excited state. Diamond's 5.5 eV band gap, on the other hand, is too high for the visible light to excite the electrons. Silicon with an energy gap of 1.12 eV has been the material of choice for the

1.2. PARTICLE DETECTORS

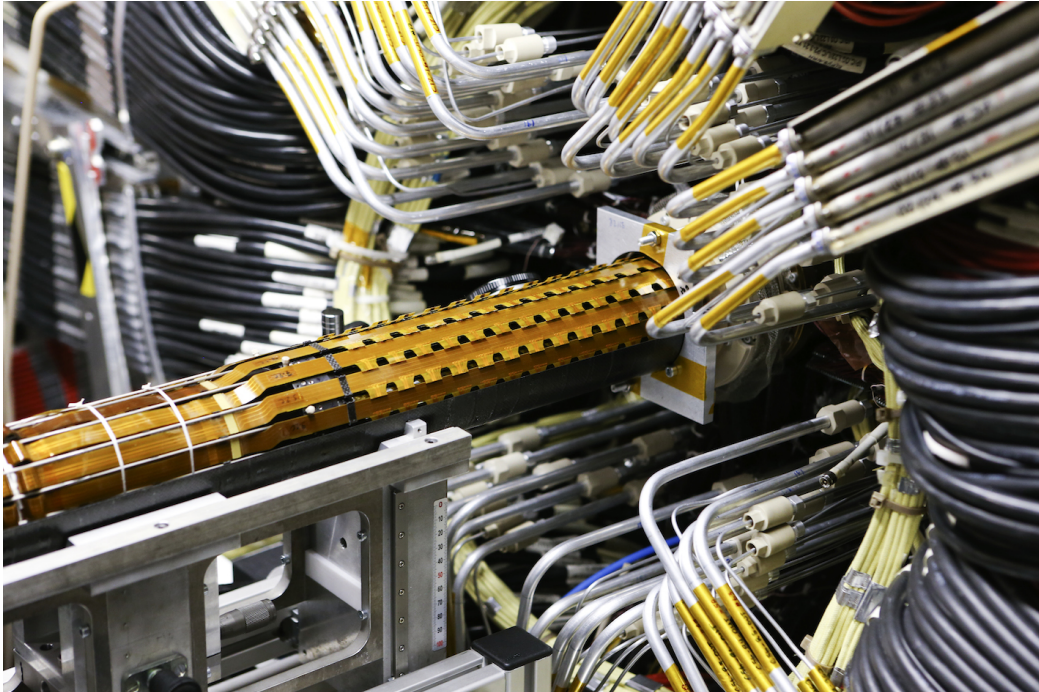


Figure 1.6: The Insertable B-Layer – a silicon particle tracker installed in the ATLAS experiment in 2014 [34]

529 majority of semiconductor applications, including radiation detectors. Semiconductor
530 detectors are most widely used for tracking applications, like the Insertable B-Layer
531 (see figure 1.6) [39], which was installed in ATLAS Experiment in 2014. They can
532 be produced into light and thin sensors, they have a fast signal response, they are
533 highly efficient and highly resistant to radiation damage. They also allow for a fine
534 spatial segmentation to increase the tracking resolution. Semiconductor sensors come
535 in several configurations. The simplest type is a pad – a single plate measuring
536 25 mm^2 . Pads are used for particle counting and radiation monitoring. Next is a
537 strip detector, a more finely segmented detector made out of long parallel sensing
538 areas or strips. Each strip has its own signal line for readout. Usually the strip
539 detectors are used in pairs – one detector is placed on top of the other at a 90° angle
540 to increase spatial resolution in both axes. The third and the most finely segmented
541 is a pixel detector, consisting of a 2D array of independent sensing areas. In tracking
542 applications, pixel detectors are used where the detection resolution is the highest.
543 Due to their high production cost and a high number of signal channels, they can
544 only cover limited areas. Strip detectors are cheaper to produce and can be used to
545 cover larger areas in several consecutive layers.

546 1.2.2 Diamond sensors

547 Diamond has been known for over two millennia, valued for its mechanical properties
548 and its appearance. When we learnt how to synthesise it, diamond found its way to

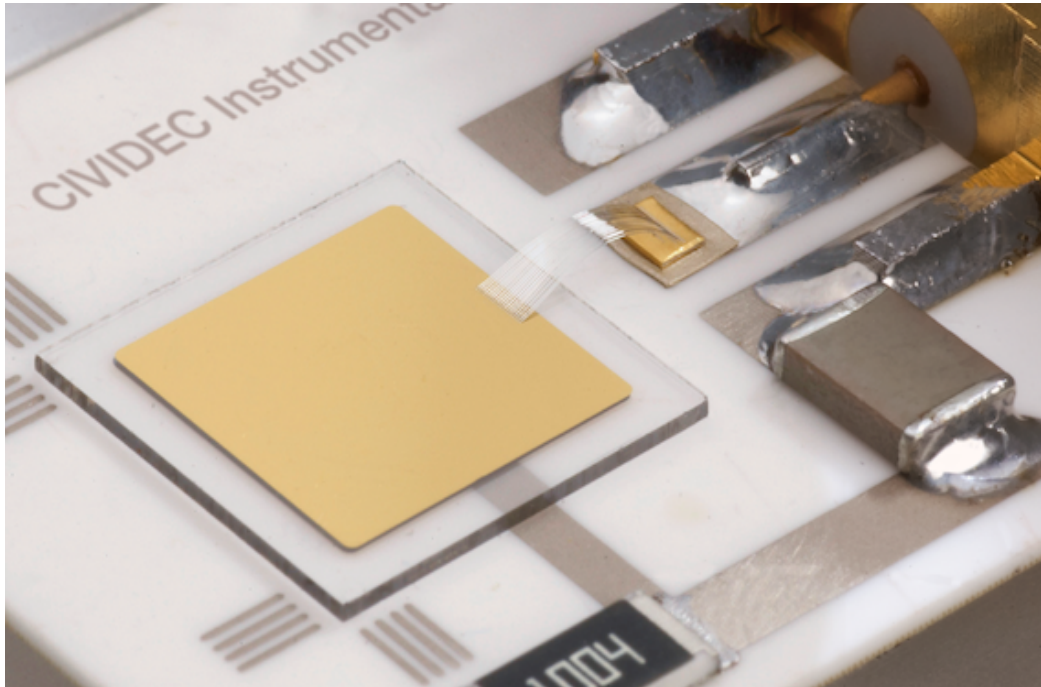


Figure 1.7: A pCVD diamond pad detector [23]

549 a broad range of industries which exploited its optical and electrical properties. The
550 discovery of the Chemical Vapour Deposition (described below) as a new synthesis
551 process gave rise to a range of new applications. From being used on machines
552 for drilling tunnels it found its way to electronics, high-power switching devices,
553 electrochemical systems, radiation sensors, quantum computing etc. Recently it was
554 found that it also exhibit superconductivity. This thesis focuses on the use of diamond
555 for radiation detection. Compared to a natural diamond, a detector-grade CVD
556 diamond has almost no impurities (foreign atoms like nitrogen or boron). The carbon
557 lattice is very uniform, which improves its electrical properties. It is an almost perfect
558 insulator, but behaves as a semiconductor under certain conditions. Compared to
559 silicon, the most widely used semiconductor material for radiation detection, it has
560 many advantages, which are described in detail in chapter ???. Figure 1.7 shows a
561 diamond pad detector produced by CIVIDEC Instrumentation GmbH.

562 **Chemical vapour deposition** (CVD) [] is a process where a material is deposited
563 from a gas onto a substrate, involving chemical reactions. It is often carried out un-
564 der high pressure and high temperatures. It takes place in enclosed chambers called
565 furnaces with careful regulation of the temperature, pressure and gas mixture. Syn-
566 thetic diamond is grown at 700–900 °C with a mixture of hydrogen and methane
567 gas. At this temperature the molecules dissociate into carbon and hydrogen atoms.
568 The carbon atoms are the building blocks and are deposited on the surface of the
569 substrate. However, they would rather form graphitic bonds as they are more stable
570 than diamond bonds. Nevertheless, with high pressure, high temperature and with
571 added abrasive atomic hydrogen, the graphitic double bonds are broken up and con-

1.2. PARTICLE DETECTORS

572 vertyed into diamond bonds. The speed of the growth can be anywhere between 0.1
573 and 10 micron per hour. The detector grade samples are grown at a rate of the order
574 of 1 micron per hour. They can grow up to several millimetres in thickness. Their
575 width, however, depends entirely on the substrate used. Diamond can be deposited
576 on various materials: diamond, silicon, tungsten, quartz glass etc. The substrate
577 material must be able to withstand the high temperatures during the CVD process.
578 The diamond substrate does not need any surface pre-treatment. Carbon atoms form
579 bonds with atoms in the existing crystal structure. This is the homoepitaxial growth
580 where the newly deposited atoms retain the orientation of the structure in the sub-
581 strate. Other non-diamond substrates, however, need to be pre-treated, usually by
582 being polished using diamond powder. Some powder particles remain on the surface,
583 acting as seeds for the growth of small crystals or grains. These grains grow and
584 at some point merge with the adjacent ones, making up a compact material. The
585 lower side is later polished away. These diamonds are called *polycrystalline* (pCVD)
586 whereas those grown on a diamond substrate are *single crystal* (sCVD) diamonds.
587 The area of the former can be large - up to 0.5 m^2 or more compact 15 cm^2 in the case
588 of detector grade diamonds. The sCVD diamonds, on the other hand, can currently
589 only measure up to 1.5 cm^2 .

590

Chapter 2

591

Signal formation in diamond

592 This chapter describes the fundamentals of signal formation in a diamond sensor, as
593 well as its use as a particle detector. This is described in section 2.1 where energy
594 deposition and signal formation mechanism are explained. Then some examples of
595 ionisation are shown. Later, some of the internal lattice defects that effect the signal
596 are described. The final section contains the description of the remaining part of the
597 signal chain – signal amplifiers, digitisers and devices for signal processing. Noise
598 contributions are discussed at every stage of the signal chain.

599 There are many types of radiation sensors existing, but in this chapter we will
600 focus on semiconductors, in particular on diamond sensors. Diamond is a good insu-
601 lator, but behaves as a semiconductor in certain cases. In fact, the main principle of
602 operation is the same for diamond, silicon and other semiconducting materials – ion-
603 isation. An incident highly energetic charged particle ionises the atoms in the lattice,
604 freeing electrons and holes, which then drift towards positively and negatively charged
605 electrodes, inducing an electrical signal. A sensor converts the energy deposited by a
606 particle or a photon to an electrical signal.

607 Silicon is currently considered as the industry standard for particle detection.
608 However, there are some disadvantages of using silicon instead of diamond, due to
609 significant differences in the material properties. In particular, the properties of silicon
610 change significantly with radiation. For instance, the leakage current increases, which
611 in turn increases shot noise and can lead to a thermal runaway. In addition, due to
612 induced lattice defects, which act as charge traps, its charge collection efficiency starts
613 dropping quickly. Both are true for diamond as well, but on a much smaller scale.

614 Table 5.2 compares the properties of diamond and silicon. Some of these values
615 will be revisited and used in the course of this thesis.

Property	Diamond	Silicon
Band gap energy E_g (eV)	5.5	1.12
Electron mobility μ_e ($\text{cm}^2 \text{ V}^{-1} \text{ s}^{-1}$)	1800	1350
Hole mobility μ_h ($\text{cm}^2 \text{ V}^{-1} \text{ s}^{-1}$)	1200	450
Breakdown field (V cm^{-1})	10^7	3×10^5
Resistivity ($\Omega \text{ cm}$)	$> 10^{11}$	2.3×10^5
Intrinsic carrier density (cm^{-3})	$< 10^3$	1.5×10^{10}
Mass density (g cm^{-3})	3.52	2.33
Atomic charge	6	14
Dielectric constant ϵ	5.7	11.9
Displacement energy (eV/atom)	43	13 – 20
Energy to create an e-h pair (eV)	13	3.6
Radiation length (cm)	12.2	9.6
Avg. signal created/ μm (e)	36	89

617 Table 2.1: Comparison diamond – silicon []

 618

2.1 Principles of signal formation in semiconduc- 619 tors

 620 There are several ways the particles can interact with the sensor: via bremsstrahlung [],
 621 elastic or inelastic scattering (e-h pair production). Bremsstrahlung is radiation cre-
 622 ated when a particle is deflected from its original path due to attraction of the core of
 623 an atom. This is in principle an unwanted effect in semiconductors as it decreases the
 624 spatial resolution of the sensor. Elastic scattering is deflection of the particle's tra-
 625 jectory without energy loss. Inelastic scattering is the interaction through which the
 626 atom is ionised and an electron-hole pair is created. All these effects are competing
 627 and are dependent on the particle's mass, momentum etc.

 628 Semiconductors are materials that are conductive only under specific
 629 conditions. They can be made up of atoms with four electrons in their valence band
 630 (e.g. silicon–Si, carbon–C or germanium–Ge) or as combinations of two or more
 631 different materials (e.g. gallium arsenide–GaAs). The atoms in the lattice form
 632 valence bonds with adjacent atoms, making solid crystal structures. These bonds
 633 can break up if sufficient external energy is applied. The electron that was forming
 634 the bond is kicked out, leaving behind a positively charged ion with a vacancy in its
 635 valence band (see figure 2.1a). A free electron-hole pair is thus created. The free
 636 electron travels through the crystal until it is caught by another hole. Similarly, the
 637 hole also “travels” through the material. Its positive charge attracts a bound electron
 638 in the vicinity, which breaks from the current bond and moves to the vacancy, leaving
 639 a new hole behind. The process continues, making it look like the vacancy – the hole
 640 – is traveling through the material.

 641 The electrons need to absorb a certain energy to get kicked out of the atomic
 642 bond – to get ionised. The minimal energy required to excite (ionise) an electron in
 643 a semiconductor is equal to the energy gap E_g . Typical widths of the forbidden gap
 644 are 0.7 eV in Ge, 1.12 eV in Si, 1.4 eV in GaAs and 5.5 eV in Di. Due to the small

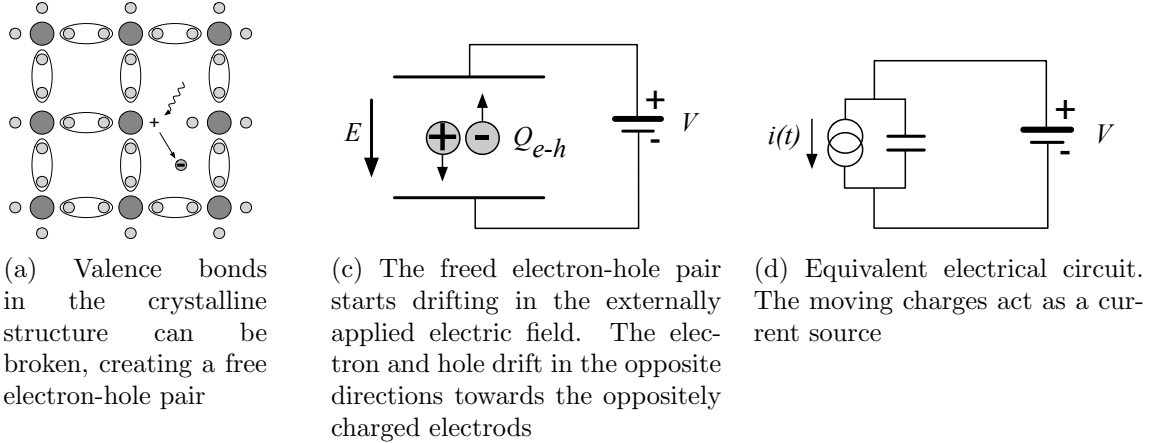


Figure 2.1: In the equivalent electrical circuit diagram, electron-hole creation and drift can be modelled as a current source with a capacitor in parallel

band gap in semiconductors some electrons already occupy the conduction band at room temperature (RT). The intrinsic carrier concentration n_i in semiconductors is given as

$$n_i = T^{3/2} \cdot \exp\left(-\frac{E_g}{2kT}\right) \quad (2.1)$$

wherein $k = 1.381 \times 10^{-23} \text{ m}^2 \text{ kg s}^{-2} \text{ K}^{-1}$ is the Boltzmann constant and T is the temperature.

If an external electric field is applied to the crystalline structure, the free electrons and holes drift toward the positive and negative potential, respectively (see figure 2.1c). While drifting, the charges couple with the electrodes, inducing current in the circuit, which is explained by the Shockley–Ramo theorem (see subsection below). The charges recombine upon reaching the electrodes.

Energy deposition of α radiation and heavy ions

Energy deposition of β and γ radiation The mean energy loss of a particle traversing the detector with respect to its momentum is given with the the Bethe-Bloch equation []:

$$-\left\langle \frac{dE}{dx} \right\rangle = \frac{4\pi}{m_e c^2} \cdot \frac{n z^2}{\beta^2} \cdot \left(\frac{e^2}{4\pi\epsilon_0} \right)^2 \cdot \left[\ln \left(\frac{2m_e c^2 \beta^2}{I \cdot (1 - \beta^2)} \right) - \beta^2 \right] \quad (2.2)$$

The resulting function for a muon (a heavy electron) is shown in figure 2.2. At the momentum of around 300 MeV/c the particle deposits the lowest amount of energy. That is called a minimum ionising particle or a MIP.

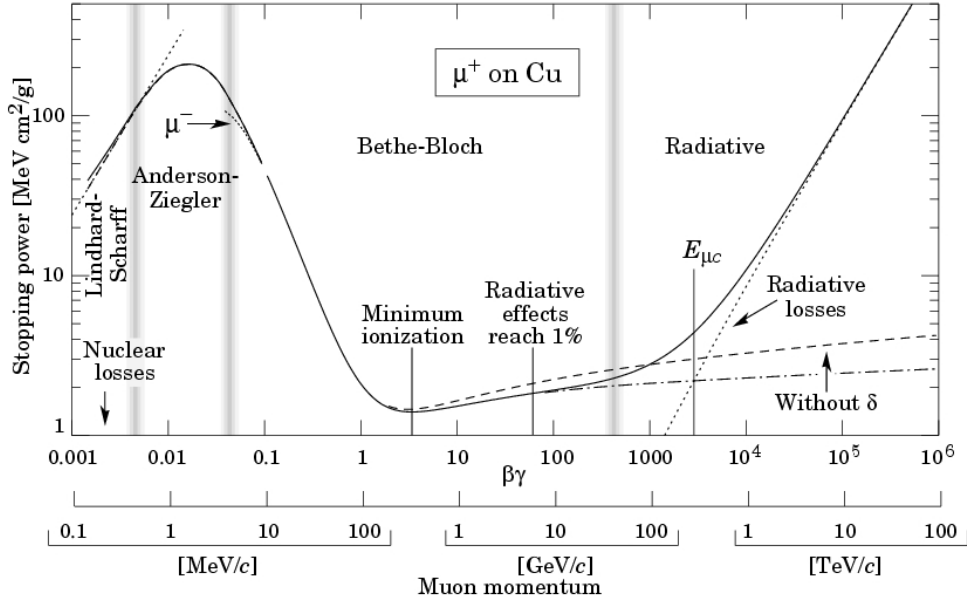


Figure 2.2: Stopping power for muons according to the Bethe-Bloch formula []

662 2.1.1 Signal induction by moving charges

663 The book [17] gives a simple introduction to understanding signal induction in a
 664 conducting plane by a point-like charge. The idea behind it lies in the coupling of
 665 the charge with the electrode. The electrode can be in this case modelled as an
 666 infinite conducting plane. When the point charge q is created (e.g. an electron-hole
 667 pair created via ionisation), its electrostatic field lines immediately couple with the
 668 electrode, as seen in figure 2.3a. The electric field on the metal surface due to a
 669 point-like charge q at the distance z_0 equals

$$E_z(x, y) = \frac{q z_0}{2\pi\epsilon_0(x^2 + y^2 + z_0^2)^{\frac{3}{2}}} \quad E_y = E_z = 0. \quad (2.3)$$

670 A mirror charge appears on the conducting plane, with a charge density distribution

$$\sigma(x, y) = \epsilon_0 E_z(x, y) = \frac{q z_0}{2\pi(x^2 + y^2 + z_0^2)^{\frac{3}{2}}}. \quad (2.4)$$

671 The charge density integrated over the whole plane gives the mirror charge Q , which
 672 has the opposite value of the point charge q :

$$Q = \int_{-\infty}^{\infty} \int_{-\infty}^{\infty} \sigma(x, y) dx dy = -q. \quad (2.5)$$

673 Now we segment the plane into infinitely long strips with a width w whereby each
 674 of the strips is grounded (figure 2.3c). With the charge density distribution 2.4, the

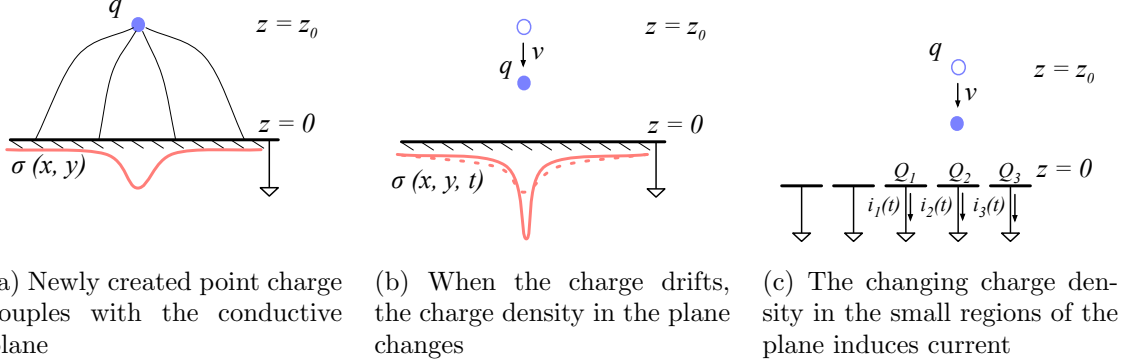


Figure 2.3: A point-like charge inducing current in a conductive plane

675 resulting mirror charge on a single strip Q_2 directly below the point charge ($x =$
 676 $0, y = 0$) will be equal to

$$Q_2(z_0) = \int_{-\infty}^{\infty} \int_{-w/2}^{w/2} \sigma(x, y) dx dy = -\frac{2q}{\pi} \arctan \left(\frac{w}{2z_0} \right) \quad (2.6)$$

677 If the charge starts moving towards the conducting plane, the mirror charge density
 678 distribution also changes (see figure 2.3b). This results in the $Q_2[z_0(t)]$ to change
 679 with time, inducing an electric current $i_n(t)$:

$$i_n(t) = -\frac{d}{dt} Q_2[z_0(t)] = -\frac{\partial Q_2[z_0(t)]}{\partial z_0} \frac{\partial z_0(t)}{\partial t} = \frac{4qw}{\pi[4z_0(t)^2 + w^2]} v. \quad (2.7)$$

680 The movement of the point-like charge therefore induces current in the conducting
 681 plane. The induced current is linearly dependent on the velocity of the point-like
 682 charge.

683 W. Shockley [42] and S. Ramo [40] independently proposed a theory which explains
 684 how a moving point charge induces current in a conductor. The Shockley-Ramo
 685 theorem can therefore be used to calculate the instantaneous electric current induced
 686 by the charge carrier or a group of charge carriers. It can be used for any number of
 687 electrodes. It states that the current $I_n^{\text{ind}}(t)$ induced on the grounded electrode n by
 688 a point charge q moving along a trajectory $\mathbf{x}(t)$ equals

$$I_n^{\text{ind}}(t) = -\frac{dQ_n(t)}{dt} = -\frac{q}{V_w} \nabla \Psi_n[\mathbf{x}(t)] v(t) = -\frac{q}{V_w} \mathbf{E}_n[\mathbf{x}(t)] v(t), \quad (2.8)$$

689 where $\mathbf{E}_n(\mathbf{x})$ is the electric field in the case where the charge q is removed, electrode n
 690 is set to voltage $V_w = 1$ and all other electrodes are grounded. $\mathbf{E}_n(\mathbf{x})$ is also called the
 691 *weighting field* of electrode n and is defined as the spatial differential of the *weighting*
 692 *potential*: $\mathbf{E}_n(\mathbf{x}) = \nabla \Psi_n(\mathbf{x})$. In the case of two parallel electrodes, the weighting field
 693 is $E_w = -\frac{d\Psi}{dx} = -1/d$, where d is the distance between the electrodes. The resulting
 694 induced current is therefore

$$i(t) = \frac{q}{d} v_{\text{drift}}(x, t), \quad (2.9)$$

2.1. PRINCIPLES OF SIGNAL FORMATION IN SEMICONDUCTORS

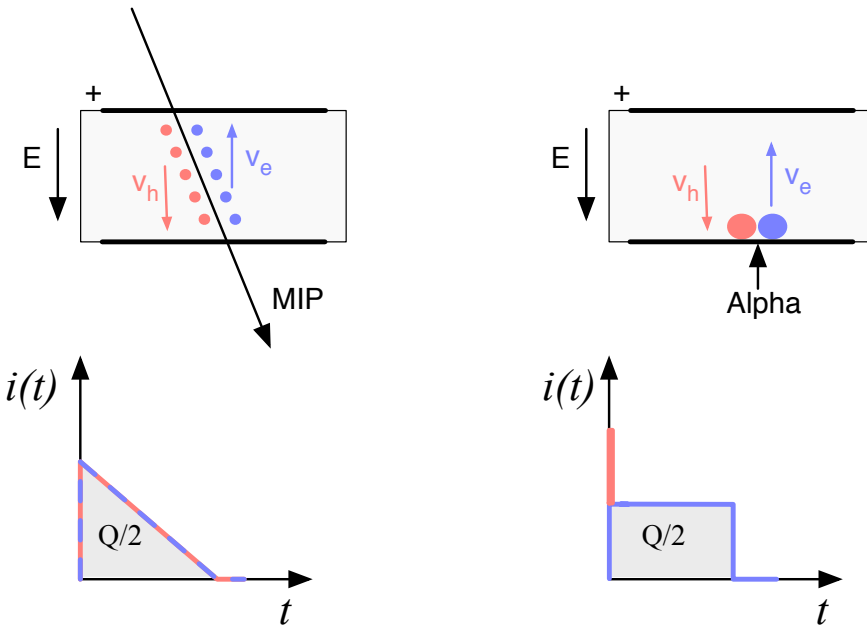


Figure 2.4: Charge carrier drift in diamond for β/γ and for α particles

695 whereby v_{drift} is the drift velocity of the point-like charge and d is the distance between
 696 the electrodes.

697 2.1.2 Radiation-induced electrical pulses

698 When a highly-energetic particle travels through the sensor, it interacts with atoms
 699 in the lattice. It ionises the valence electrons, creating electron-hole (e-h) pairs on its
 700 way. It can either deposit only a fraction of its energy and fly exit the sensor on the
 701 other side or it can get stopped in the bulk, depositing all of its energy. A special
 702 case is when it interacts with the core of the atom in the middle of the sensor via
 703 a nuclear interaction. All these various types interactions produce different amounts
 704 and different spatial distributions of e-h pairs. The induced electrical current will
 705 therefore differ for different types of interaction. Two most frequent types are shown
 706 in figure 2.4. The first diagram shows the interaction of a minimum ionising particle
 707 (an electron or a proton) or in some cases a photon, if it is energetic enough. The
 708 electrons and holes are created all along the trajectory of the particle and imme-
 709 diately start drifting towards the positive and negative electrode, respectively. At
 710 the beginning, all charges drift and contribute to the induced current. Those closest
 711 to the electrodes have a very short drift path and recombine quickly, reducing the
 712 induced current. Gradually all the charge carriers recombine. The resulting current
 713 signal is a triangular pulse with a sharp rising edge and a linear falling edge. The
 714 accumulated charge Q_s equals to the sum of the contributions of the positive and

negative charge carriers. The second type of interaction happens when the particle is stopped in the diamond close to the point of entry. Most of its energy is deposited in a small volume close to the electrode. A cloud of charge carriers is created and the charges with the shorter path to the electrode recombine almost instantly. The carriers of the opposite charge, however, start drifting through the sensor to the other electrode. In an ideal diamond sensor, their velocity is constant throughout the drift up until they recombine on the other side. The contribution of the first charge cloud is a peak with a short time. The cloud drifting through the sensor, on the other hand, induces a current signal with a flat top. The resulting signal has a shape of a rectangle, with a spike in the beginning. This spike is filtered out in a real device because it is too fast for the electronics existing currently. The accumulated charge Q_s is equal to a half of the deposited charge by the stopped particle.

The two aforementioned types of interactions have well defined signal responses. Nuclear interactions on the other hand yield various results. The resulting signal shape depends on the decay products of the interaction – they can be α , β or γ quanta, inducing a mixed shaped signal.

2.1.3 Signal charge fluctuations

Two of the important sensor characteristics are the magnitude of the signal and the fluctuations of the signal at a given absorbed energy. They determine the relative resolution $\Delta E/E$. For semiconductors the signal fluctuations are smaller than the simple statistical variance $\sigma_Q = \sqrt{N_Q}$, where N_Q is the number of released charge pairs (ratio between the total deposited energy E_0 and the average energy deposition E_i required to produce an electron-hole pair). [] shows that the variance is $\sigma_Q = \sqrt{F N_Q}$, where F is the Fano factor [] (0.08 for diamond and 0.115 for silicon []). Thus, the variance of the signal charge is smaller than expected, $\sigma_Q \approx 0.3\sqrt{N_Q}$. The resulting intrinsic resolution of semiconductor detectors is

$$\Delta E_{FWHM} = 2.35\sqrt{FEE_i} \quad (2.10)$$

wherein $E_i(Si) = 3.6$ eV and $E_i(C) = 13$ eV. E.g., for an α particle with energy $E_\alpha = 5.486$ MeV the calculated resolution in diamond is equal to $\Delta E_{FWHM} = 5.6$ keV. This defines the maximum achievable resolution for energy spectroscopy with semiconductors. Figure 2.5 shows the calculated energy resolution function for silicon and diamond.

2.2 Carrier transport in a diamond sensor

This section describes the carrier transport phenomena in diamond. This theory provides the basis for discussion about the measurements in chapter ??.

Free charge carriers in a semiconductor get thermally excited and scatter in random directions with a thermal velocity v_{th} []. Their integral movement due to thermal

2.2. CARRIER TRANSPORT IN A DIAMOND SENSOR

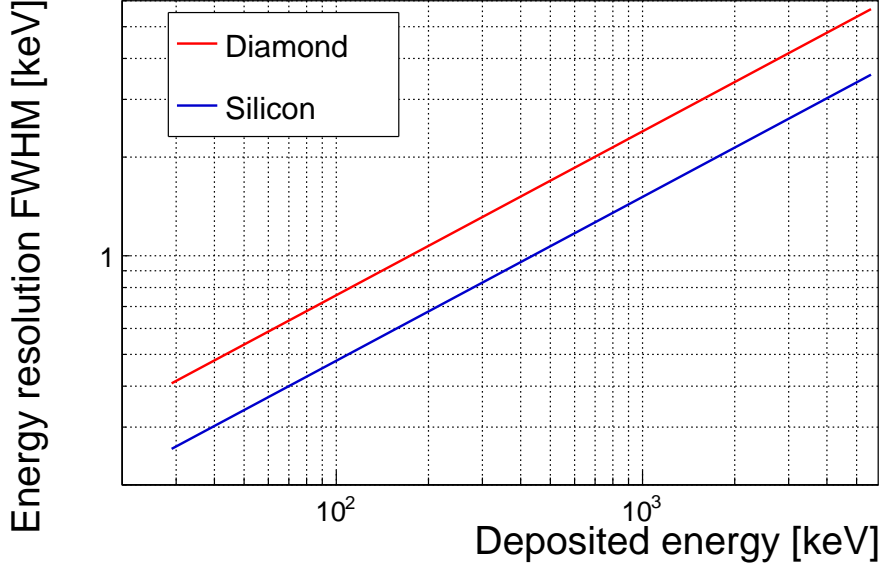


Figure 2.5: Calculated intrinsic energy resolution for silicon and diamond

excitation equals zero. Their transport is instead by means of drift and diffusion. Diffusion is caused by the concentration gradient. In its presence the carriers tend to scatter in the direction of the lower concentration. Drift on the other hand is caused by an externally applied electrical field. In that case the carriers move in parallel to the field lines. In a sensor with a high applied field the diffusion contribution is negligible.

Diffusion The concentration profile dissolves with time forming a Gaussian distribution with variance $\sigma(t) = \sqrt{Dt}$.

Drift velocity and mobility The charge carriers drift through the diamond bulk with a drift velocity $v_{\text{drift}}(E)$, which is proportional to the electric field E at low electric fields: $v_{\text{drift}} = \mu E$. The proportionality factor μ is defined as the mobility in $\text{cm}^2\text{V}^{-1}\text{s}^{-1}$. For higher fields, however, the velocity saturates. The final equation for v_{drift} is therefore

$$v_{\text{drift}}(E) = \mu(E)E = \frac{\mu_0 E}{1 + \frac{\mu_0 E}{v_{\text{sat}}}} \quad (2.11)$$

where μ_0 is the low field mobility and v_{sat} is saturation velocity. The drift velocity can be retrieved experimentally via the transit time measured with the Transient Current Technique (TCT). This technique enables the measurement of transit time t_t of the carriers through the sensor with the thickness d .

$$v_{\text{drift}}(E) = \frac{d}{t_t(E)}. \quad (2.12)$$

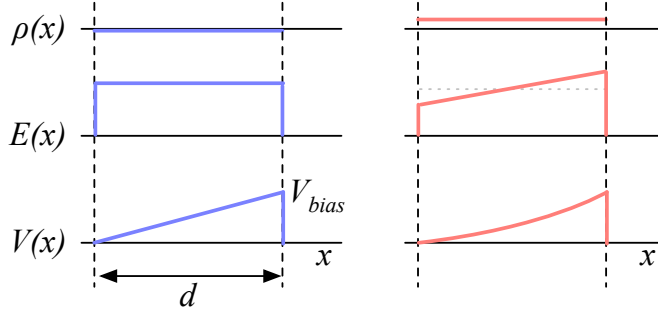


Figure 2.6: Introduction of space charge in the diamond bulk. The induced current signal is proportional to the effective electrical field. d is the thickness of the diamond sensor.

768 The velocities for holes and electrons usually differ. In diamond, the holes travel
 769 30 % faster than electrons []. The measurements in chapter ?? empirically confirm
 770 this statement.

771 **Velocity saturation** At higher drift velocities the carriers lose more energy to the
 772 lattice. They induce increasingly more lattice vibrations (phonon transport) with
 773 increased velocity. There is a velocity limit above which the carriers cannot reach –
 774 velocity saturation. Thesis [] defines this velocity to be $v_{\text{sat}}^e = v_{\text{sat}}^h = (14.23 \pm 0.12) \times$
 775 10^6 cm/s for both positive and negative charge carriers.

776 **Space charge** Poisson's equation shows that

$$\frac{d^2\Phi(x)}{dx^2} = \frac{dE(x)}{dx} = \frac{\rho(x)}{\epsilon} \quad (2.13)$$

777 where $\rho(x)$ is the space charge distribution, E is the electrical field and Φ is the voltage
 778 potential. In an ideal diamond, the externally applied high voltage potential on the
 779 two electrodes decreases linearly through the bulk. The electrical field is therefore
 780 constant throughout the sensor and the space charge distribution across it equals
 781 0. However, in some cases space charge is introduced in the bulk, uniformly or non-
 782 uniformly. It can do so by means of trapping of charge carriers in the non-uniformities
 783 in the lattice or it can already be introduced during the production of the diamond
 784 material. The space charge can be either permanent or changing – sometimes it is
 785 possible to reduce it by means of priming. All in all, it is very important to reduce
 786 it because it affects the shape of the electrical signal. Since the drift velocity of
 787 the charge carriers is proportional to the electrical field, the charges change their
 788 velocity while drifting through the space charge region. Figure 2.7 compares the
 789 voltage potential, electrical field, space charge for an ideal sensor and for that with a
 790 uniformly distributed positive space charge.

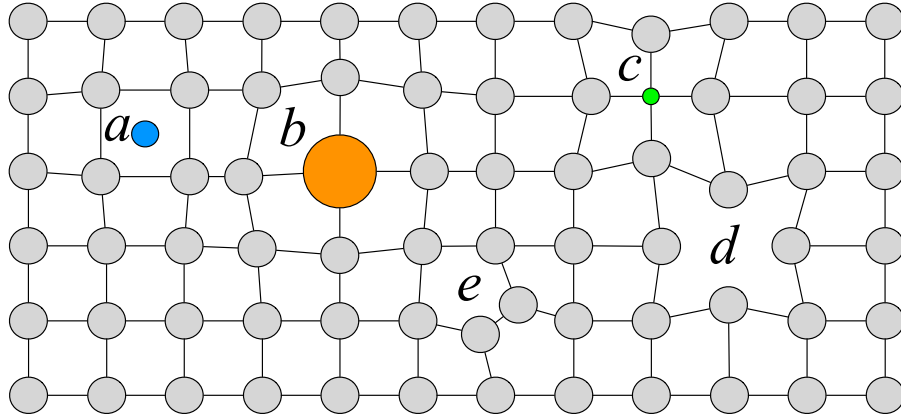


Figure 2.7: Introduction of impurities and non-uniformities into the crystal lattice due to radiation damage.

791 **Radiation damage** The diamond crystal lattice is very strong and uniform. However, when the highly energetic particles or photons impinge the diamond, they can 793 damage the crystal structure. Figure ?? shows several examples of the lattice damage:

- 794 a) foreign interstitial (e.g. H, Li),
- 795 b, c) foreign substitutional (e.g. N, P, B),
- 796 d) vacancy and
- 797 e) self interstitial.

798 These non-uniformities – traps – form new energy levels in the forbidden gap. The 799 drifting charge carriers are stopped by these traps, which in effect reduces the induced 800 current. The energy level of the trapped carrier is reduced from the conduction band 801 to the energy level of the trap. Different types of lattice damage have different energy 802 levels. The release time depends on the level (shallow, deep trap).

803 2.3 Electronics for signal processing

804 This section describes the electronics of a detector, starting with a description of 805 signal amplifiers and then discussing the digitisation and signal processing. All these 806 stages are necessary to extract information from the sensor. First, the signal has to be 807 amplified. Then it is digitised and finally processed in a specially designed processor 808 or a logic unit.

809 2.3.1 Signal preamplifiers

810 The signal charge generated in the sensor by a single highly energetic particle or 811 photon is of the order of fC. The induced current is ranging between 10^{-8} A (β, γ

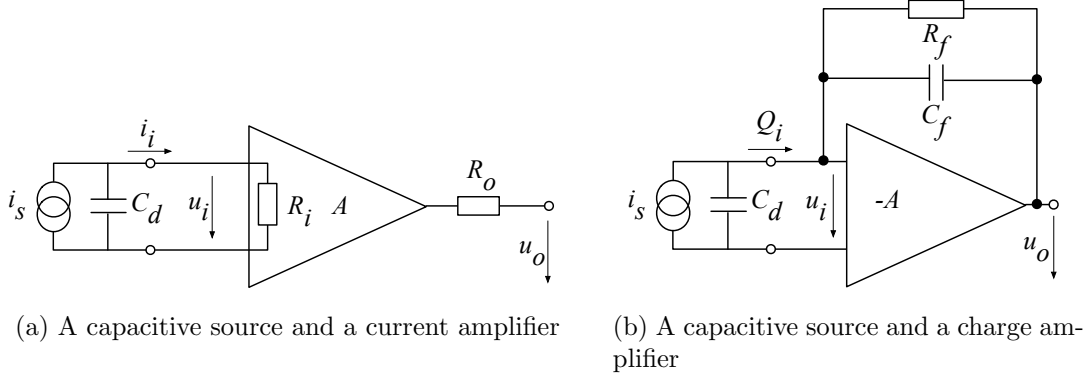


Figure 2.8: Simplified equivalent circuits of a current and charge amplifier

radiation) and 3×10^{-7} A (α radiation). Signals as low as these have to be pre-amplified before processing. Depending on the measurement, several types of signal amplifiers can be used. The preamplifiers have to be designed carefully to minimise electronic noise while maximising gain – thus maximising the signal-to-noise ratio (SNR). In addition, they have to have a high bandwidth limit because the signals from the diamond sensors are very short. A critical parameter is the total capacitance, i.e. sensor capacitance and input capacitance of the preamplifier. The SNR improves with a lower capacitance. Several types of amplifiers can be used, all of which affect the measured pulse shape. They behave differently for resistive or capacitive sources. Given that semiconductors are capacitive sources, we will focus on these. Two preamplifiers are used most commonly, a current and a charge amplifier. Both are described below in detail.

2.3.1.1 Current-sensitive amplifier

Figure 2.8a shows the equivalent circuit of a capacitive source and a current amplifier. An amplifier operates in current mode if the source has a low charge collection time t_c with respect to the $R_i C_d$ time constant of the circuit. In this case the sensor capacitance discharges rapidly and the output current i_o is proportional to the instantaneous current i_i . The amplifier is providing a voltage gain, so the output signal voltage u_o is directly proportional to the input voltage u_i :

$$u_o(t) = A \cdot R_i \cdot i_s(t). \quad (2.14)$$

The detector capacitance C_{det} together with the input resistance of the amplifier R_i defines the time constant of the signal (see figure 2.9). The higher the C_{det} is, the slower will be the response of the amplifier. For the case of the diamond sensor, which has the capacitance of the order of 2 pF and the input resistance of 50 Ω , the resulting time constant is $\tau = 10^{-10}$ s. This yields the signal rise time $t_r \sim 2.2\tau = 0.22$ ns.

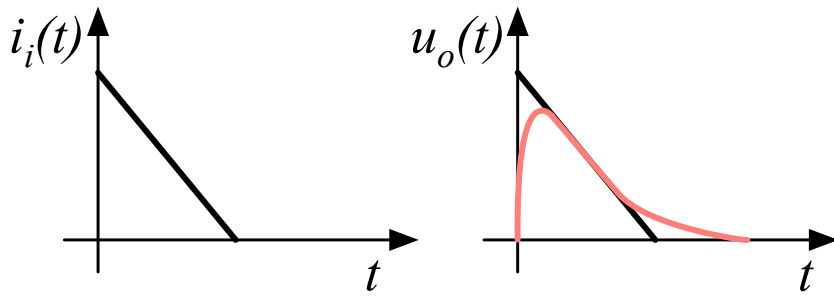


Figure 2.9: Input and output signal of the current amplifier

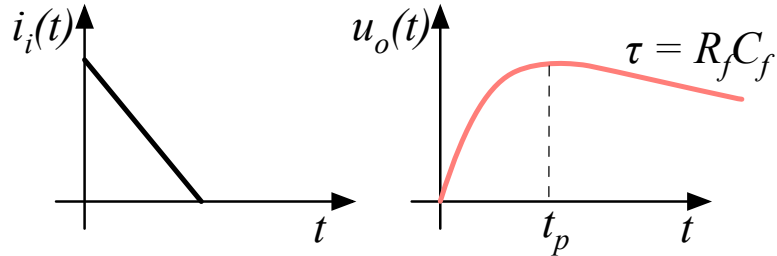


Figure 2.10: Input and output signal of the charge amplifier

836 2.3.1.2 Charge-sensitive amplifier

837 In order to measure integrated charge in the sensor, a feedback loop is added to the
838 amplifier (see figure 2.8b). The feedback can be used to control the gain and input
839 resistance, as well as to integrate the input signal. The charge amplifier is in principle
840 an inverting voltage amplifier with a high input resistance.

841 In an ideal amplifier the output voltage u_o equals $-Au_i$. Therefore the voltage
842 difference across the capacitor C_f is $u_f = (A + 1)u_i$ and the charge deposited on the
843 capacitor is $Q_f = C_f u_f = C_f(A + 1)u_i$. Since no current can flow into the amplifier,
844 all of the signal current must charge up the feedback capacitance, so $Q_f = Q_i$.

845 In reality, however, charge-sensitive amplifiers respond much slower than is the
846 duration of the current pulse from the sensor. In addition, a resistor is added to the
847 feedback line in parallel to the capacitor. The resistor and capacitor define the decay
848 time constant of the pulse (see figure 2.10). This is necessary to return the signal to
849 its initial state and ready for a new measurement.

850 **2.3.1.3 Analogue electronic noise**

851 Electronic noise determines the ability of a system to distinguish signal levels. The
 852 analogue signal contains a lot of information, which can quickly be erased or altered
 853 if the signal properties change. It is therefore instrumental to understand the noise
 854 contributions to the signal to qualify the information it carries. There are several
 855 noise contributions, of which the important ones are listed below. The thermal noise
 856 is the dominant noise contribution in the use case for diamond detector signal ampli-
 857 fication and therefore defines the limitations of the detector system. Thermal noise
 858 or Johnson–Nyquist [] noise is generated by the random thermal motion of charge
 859 carriers in the conductor. The frequency range of the thermal noise is from 0 to
 860 ∞ with a more or less uniform distribution. Therefore this is nearly a white noise.
 861 The resulting signal amplitude has a Gaussian distribution. The RMS of the noise
 862 amplitude is defined as

$$u_{\text{RMS}} = \sqrt{4k_B RT \Delta f} \quad (2.15)$$

863 where k_B is the Boltzmann constant, R is the resistance of the conductor, T its
 864 temperature and Δf the frequency range. This equation shows that it is possible to
 865 reduce the noise RMS by either (1) reducing the frequency range, (2) reducing the
 866 resistance of the conductor or (3) cooling the conductor.

867 Contributions of shot noise, flicker noise and burst noise and other types are not
 868 significant relative to the thermal noise. However, the contributions of external factors
 869 can severely deteriorate the signal. This means the noise produced by capacitive or
 870 inductive coupling with an external source, which causes interference in the signal.
 871 These effects can be reduced by shielding the electronics and avoiding ground loops.

872 **2.3.2 Analogue-to-digital converters**

873 An analogue-to-digital converter (ADC) is a device that converts the analogue elec-
 874 trical signal on the input to its digital representation - a series of digital values. This
 875 involves a quantisation – *sampling* of the signal at a defined sampling period, resulting
 876 in a sequence of samples at a discrete time period and with discrete amplitude values.
 877 The resolution of the ADC is the number of output levels the ADC can quantise to
 878 and is expressed in bits. For instance, an ADC with a resolution $n = 8$ bit will have
 879 the dynamic range $N = 2^n = 256$ steps. The resulting voltage resolution Q_{ADC} at
 880 the input voltage range of $V_{\text{ADC}} = \pm 50$ mV is then equal to

$$Q_{\text{ADC}} = \frac{V_{\text{ADC}}}{2^n} = \frac{100 \text{ mV}}{2^8 \text{ steps}} = 0.39 \text{ mV/step.} \quad (2.16)$$

881 With a sampling period of $t_s = 1$ ns this will produce the sampling rate of $f_s = 1$ GSPS
 882 (gigasample per second).

883 **Quantisation error and quantisation noise** (or a round-off error) is a contribu-
 884 tion to the overall measurement error due to digitisation (rounding). It is defined
 885 as a difference between the actual analog value and a digitised representation of this

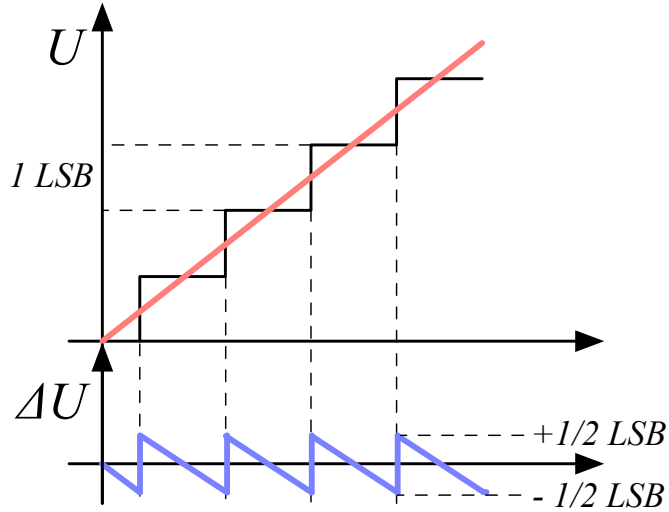


Figure 2.11: Input signal digitisation and quantisation error

886 value. The error is defined by the least significant bit (LSB), as seen in figure 2.11.
 887 Typically, the input signal amplitude is much larger than than the voltage resolution.
 888 Therefore the quantisation error is not directly correlated with the signal and has an
 889 approximately uniform distribution []:

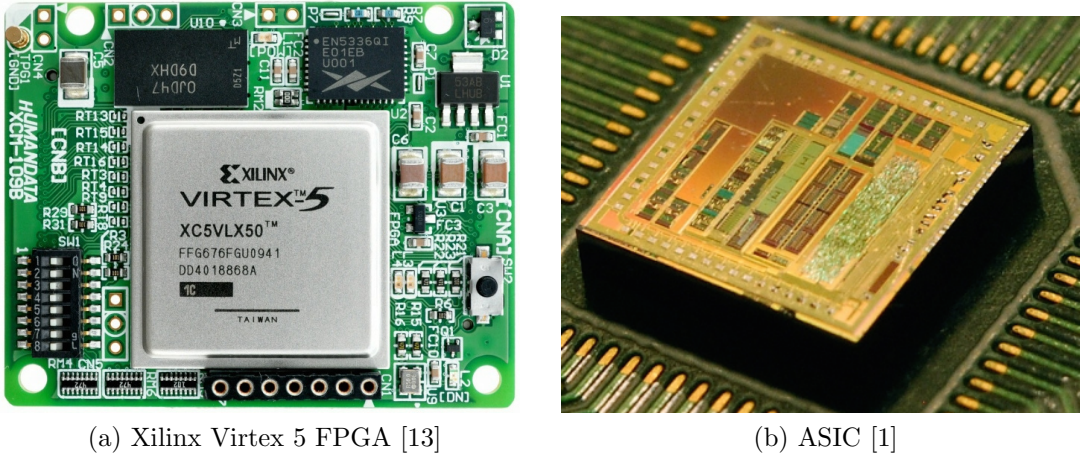
$$\Delta Q_{\text{ADC}} = \frac{1}{\sqrt{12}} \text{ LSB} \sim 0.289 \text{ LSB}. \quad (2.17)$$

890 For the example above the quantisation error will be $\Delta Q_{\text{ADC}} = 0.289 \cdot 0.39 \text{ mV} = 0.11 \text{ mV}$.
 891 The error depends strongly on the linearity of the ADC, but this will not be discussed
 892 in this document as the devices used have ADCs with a linear response.

893 2.3.3 Digital signal processing

894 The digitised signal can be processed to extract useful information. Therefore after
 895 the signal amplification and digitisation the signal is routed in a device which handles
 896 the analysis. The signal can either be processed immediately (in real time) or it can
 897 be saved to a data storage for analysis at a later stage (offline). The devices carrying
 898 out the processing can be multipurpose (e.g. Field programmable gate arrays) or
 899 dedicated (e.g. application-specific integrated circuits). Each of the two has its
 900 advantages and disadvantages, which are listed below.

901 **Field programmable gate array (FPGA)** is an integrated circuit designed to be
 902 reprogrammable and reconfigured after manufacturing. It consists of a set of logic
 903 gates that can be interconnected in numerous combinations to carry out a logic op-
 904 eration. Many such logic operations can take place in parallel, making the FPGA a



(a) Xilinx Virtex 5 FPGA [13]

(b) ASIC [1]

Figure 2.12: An example of an FPGA and an ASIC chip

powerful tool for signal processing. FPGAs are often used during system development or in systems in which the requirements might change with time. They can be reprogrammed in the order of seconds. In addition, the logic design only needs minor changes when migrating to a newer version of the FPGA chip of the same vendor. They also offer faster time-to-market with comparison to application-specific solutions, which have to be developed. On the other hand, the price per part can be significantly higher than for the application-specific solutions. Also, their other major disadvantages are a high power consumption and a relatively low speed. However, today's solutions are capable of clock speeds of the order of 500 MHz. Together with the integrated digital signal processing blocks, embedded processors and other modules, they are already very powerful and versatile. All in all, FPGAs are a good choice for prototyping and limited production, for projects with a limited requirements for speed and complexity.

Application-specific integrated circuit (ASIC) is an integrated circuit designed for a specific use. The design cannot be modified after chip production, as compared to FPGAs. On the other hand, the ASICs can be optimised to perform a required operation at a high speed and at a low power consumption. In addition, due to the specific design the size of the chip can be much smaller. ASICs can be designed as hybrid chips, containing both a digital and an analog part. To update the chip, the design has to be submitted to a foundry, which produces the new chips with a turnover time of 4—6 weeks. The costs of a submission start at \$ 50 000, but the price per part can be reduced significantly with a high volume. To sum up, ASICs are used for high volume designs with well defined requirements where some stringent constraints in terms of power consumption and speed have to be met.

₉₂₉ **Chapter 3**

₉₃₀ **Experimental results**

₉₃₁ ***Diamond irradiation study***

₉₃₂ This chapter contains the measurement results of data taken with diamond sensors.
₉₃₃ First the measurement setup is described (section 3.1). Then the measured particle
₉₃₄ spectra are shown in 3.2. This is followed by a study of effects of irradiation damage
₉₃₅ on the electrical signal of the diamond detector and its lifetime. The last section
₉₃₆ shows the results of the measurements of irradiated diamond samples at cryogenic
₉₃₇ temperatures. The aim of these studies is to find the operational limitations of dia-
₉₃₈ mond detectors for spectroscopy and tracking applications. The studies compare the
₉₃₉ experimentally acquired data with the theory from the previous chapter and define
₉₄₀ limitations of the diamond detectors in terms of noise, radiation and temperature.

₉₄₁ Diamond sensors are mainly used for two types of measurements: particle counting
₉₄₂ and spectroscopy. The first type of measurements depends on the sensor's efficiency –
₉₄₃ the ability to detect all or at least a known percentage of radiation quanta (particles
₉₄₄ or photons) that hit it. The energy of the radiation is not so important; what bears
₉₄₅ the information is the rate and the spatial distribution. Here the radiation does
₉₄₆ not necessarily stop in the bulk, but rather continues its way. In spectroscopy, on
₉₄₇ the other hand, the idea is that a particle stops within the sensor, depositing all
₉₄₈ its energy, which is then measured via the freed charge carriers. The aim of the
₉₄₉ experiments described in this chapter is to:

- ₉₅₀ 1. Quantify the efficiency of the sCVD diamond in counting mode,
- ₉₅₁ 2. Quantify the degradation of efficiency with respect to the received radiation
₉₅₂ dose,
- ₉₅₃ 3. Quantify the macroscopic effects on charge carrier behaviour with respect to
₉₅₄ the received radiation dose and
- ₉₅₅ 4. Define limitations for its use in spectroscopy.

₉₅₆ The results discussed here show that there are several limitations for using diamond as
₉₅₇ a measurement device. All of them need to be taken into account for the measurement

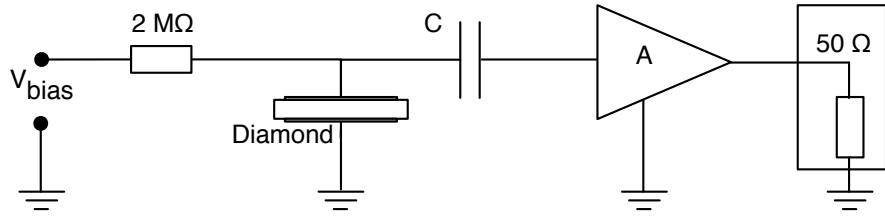


Figure 3.1: Diagram of a diamond detector readout chain.

device to perform reliably and stably. The first step is to build a setup that is insensitive to external electromagnetic interferences and minimises electrical noise in the system. The setup needs to be calibrated before use. Then, the measurement conditions have to be defined, such as the temperature, the type of radiation and its flux. This allows us to estimate the lifetime of the detector and predict the longterm change of the signal. This change can then be accounted for when interpreting the output data.

3.1 Measurement setup

To get reliable measurement results, great care has to go towards designing a measurement setup that minimises the noise in the measurements. Shielding has to be applied wherever possible. For instance, aluminium foil can be wrapped around the exposed parts of the system to shield them from external radio-frequency (RF) interferences. In addition, the sensors have to be covered to prevent the light from shining directly onto them. The incident photons can deposit enough energy to increase the leakage current of the detector.

The measurements using diamond that are explained in these chapters were carried out using several measurement setups, but they are all similar in terms of the electrical signal chain. The measurement chain consists of three main parts: a diamond sensor, a signal preamplifier and a readout device, as seen in diagram 3.1. The signals propagating along the analogue chain (before being digitised by the readout device) are fast – in the GHz bandwidth range – and with low amplitudes – of the order of tens of μV . This gives rise to importance of RF shielding. Also, the connection between the carrier and the preamplifier has to be as short as possible to avoid capacitive signal losses in the transmission line. Finally, the system needs to be grounded properly.

3.1.1 Preamplifiers

Two preamplifiers are used for the measurements, one sensitive to charge and the other to current. *CIVIDEC Cx* (figure 3.2a) is a charge sensing amplifier. Its high SNR (equivalent noise charge of $300 + 30 \text{ pF}^{-1} \text{ e}^-$ and a reported gain of $\sim 12 \text{ mV/fC}$) makes it a good choice for spectroscopic measurements with diamond

3.1. MEASUREMENT SETUP

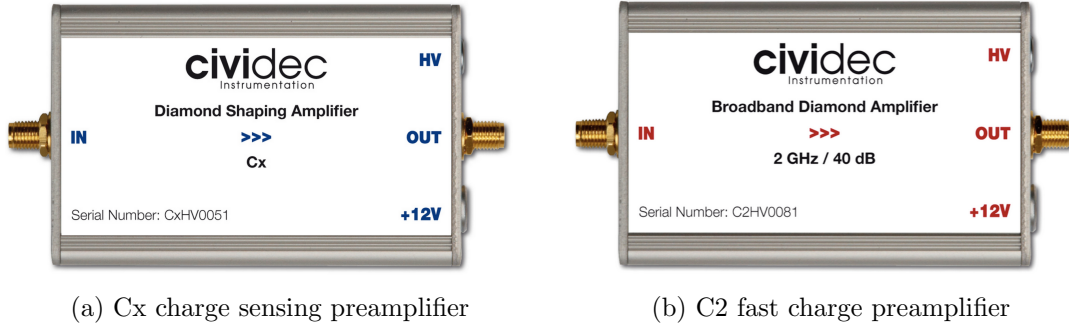


Figure 3.2: Amplifiers used for the charge and current measurements

987 sensors. *CIVIDEC C2* (figure 3.2b) is a fast current preamplifier with a 2 GHz band-
 988 width limit. It is used for TCT measurements because of its fast response and a good
 989 SNR. Both are embedded in an RF-tight aluminium box to reduce the noise pickup.
 990 Both have an AC coupled input and an output with a 50Ω termination.

991 3.1.1.1 Calibration

992 The amplifiers have to be calibrated before use to determine their gain. Both are
 993 calibrated using a square signal generator with a known amplitude step of $U_{\text{in}} =$
 994 (252 ± 5) mV. A 2 GHz oscilloscope with a 10 GS/s sampling is used to carry out
 995 these measurements.

996 In the case of the Cx charge sensitive amplifier, the signal is routed through a
 997 capacitor with a calibration capacitance $C_{\text{cal}} = (0.717 \pm 0.014)$ pF and then to the
 998 input of the amplifier. The pulse area behind the capacitor is $a_{\text{cal}} = (5.0 \pm 0.5)$ pVs,
 999 with the signal amplitude on the output amounting to $U_{\text{Cx}} = (1.95 \pm 0.05)$ V. The
 1000 input voltage step combined with the calibration capacitance yields a calibration
 1001 charge $Q_{\text{cal}} = C_{\text{cal}} \cdot U_{\text{in}} = (181 \pm 5)$ fC. The gain of the Cx amplifier is therefore
 1002 $A_{\text{Cx}}^Q = \frac{U_{\text{Cx}}}{Q_{\text{cal}}} = (9.3 \pm 0.4)$ mV/fC or $A_{\text{Cx}}^a = \frac{U_{\text{Cx}}}{a_{\text{cal}}} = (390 \pm 40)$ mV/pVs. The area-based
 1003 amplification factor has a higher uncertainty ($\sim 10\%$) than the amplitude-based
 1004 factor ($\sim 4\%$) due to the measurement limitations of the oscilloscope. Nevertheless,
 1005 it can be used as an estimate for the integrated charge of a current pulse.

1006 To calibrate the C2 current amplifier, only the amplitude gain has to be measured.
 1007 The input signal amplitude has to be such that it keeps the output amplitude within
 1008 the amplifier's linear range, that is ± 1 V. The signal from the generator is therefore
 1009 routed through a 36 dB attenuator to decrease its amplitude to $U_{\text{inAtt}} = (3.95 \pm$
 1010 $0.05)$ mV. Two amplifiers with different gains have been measured, because both
 1011 are used for the measurements at different times. The output of the first amplifier
 1012 amounts to $U_{\text{C2-1}} = (860 \pm 5)$ mV. This yields the amplification gain equal to $A_{\text{C2-1}} =$
 1013 $\frac{U_{\text{inAtt}}}{U_{\text{C2-1}}} = (217 \pm 3)$. The second amplifier has the output equal to $U_{\text{C2-2}} = (632 \pm 5)$ mV
 1014 with the gain equal to $A_{\text{C2-2}} = (152 \pm 3)$.

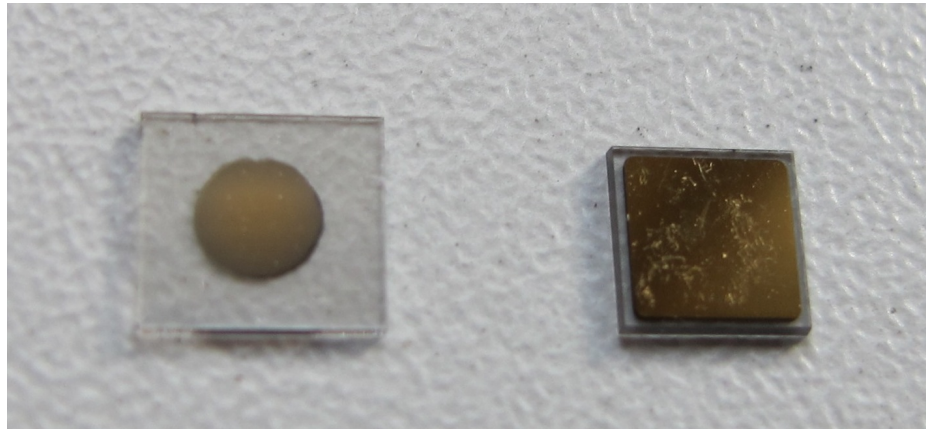


Figure 3.3: Two scCVD diamond samples: A IIa 1scdhq (left) and an E6 S37 (right)

3.1.2 Diamond samples

Detector-grade diamonds are very difficult to produce, mostly because it is very difficult to ensure a high enough purity of the lattice. The sensor samples used for these studies were bought at Element Six (E6) [5]. They all have the same standard dimensions. sCVD diamonds with dimensions $4.7 \times 4.7 \text{ mm}^2$ are already sufficiently large for most of the beam monitoring applications and still affordable. One of the samples with dimensions of $5.6 \times 5.3 \text{ mm}^2$ produced by IIa Singapore [7] was also sent to CERN to be characterised. The target thickness for all the samples is $500 \mu\text{m}$. Diamonds this thick yield a high enough signal-to-noise ratio for MIPs to be measured by the electronics. Table 3.1 shows all the samples used for this study. Two of them were later irradiated with 300 MeV pions and then compared to the pre-irradiated state. Irradiation doses for damaging the material need to be high – above 10^{12} particles per cm^2 to be able to observe change in the sensor’s behaviour.

Name	Type	Producer	Dimensions [mm^2]	Thickness [μm]	Electrode	Irradiated
S37	sCVD	E6	4.7×4.7	548	Cr/Au	no
S50	sCVD	E6	4.7×4.7	537	Cr/Au	no
S52	sCVD	E6	4.7×4.7	515	Cr/Au	$1 \times 10^{14} \pi \text{ cm}^{-2}$
S79	sCVD	E6	4.7×4.7	529	Cr/Au	$3.63 \times 10^{14} \pi \text{ cm}^{-2}$
ELSC	sCVD	E6	4.7×4.7	491	Cr/Au	no
1scdhq	sCVD	IIa	5.6×5.3	460	Cr/Au	no

Table 3.1: Diamond sensor samples used

The diamond samples have quoted impurity densities of $\leq 2 \times 10^{14} \text{ cm}^{-3}$ and nitrogen incorporation of $\leq 1 \text{ ppb}$. The electrodes were added by various companies and institutes. For instance, S52 was metallised by a company DDL (now defunct) while the Physics Department of the University of Firenze, Italy metallised the S79. There are also several techniques for producing the electrodes. The DDL contacts consist of three layers: DLC (diamond-like carbon)/Pt/Au with 4/10/200 nm thicknesses, respectively. The metallisation for S79, on the other hand is made up of Cr/Au with

3.1. MEASUREMENT SETUP

1038 a total thickness of \sim 400 nm. The area coverage also differs from sample to sample.
1039 Diamonds must not be metallised until the very edge as the proximity of contacts
1040 with a high potential can lead to sparking. However, the areas not covered by the
1041 metallisation are less efficient because the fringe fields at the edges are not as strong
1042 as in the middle. This effectively reduces the sensitive area of the sensors. In the
1043 diamonds used here the effective area was anywhere from 9 mm^2 to 18 mm^2 . Leakage
1044 current through the bulk was below 1 ns, but increased for the irradiated samples.
1045 The capacitance was of the order of $(2.0 \pm 0.3)\text{ pF}$.

1046 3.1.3 Readout devices

1047 Electrical signals in diamond detectors are in the GHz frequency range. To preserve
1048 this information, the readout device has to have a high bandwidth limit. For in-
1049 stance, a 250 MHz limit is enough for the spectroscopic measurements with the Cx
1050 charge amplifier, but might be insufficient for the current measurements with the C2
1051 amplifier. Two devices are used take data shown in this chapter. The first choice is a
1052 2 GHz LeCroy WaveRunner 204MXi-A. This specific model has a high enough limit
1053 for the fast current preamplifier signals. It offers a versatile solution for analogue sig-
1054 nal readout – it is fast to set up and reliable. It is very convenient for use in lab tests
1055 and for experiments where small amounts of data are taken and where speed is not
1056 crucial. However, its slow acquisition speed turns out to be a bottleneck in the test
1057 beam experiment. Its initial 100 Hz readout rate decreases to a mere 20 Hz within
1058 20 minutes, because every single trigger is saved as a separate file and the Windows
1059 operating system is not capable of handling 10000+ files in a single directory eas-
1060 ily. This is why it has been exchanged with a DRS4 [4], an analogue readout device
1061 developed by PSI, Switzerland. This compact device is capable of recording up to
1062 four waveforms at a time at a steady rate of up to 500 Hz. Its 700 MHz bandwidth
1063 limitation is sufficient for the signal from the charge amplifier.

1064 3.1.4 Setup for the efficiency study using β particles

1065 The efficiency study of the diamond sensors has been carried out at CERN in the
1066 North Hall test beam facility. There a straight high-energy particle beam of $\pi_{120}\text{ GeV}$
1067 is provided to the users to calibrate their detectors. The beam had a transverse spread
1068 of $\sigma = 10\text{ mm}$ in both axes. The particle rate is of the order of $10^4\text{ }\pi\text{ cm}^{-2}\text{ s}^{-1}$. A
1069 diamond sensor embedded in a PCB carrier has been placed in the beam spot per-
1070 pendicular to the beam and connected via an SMA connector directly to a charge
1071 amplifier (described below). The amplified signal is read out using a LeCroy oscil-
1072 loscope and a DRS4 analogue readout system (both described below). A computer
1073 is used as a controller and data storage for the readout device. A beam telescope is
1074 used as a reference detector. It is a device that helps to cross-check the measurements
1075 of the devices under test (DUTs) and to carry out spatially resolved studies on the
1076 DUTs. It consists of several pixellated sensor planes placed in series, which can track
1077 a particle's trajectory with a precision of a few μm . The sensor planes are positioned

in front of the DUT and behind it. Then the beam telescope acts as a trigger system – it triggers the readout of both the telescope data and DUT data when both the planes in front and behind the DUT recorded a hit by the incident particle. A particle detected by all the planes within the DUT window and the DUT itself counts towards its efficiency whereas a hit missed by the DUT means that the DUT is not 100 % efficient. To discard the hits that miss the DUT completely, a region of interest (ROI) can be chosen in the beam telescope planes. The equation for calculating the sensor efficiency is therefore

$$\epsilon = \frac{N_{\text{DUT}} \wedge N_{\text{telescope}}}{N_{\text{telescope}}} \quad (3.1)$$

for an ROI smaller than the sensitive region of the diamond.

3.1.5 Room temperature α -TCT setup

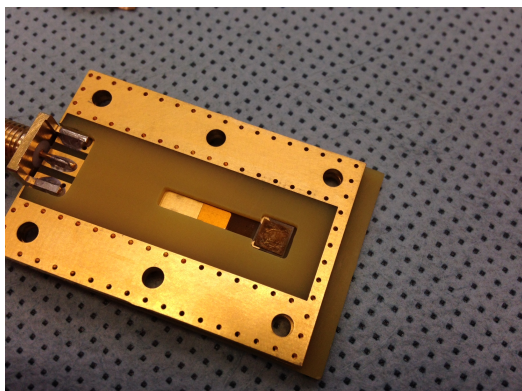
This TCT study is a follow-up of an extensive diamond TCT study at cryogenic temperatures [28]. The room-temperature TCT measurements have been carried out in the lab. The setup consists of a diamond sensor embedded in a PCB carrier, a current amplifier and an oscilloscope. To measure α particles, their energy loss during their trajectory has to be minimised. Therefore the diamond is placed inside a vacuum chamber. The chamber is a steel tube with a diameter of 5 cm. On one side it is connected to a vacuum pump via a steel pipe. A feedthrough with an SMA connector is placed on the other side. A C2 current amplifier is connected directly onto the feedthrough. The amplified output is connected to the oscilloscope via an SMA cable. An ^{241}Am source with a diameter of 2 cm and a height of 0.5 cm is fixed onto the sensor carrier (figure 3.4a, figure 3.4b). Then the carrier is inserted in the chamber and fixed in place using an air-tight clamp. The pump can then be switched on. It is capable of providing the inside pressure as low as 10^{-4} mbar after approximately one hour of operation, but measurements can take place even after five minutes of evacuation, at around 10^{-3} mbar. The most important thing to bear in mind is to switch the bias voltage of the sensor OFF during the process of evacuation, because the gas becomes more conductive at the pressure of the order of 10^{-1} mbar, which is at the bottom of Paschen's curve [21]. A failure to switch off the bias voltage may cause a spark between the signal and ground line, destroying the amplifier.

3.1.6 Cryogenic α -TCT setup

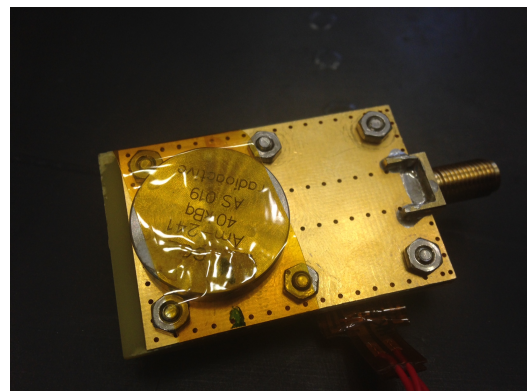
The experiment at cryogenic temperatures has been carried out in the cryolab at CERN. The room-temperature TCT setup has to be modified to allow for measurements at temperatures as low as 2 K. It consists of three parts:

1. a cryostat – a thermally insulated cylinder capable of containing liquid helium,
2. an inlet – an air-tight mechanical tube with valves and feedthroughs at the top that is lowered in the liquid helium and

3.1. MEASUREMENT SETUP



(a) PCB carrier with an embedded diamond sample



(b) Radioactive source over the carrier

Figure 3.4: Positioning of the α -source on top of the sensor carrier

1114 3. the diamond sample embedded in a PCB carrier with a fitted temperature
1115 sensor, a heater and cables leading to the feedthroughs.

1116 The setup is described in detail in [28].

1117 When the diamond sample is placed in the PCB carrier and the ^{241}Am source is in
1118 place, the inlet is sealed and lowered in the empty cryostat. Then the inside volume
1119 of the inlet is evacuated to down to 10^{-5} mbar while the liquid helium is flowing into
1120 the cryostat. To improve the thermal contact between the diamond and the coolant,
1121 a small amount of helium gas is added inside the evacuated inlet, setting the vacuum
1122 to around 10^{-3} mbar. This value changes with time, because the gas condenses on
1123 the walls of the inlet, reducing the number of floating particles. For this reason the
1124 helium gas has to be added on an irregular basis. Every addition causes a significant
1125 undershoot of the sample temperature, which had to be corrected for using a heater
1126 placed on the back of the PCB carrier. Also, the added gas deteriorates the vacuum
1127 inside the inlet. It is very important to monitor the pressure so as not to let it rise
1128 above 10^{-2} mbar. The gas at this pressure is significantly more conductive and could
1129 cause a short circuit between the two diamond plates or in the SMA connectors,
1130 destroying the amplifier. Furthermore, at approximately 60 K the helium gas has to
1131 be evacuated from the inlet to avoid a potential explosion due to the expansion of
1132 the gas with temperature.

1133 When the sample is cooled to the minimum temperature achievable by means
1134 of liquid helium without over-pressurising it (4.2 K), the measurements start. A
1135 temperature sensor placed on the back of the PCB carrier is used to measure the
1136 temperature of the sample. After every temperature data point, the current through
1137 the heater placed in the PCB next to the diamond sample is increased, warming up
1138 the sample. The initial temperature time constant of the order of tenths of seconds at
1139 low temperatures increases with temperature. Even more so when helium is evacuated
1140 from the inlet at 60 K, removing the thermal bridge between the wall of the inlet and
1141 the diamond sample. At the room temperature (RT), the time constant increases to

1142 the order of minutes.

1143 3.2 Charged particle pulses and spectra

1144 In previous chapter the ionisation profiles for different types of radiation were dis-
1145 cussed. It is known that β and γ radiation induces a triangular electric pulse whereas
1146 α radiation induces a rectangular one. However, their amplitude, width and rise/fall
1147 time depend heavily on the type of interaction with the diamond, the purity of the
1148 diamond and the bandwidth of the amplifier and the oscilloscope. This section shows
1149 the signal pulses of α , β and γ radiation with their respective energy distributions for
1150 the case of a diamond detector. Then follows a discussion of effects of noise on these
1151 measurements.

1152 A CIVIDEC C2 current amplifier together with the LeCroy oscilloscope (both
1153 with a bandwidth limit of 2 GHz) has been used to record the pulse shapes whereas
1154 the Cx charge amplifier is used for charge measurement. A 2 GHz bandwidth limit
1155 defines the minimum rising time equal to $t_r \simeq \frac{0.34}{BW} = \frac{0.34}{2 \times 10^9} = 170$ ps, therefore
1156 the system is capable of measuring pulses with a minimum FWHM $\simeq 170$ ps. This
1157 already makes it impossible to measure the initial peak in the α response due to the
1158 two flavours of charge carriers travelling. If a charge carrier travelling through the
1159 bulk takes $t_{t1} \sim 6$ ns to get to the electrode on the other side ($d_1 \sim 500$ μm), the
1160 carrier with the opposite charge and a shorter path to the closer electrode – max.
1161 $d_2 \sim 10$ μm – only takes $t_{t2} \sim \frac{d_2}{d_1} t_{t1} = 120$ ps. A drift time this short induces a
1162 current pulse that is too narrow for the C2 amplifier or the oscilloscope to be able to
1163 observe.

1164 Figure 3.5 shows a set of pulses and an averaged pulse for α , β and γ radiation
1165 using an ^{241}Am , ^{90}Sr and ^{60}Co source, respectively. The particles are measured with
1166 the non-irradiated sCVD diamond S37. α particles always produce the same signal
1167 pulse, but with a high noise RMS. The averaging suppresses the noise while still
1168 retaining most the information. It does, however, smear the rising and falling edge,
1169 increasing the rise time. The t_r is now of the order of 0.5 ns. Both β and γ pulses
1170 look similar – triangular and with a wide range of amplitudes. Here the pulse count
1171 is low, so the pulses with a high amplitude are not recorded. A trigger set very high
1172 would be needed to “catch” them with the oscilloscope.

1173 3.2.1 Noise limitations

1174 Noise is a major limiting factor in particle detection. It defines the minimum measur-
1175 able particle energy and the minimum measurement resolution. It is hence important
1176 to minimise the electric noise in the detector signal. The major noise contribution
1177 comes from poor shielding from external electromagnetic sources. These often cause
1178 ringing, whereby the signal oscillates with a frequency defined by the external source.
1179 The ringing makes high-frequency measurements impossible. Another source of noise
1180 is the sensor itself. In the case of silicon, natural light increases the number of ther-

3.2. CHARGED PARTICLE PULSES AND SPECTRA

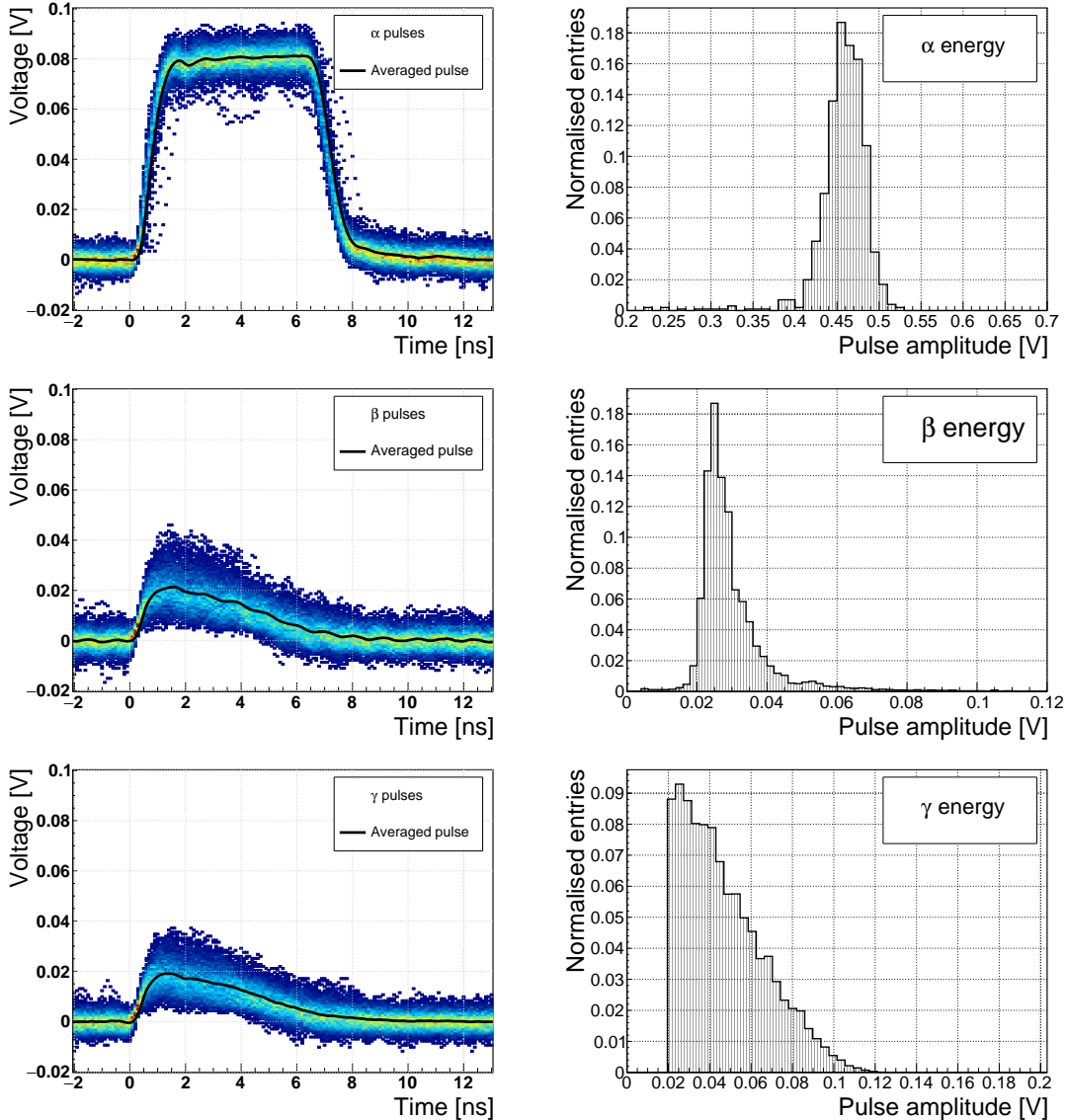


Figure 3.5: Superimposed and averaged pulses (a, b and c, current amplifier) and distributions of deposited energy (d, e, f, charge amplifier) for three types of radiation. Note the scale on the X axis of the distributions.

1181 mally excited free charge carriers, increasing the leakage current. This is not the
 1182 case for diamond, which is with its high energy band gap insensitive to visible light.
 1183 Nevertheless, any noise produced by the sensors is amplified by the signal amplifiers,
 1184 which add an additional noise of the analogue electrical circuit to the amplified
 1185 signal. Finally, the digitisers add the quantisation noise to the digitised signal. If
 1186 the measurement range is significantly higher than the actual measured signal, the
 1187 quantisation noise can be a significant contributor to the decrease of the overall mea-
 1188 surement resolution.

1189 **3.3 Radiation limitations**

1190 Exposure to ionising radiation degrades sensors. It deforms the lattice by displacing
1191 the atoms. Various types of lattice defects can be created in diamond, similar to those
1192 in silicon: vacancies, interstitials etc. [31] These deformations introduce new discrete
1193 energy levels between the valence and conduction band. Charge carriers drifting in
1194 their vicinity can get trapped, their energy falling to the energy level of the trap.
1195 Their emission back to the conduction band depends on how deep the trap is (how
1196 far away from the conduction band it is). The carriers caught in the shallow traps of
1197 the order of 100 meV below the conduction band are excited back up already by means
1198 of the thermal excitation. This phenomenon has a short time constant, dependant
1199 on the environmental temperature. Those stopped by deep traps near the middle
1200 of the band gap need more energy and thus more time to be emitted to either the
1201 conduction or valence band. Some charge carriers remain trapped for long periods.
1202 If they build up in a certain region of the diamond, their charge starts affecting the
1203 surrounding electric field – space-charge forms. It can either help or counteract the
1204 field, depending on the polarity of the carrier.

1205 The energy band jumping goes the other way, too. The carriers in the valence
1206 band may use the intermediate energy levels as “stepping stones” to jump to the
1207 conduction band and start drifting in the externally applied electric field. This is
1208 called the leakage current.

1209 The electrons and holes stopped in these traps cause a decrease of the induced
1210 current on the electrodes. This yields a lower integrated charge in an irradiated sensor
1211 than that in a non-irradiated one. Charge collection efficiency is therefore correlated
1212 with the level of irradiation.

1213 This section contains a study of the effects of pion ($\pi_{300 \text{ MeV}}$) irradiation on the
1214 charge collection efficiency of sCVD diamond detectors. To carry out this study,
1215 two diamond samples have been irradiated to doses of $1 \times 10^{14} \pi \text{ cm}^{-2}$ (S79) and to
1216 $3.63 \times 10^{14} \pi \text{ cm}^{-2}$ (S52). Then a test beam campaign has to be carried out to observe
1217 the charge collection efficiency at different bias voltage settings. The efficiency values
1218 acquired are used to determine the effective drop in efficiency with respect to received
1219 radiation dose. This is to test if the collected charge Q is inversely proportional to
1220 the received dose Φ . A procedure defined by a collaboration researching diamond
1221 behaviour RD42 has been applied to the measured values to extract the damage factor.
1222 The next subsection contains measurements and results of a long-term stability study
1223 using α and β particles. In particular, the charge collection efficiency as a function
1224 of time is measured during the measurements with β and α radiation. To investigate
1225 this effect on the scale of charge carriers, the change of TCT pulses with time is
1226 observed. Finally, a procedure that improves the pulse shape and with it the charge
1227 collection is proposed.

3.3. RADIATION LIMITATIONS

3.3.1 Quantifying radiation damage in diamonds

Radiation damage varies with the type of radiation (particles or photons) and its energy. There are several models existing [27, 26] that try to explain the impact of irradiation and to provide *hardness factors* to compare the radiation damage between different particles. The standard way is to convert the damage into *neutron equivalent* [14]. Some models have been extensively verified with simulations and with experiments. In these experiments charge collection in sensors is measured before and after irradiation. This procedure is repeated several times, with a measurement point taken after every irradiation. When a set of measurements of charge collection is plotted against the radiation dose received by a specific particle at a specific energy, a damage factor k_λ can be extracted. Damage factors have to be measured across a range of energies and types of radiation to properly quantify the damage in the sensors. They are then compared against the simulations to verify that the experimental observations are in line with the theory.

Diamond is an expensive material and the technology is relatively new as compared to silicon. Therefore not many institutes are carrying out diamond irradiation studies. To join the efforts, the RD42 collaboration [11] was formed. It gathers the experimental data from diamond irradiation studies. Unlike with silicon, the experimental results so far show no significant correlation with the NIEL (non-ionising energy loss) model [27], which correlates detector efficiency with the number of lattice displacements. Therefore an alternative model was proposed [26], correlating the diamond efficiency with the number of displacements per atom (DPA) in the bulk. The idea is that if the recoil energy of an incident particle is higher than the lattice binding energy (42 eV for diamond), the atom is displaced from its original position. The newly formed vacancy acts as a trap for drifting charge carriers. The more displacements that form in the bulk, the higher is the probability that a drifting carrier will get trapped, effectively reducing the induced signal. However, different types of particles interact differently with the bulk. In addition the mechanisms of interaction at low energies are different to those at high energies. To assess the damage for individual particles at a range of energies, simulations need to be run first. The simulation shown in [26] shows the DPA model for a range of energies of proton, pion and neutron irradiation in diamond. Figure 3.6 contains the simulation results as well as the superimposed empirical results of several irradiation studies. According to the figure, a 300 MeV pion beam damages the diamond bulk twice as much as a 24 GeV proton beam. The data points obtained by RD42 are also added to the figure. They have been normalised to damage by 24 GeV protons. Finally, the data point measured in the scope of this thesis has been added for comparison. The derivation is done below.

3.3.1.1 Irradiation with a $\pi_{300 \text{ MeV}}$ beam

The samples were irradiated at the Paul Scherrer Institute (PSI) [10] by means of a beam of pions with an energy of 300 MeV (kinetic energy 191.31 MeV) and with a

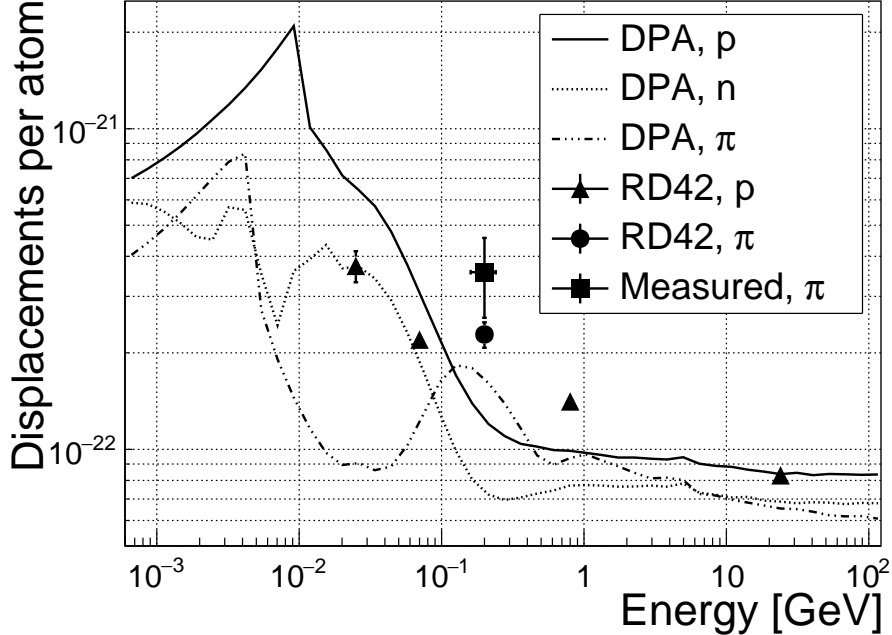


Figure 3.6: Diamond radiation damage - a model based on displacements per atom [26]. Added are data points for protons and pions by RD42 [35] and one data point for pions measured in the scope of this thesis.

flux of up to $1.5 \times 10^{14} \pi \text{ cm}^{-2}$ per day. The system has a 10 % uncertainty on the beam energy. In addition, their quoted uncertainty on the measurement has an error of $\pm 20\%$. Looking at the pion damage curve in figure 3.6, $\pi_{300 \text{ MeV}}$ point sits on a steep section of the DPA curve. This means that a deviation in beam energy can have a significant effect on the damage.

Two diamond samples, S52 and S79, were put in the $\pi_{300 \text{ MeV}}$ beam in the 2014 PSI irradiation campaign; S52 to $(1 \pm 0.21) \times 10^{14} \pi \text{ cm}^{-2}$ and S79 to $(3.63 \pm 0.77) \times 10^{14} \pi \text{ cm}^{-2}$. During the process, the golden electrodes got slightly activated, but the activation decayed in two weeks.

3.3.1.2 Charge collection efficiency and charge collection distance

Three diamonds – non-irradiated S37 and irradiated S52 and S79 – were tested in a $\pi_{120 \text{ GeV}}$ test beam in the SPS North Experimental Area at CERN [18] before and after irradiation. The goal was to estimate the charge collection efficiency (CCE) and charge collection distance (CCD) as a function of irradiation dose. The samples were primed (pumped) prior to data taking using a ^{90}Sr radioactive source. The data were then taken at a range of bias voltages ranging from 30 V to 900 V, yielding between 0.06 V/ μm and 1.8 V/ μm electrical field in the bulk. Every data point contained approximately 5×10^4 measured particles. The charge deposited by the particles was measured using a CIVIDEC Cx charge preamplifier. As expected, the integrated

3.3. RADIATION LIMITATIONS

1288 amplitude spectrum followed a landau distribution. Its most probable value (MPV)
 1289 was used to calculate the most probable collected charge Q_i :

$$Q_i [e^-] = \frac{Q_i [fC]}{1.6 \times 10^{-4}} = \frac{MPV [mV]}{A [mV/fC]} \cdot 6.241 \times 10^4 \quad (3.2)$$

1290 where $A = 9.2 \text{ mV/fC}$ is the preamplifier gain factor. The CCD was then calculated
 1291 using the average number of electron-hole pairs produced per micrometer in diamond
 1292 $\delta_d = 36 \text{ e-h } \mu\text{m}^{-1}$ (from table 5.2):

$$CCD = \frac{Q_i}{\delta d} \quad (3.3)$$

1293 The resulting CCD for the three measured samples at bias voltages ranging from
 1294 $0.2\text{--}1.6 \text{ V } \mu\text{m}^{-1}$ is shown in figure 3.7a. S37 exhibits a full collection distance already
 1295 at $0.4 \text{ V } \mu\text{m}^{-1}$ whereas the irradiated samples have a more gentle increase of CCD
 1296 with increasing bias voltage. It is evident that at $1 \text{ V } \mu\text{m}^{-1}$ the maximum CCD has
 1297 not been reached in the case of S79 and S52. Nevertheless, to compare the measured
 1298 data point with those provided by RD42, the CCD at $1 \mu\text{m}$ has to be taken.

1299 3.3.1.3 Irradiation damage factor

1300 The irradiation damage factor k is a way to quantify irradiation damage of a specific
 1301 particle at a specific energy. Via this factor different types of irradiation can be
 1302 compared. It is obtained experimentally by measuring the CCD of a number of
 1303 samples at various irradiation steps and fitting the equation 3.5 to the data. λ is the
 1304 measured CCD, λ_0 is the CCD of a non-irradiated sample and Φ the radiation dose.
 1305 As a reference, the damage factor for 24 GeV protons is set to $1 \times 10^{-18} \mu\text{m}^{-1} \text{ cm}^{-2}$.

$$\frac{1}{\lambda} = \frac{1}{\lambda_0} + k_\lambda \cdot \Phi \quad (3.4)$$

$$\lambda = \frac{\lambda_0}{k_\lambda \lambda_0 \Phi + 1} \quad (3.5)$$

1306 The data points with the maximum CCD obtained in the test beam measurements
 1307 are plotted against radiation dose received (see figure 3.7b). Equation 3.5 is fitted
 1308 to the data points and a damage factor $k_\lambda = (4.4 \pm 1.2) \times 10^{-18} \mu\text{m}^{-1} \text{ cm}^{-2}$ was
 1309 obtained. This value is for a factor of two higher than the damage factor obtained by
 1310 RD42. This could be due to an insufficient priming time ahead of the measurement.
 1311 In addition, the diamond samples have not been polished and re-metallised after
 1312 irradiation, as is the case for the RD42. Also, with only two samples measured, the
 1313 statistical uncertainty is high. Nevertheless, it can be concluded that the 300 MeV
 1314 pions damage the diamond bulk more than the 24 GeV protons.

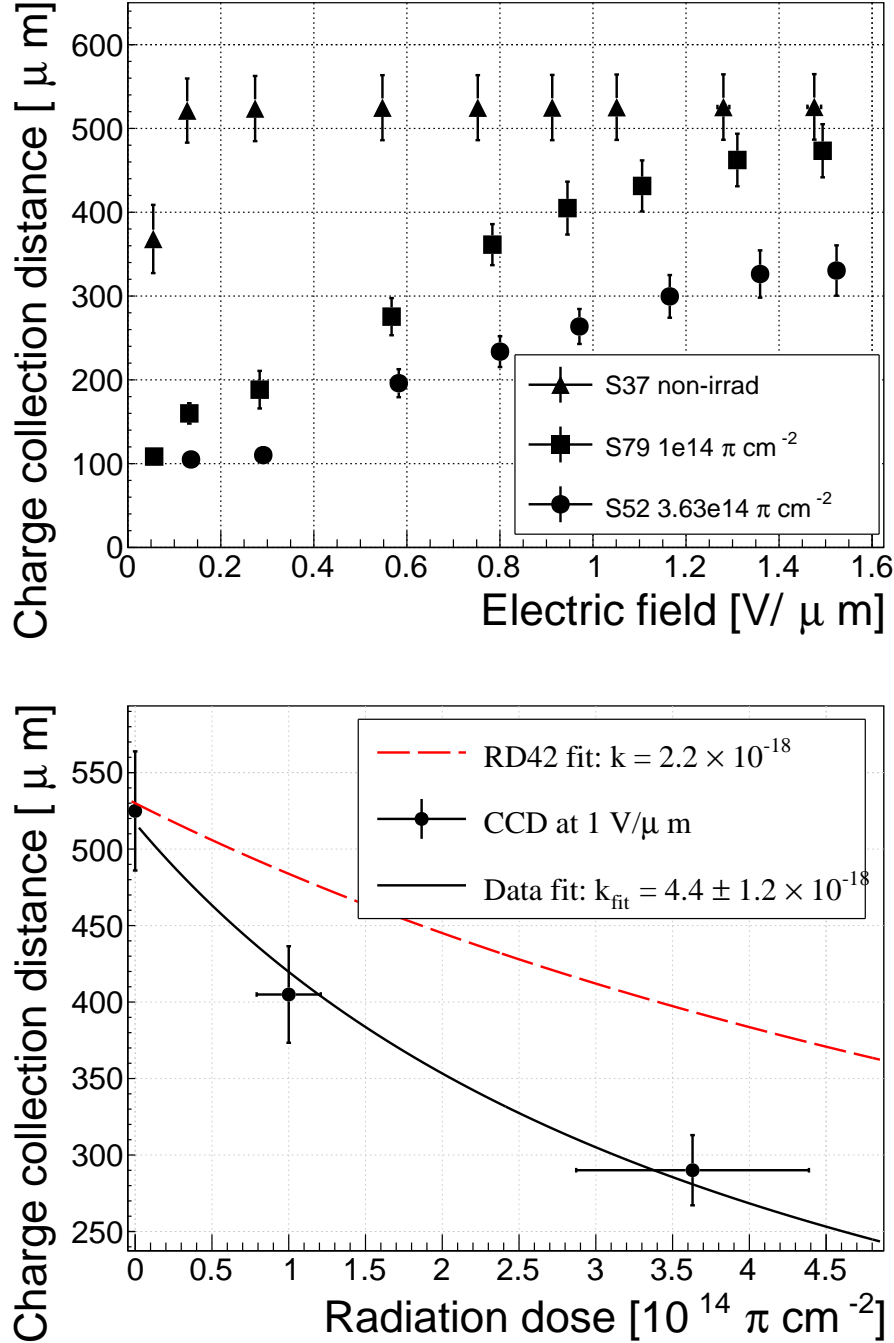


Figure 3.7: First figure shows the CCD for S37, S79 and S52 at a range of bias voltage settings. The charge collection distance at 1 V/μm bias voltage for the three diamond samples is then compared to the RD42 data for pion irradiation in the second figure. The data points are about 15–25 % lower than expected from the RD42 data [35].

¹³¹⁶ 3.3.2 Long-term measurement stability

¹³¹⁷ An important requirement for particle detectors is a stable performance over long
¹³¹⁸ periods of time. For instance, the charge collection for a defined radiation type and

3.3. RADIATION LIMITATIONS

1319 quantity must not change over time or has to change in a predicted way. Diamonds
1320 are stable as long as their environment and their operating point does not change
1321 significantly. The stability of diamond detectors depends on many factors (material
1322 purity, polishing process, electrode material, irradiation damage etc.). The aim is
1323 to study the behaviour of diamond under controlled conditions, with the goal to
1324 understand its limitations. One of these limitations is for sure the received radiation
1325 dose as it can affect the long-term stability of the sensor during operation.

1326 The three diamond samples (S37, S79 and S52) have been exposed to two different
1327 types of ionising radiation for a longer period to see if their behaviour changes over
1328 time. Two parameters have been observed in particular:

- 1329 1. Charge collection of β particles and
- 1330 2. Charge collection and ionisation profile of α particles.

1331 The results in this and in the next section will show that, in both cases, priming plays
1332 an important role in improving the diamond measurement stability.

1333 3.3.2.1 β long-term stability

1334 The diamond samples have undergone a long-term stability test using β radiation.
1335 This has been done using a ^{90}Sr source emitting ~ 2 MeV electrons at a rate of
1336 approximately $10^4 \text{ e}^- \text{ cm}^{-2}$. To simulate the initial conditions in HEP experiments,
1337 the sensors must not be primed before starting the measurements. The measurement
1338 setup consists of a diamond sample (S37, S52 or S79) with the Cx spectroscopic
1339 amplifier, a silicon diode with a C6 amplifier for a trigger and a ^{90}Sr source on
1340 top. A particle emitted by the source traverses the sensor bulk and hits the silicon
1341 diode, triggering the analogue signal readout. The source is left on the top for the
1342 course of the experiment. The measurements, however, are taken at discrete times.
1343 For every data point, approximately 10^4 triggers are recorded. The offline analysis
1344 of the recorded signal pulse amplitudes yields a landau distribution for every data
1345 point. The most probable value (MPV) of the distribution is proportional to the
1346 collected charge by the diamond sensor. The resulting graph of charge collection over
1347 time (see figure 3.8) shows that the charge collection efficiency improves when the
1348 diamond sensor is primed with a β source. This is especially evident in the case of
1349 the two irradiated samples. S79 achieves close to a full efficiency whereas S52 reaches
1350 about 50 %. Both increases are significant. At a received dose of approximately
1351 4×10^6 particles the signal stabilises. As expected, the signal of the non-irradiated
1352 S37 does not change with time – this pure sCVD diamond sample has the maximum
1353 collection distance from the start of the measurement.

1354 It should be noted that the ~ 2.28 MeV electrons emitted by this source are not
1355 MIPs; their charge deposition is higher than that of an electron MIP, according to the
1356 Bethe-Bloch distribution [16]. Nevertheless, for the purpose of these measurements
1357 this energy was adequate since only the relative change in charge collection was of
1358 our interest.

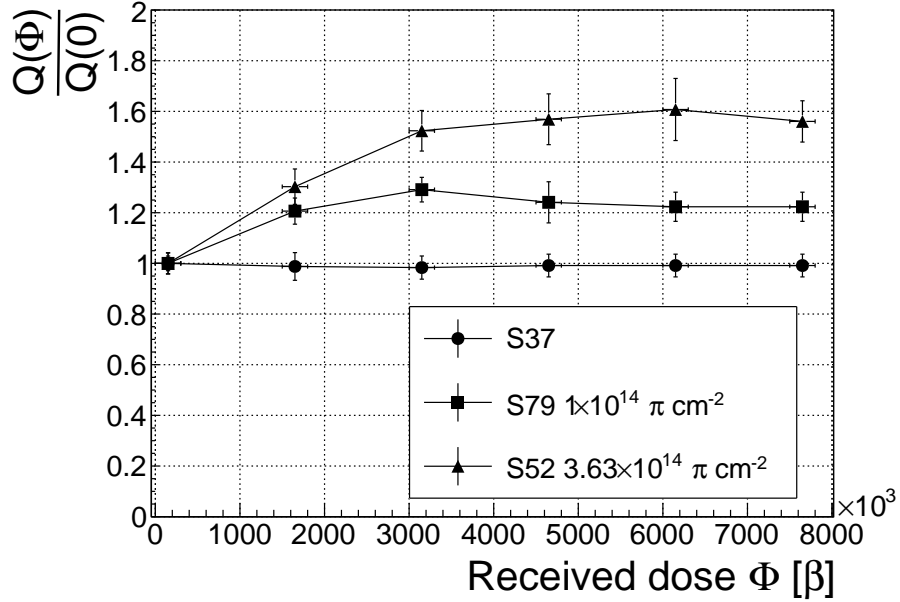


Figure 3.8: Relative increase of charge collection over time due to priming with the ${}^{90}\text{Sr}$ radioactive source. The bias voltage for this measurement is $1 \text{ V}/\mu\text{m}$.

To sum up, diamond is a good choice for β radiation detection. Even if damaged by radiation, it reaches a stable charge collection at a received dose of $\sim 4 \times 10^6$ MIP particles. The efficiency decreases with a high irradiation dose (effects visible above $10^{12} \text{ MIP cm}^{-2}$). However, the decrease can be accounted for if the damage factor and the rate and energy of the particles are known. γ radiation has a similar impact on the diamond as the β because the ionisation mechanism is the same. The incident photons, if they interact with the diamond, prime the bulk, causing the increase in charge collection efficiency. The difference, however, is that the interaction probability (cross section) is lower for gammas [41, 25].

3.3.2.2 α long-term stability

This part discusses the stability of irradiated diamond sensors during α measurements. An ${}^{241}\text{Am}$ source is used, emitting α particles with a mean energy of 5.5 MeV. It is safe to assume that they will behave differently than when subject to β radiation. This is due to the point-like charge carrier creation when an α particle penetrates the bulk and stops at a depth of $\sim 14 \mu\text{m}$ (for a 5.5 MeV particle). The deposited energy produces $\frac{5.5 \text{ MeV}}{13.6 \text{ eV}} = 4 \times 10^5$ e-h pairs. Compared to a MIP, which produces an MPV of $500 \mu\text{m} \times 36 \text{ e-h } \mu\text{m}^{-1} = 18 \times 10^3$ e-h pairs in a $500 \mu\text{m}$, the collected charge is for a factor of 22 higher. In addition, the energy is deposited in a small volume – $14 \mu\text{m}$ in depth and $\sim 20 \text{ nm}$ radially [28]. This dense distribution of charge carriers affects their behaviour at the start of the drift. Furthermore, carriers of only one polarity drift through the sensor while those of the opposite polarity almost instantly

3.3. RADIATION LIMITATIONS

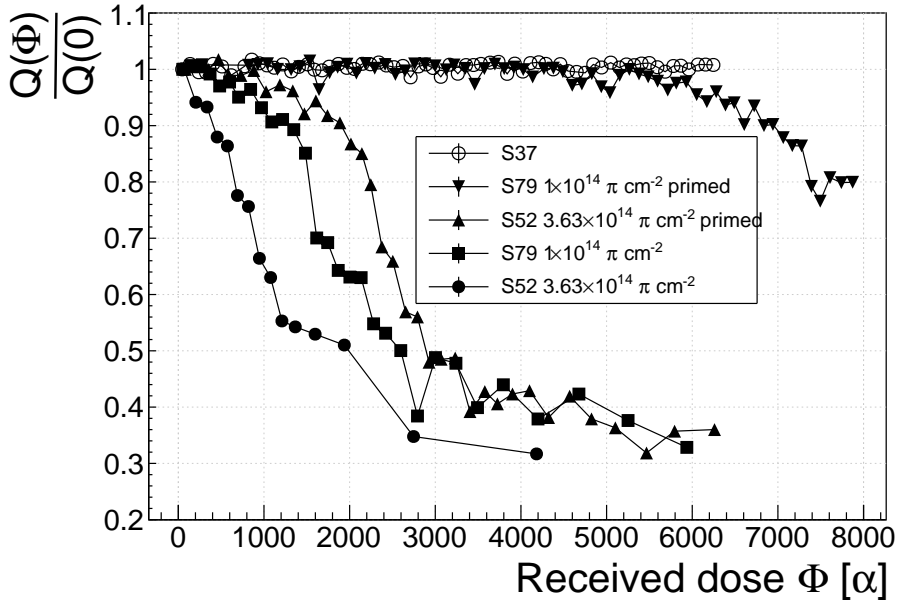


Figure 3.9: Relative decrease of collected charge with time for non-irradiated and irradiated diamond samples.

1380 recombine with the adjacent electrode. Taking into account that the diamond bulk
 1381 has been damaged by irradiation, these two phenomena might have an effect on the
 1382 operation of the detector on a macro scale.

1383 The first test has been carried out using the Cx spectroscopic amplifier, with
 1384 the bias voltage of the samples set to +500 V. Figure 3.9 shows the results of 6500
 1385 recorded hits at a rate of ~ 7 particles per second. The collected charge $Q(\Phi)$ for
 1386 the non-irradiated sample is stable as compared to the initial collected charge $Q(0)$
 1387 (plotted as a relative value $\frac{Q(\Phi)}{Q(0)}$). It is expected that the irradiated samples will have
 1388 a lower charge collection efficiency than the non-irradiated sample. However, their
 1389 initial efficiency suddenly drops after a certain period of time. The initial efficiency
 1390 after priming with β particles is higher than that without priming, but eventually it
 1391 deteriorates again. In addition, the spread of measured energies increases significantly.
 1392 Finally, the particle counting rate decreases with the decreased efficiency.

1393 To investigate this sudden drop in efficiency, the current pulse shapes using a
 1394 C2 current amplifier have to be observed (see figure 3.10). The shape of the pulse
 1395 holds more information about the charge carrier properties in the sensor than solely
 1396 the value of the integrated charge. This time only the primed S79 sample has been
 1397 tested. Both hole and electron collection are observed to determine whether they
 1398 behave differently or not. The sample has been measured long enough for the pulse
 1399 shapes to start changing. The data in figures 3.10 show that the initially stable pulses
 1400 start deteriorating – suddenly several different shapes start appearing, some still very
 1401 similar to those from the beginning while the others with almost zero amplitude.

1402 Some charges get stopped in the charge traps in the bulk for a long time, building

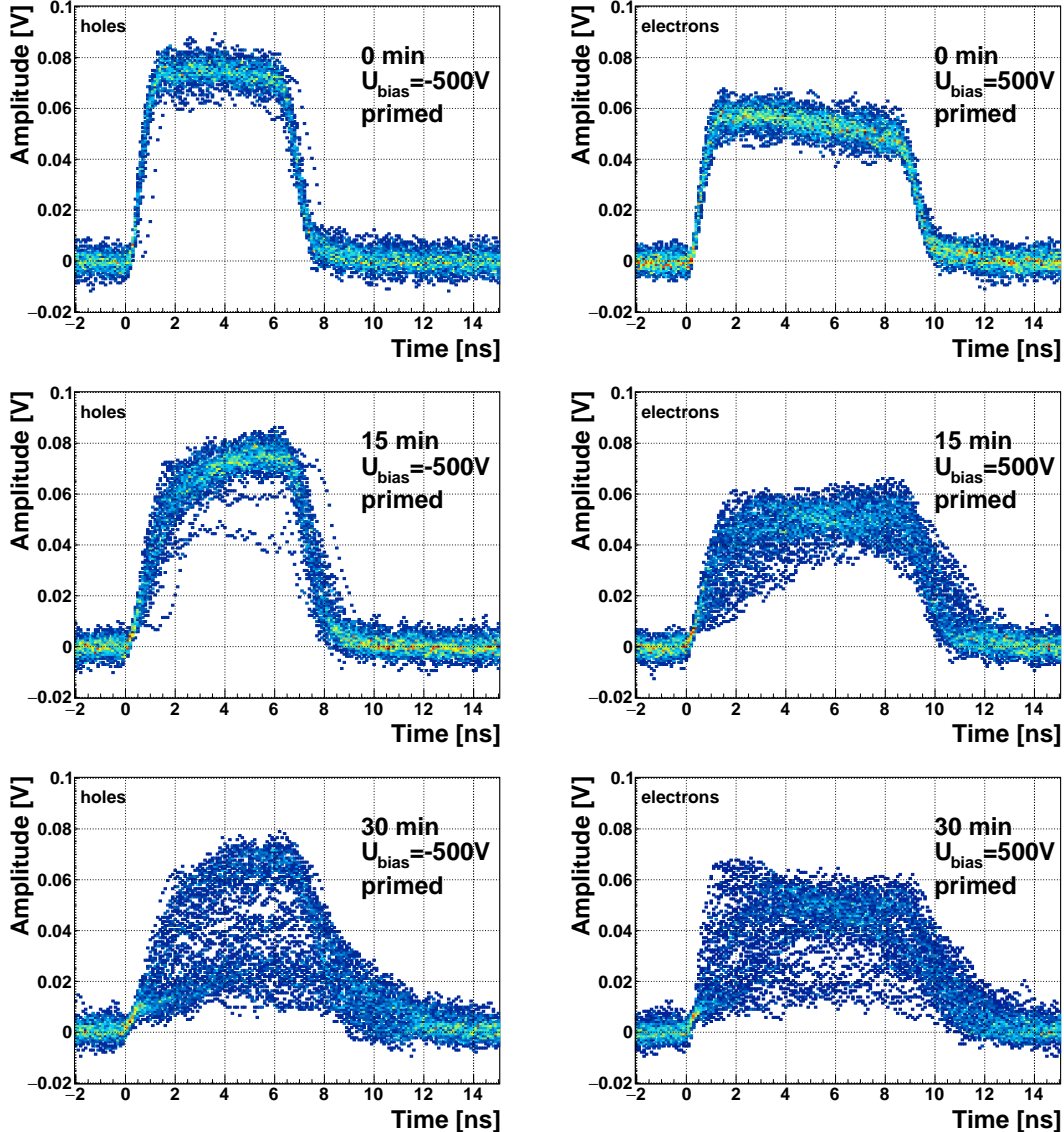


Figure 3.10: The signal of the irradiated and primed S79 deteriorates with time for both polarities. Every plot contains 60 superimposed pulses.

1403 up regions of space charge. The built up space charge affects the electric field, making
 1404 it non-uniform. The non-uniform field in turn affects the drifting carriers, slowing
 1405 them down or speeding them up, depending on the field gradient. Since the movement
 1406 of the carriers is inducing the electric current, the field gradient can be observed in
 1407 the signal.

1408 The second test with the C2 current amplifier has been carried out as follows: At
 1409 the beginning of the test when the diamond is still operating stably, 60 pulses are
 1410 recorded. An average pulse is calculated. This is a reference pulse for the subsequent
 1411 measurement points. Then an RMS of the single pulses with respect to the reference
 1412 pulse is calculated and the values are summed together (σ_{ref}).

3.3. RADIATION LIMITATIONS

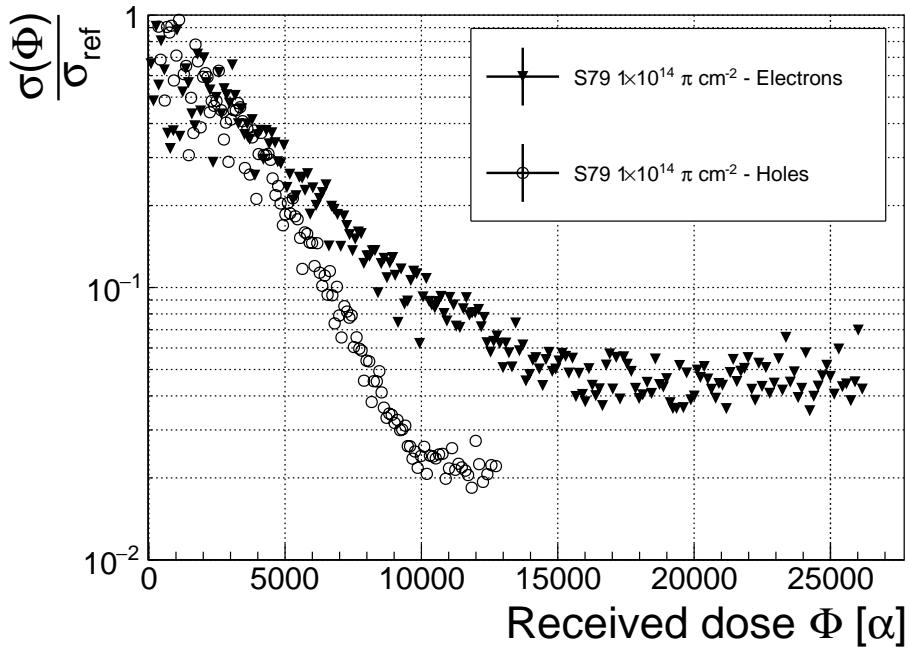


Figure 3.11: Deterioration of the pulse shapes with time

1413 All the subsequent data points also consist of a set of 60 pulses. At every data point
 1414 the summation of the RMS values of the individual pulses with respect to the initial
 1415 averaged pulse is calculated (σ). The ratio between the initial σ_{ref} and discrete values
 1416 σ gives a measure of change of the pulse shape with respect to the reference pulse at
 1417 the start of the measurement. Figure 3.11 shows the ratio $\frac{\sigma_{\text{ref}}}{\sigma(\alpha \text{ dose})}$. From the data
 1418 obtained it can be concluded that initial pulse shape quickly starts deteriorating. In
 1419 fact, the deterioration of the shape follows an approximate exponential decay function,
 1420 which can be fitted to the data. The resulting decay constants for electrons and holes
 1421 are $\tau_e = (4400 \pm 150) \alpha^{-1}$ and $\tau_h = (3300 \pm 140) \alpha^{-1}$. The electrons retain the initial
 1422 shape for longer. The deteriorated shapes also seem to be for a factor of 2 better
 1423 than those of the holes.

1424 Finally, an effort has been made to find a way for the pulse shapes to return to
 1425 their initial state. Five methods are listed:

- 1426 1. Removing the source and leaving the bias voltage switched on,
- 1427 2. Removing the source and switching the bias voltage off,
- 1428 3. Priming with γ at a rate of $400 \text{ s}^{-1} \text{cm}^{-1}$ without applied bias voltage,
- 1429 4. Priming with β at a rate of $1000 \text{ s}^{-1} \text{cm}^{-1}$ with applied bias voltage and
- 1430 5. Priming with β at a rate of $1000 \text{ s}^{-1} \text{cm}^{-1}$ without applied bias voltage.

1431 The diamond sample S79 is first primed using a ^{90}Sr source for about one hour.
 1432 Then the bias voltage is switched on and an ^{241}Am source is put on top. The pulses

produced by the incident α particles have a proper rectangular pulse at the beginning, but then start changing – first gradually and later increasingly more in an erratic way, as described in the text above. After approximately 30 minutes, one of the methods is tested. When a “healing” procedure is started, a set of 60 pulses is taken at irregular points of time to observe the change in the pulse shape and to assess the quality of the “healing” procedure. Then the bias voltage is switched off and the sample is primed again to reset its state before starting with the next run.

The results depicted in figure 3.12 show that the methods (3) and (5) improve the shape, method (2) helps slowly, (1) does not show any change with time and (4) at first improves, but then significantly degrades the shape. The effect observed in method (4) has already been described in [32]. The “healing” process therefore depends on the rate of radiation, the bias voltage and the time of exposure. The ionising radiation creates free charges, which quickly recombine close to the place of generation. It is likely that they also release the charges trapped during the measurement, reducing the overall effect of the space charge. The traps get filled with both flavours of carriers, thus they are neutralised. The pulse shape gradually returns to its initial state.

	Procedure	Source	Bias voltage	Effectiveness
1449	1	/	ON	no
	2	/	/	slow
	3	^{60}Co	/	YES
	4	^{90}Sr	ON	no
	5	^{90}Sr	/	YES

Table 3.2: Effectiveness of healing procedures

In summary, the shape of the pulses caused by α radiation changes with time for irradiated samples. The shape of the pulses gets distorted and becomes erratic. Charge collection decreases and its spread increases. This happens even faster for non-primed diamonds. To “heal” the diamond – to bring the pulse shapes back to their initial shape – the sample must be primed using a β or a γ source for several minutes at the bias voltage set to 0 V. Switching to the inverse polarity for a few seconds helps a bit, but in a long run distorts the signal, which cannot get back to its initial shape.

3.4 Temperature limitations

A test has been carried out to evaluate the effect of temperature changes on the output signal of the diamond sensors. A cryostat filled with liquid helium is used to cool down the sensor during the measurement process. The current signal response to α -particles is measured at 18 temperature points between 4 K and 295 K. At every temperature point, a set of 300 pulses is read out at various bias voltages. Resulting data show that the charge collection is stable down to 150 K, where it starts decreasing and stabilises again at about one third of the initial value at 75 K. This behaviour was first measured and discussed by H. Jansen [28].

3.4. TEMPERATURE LIMITATIONS

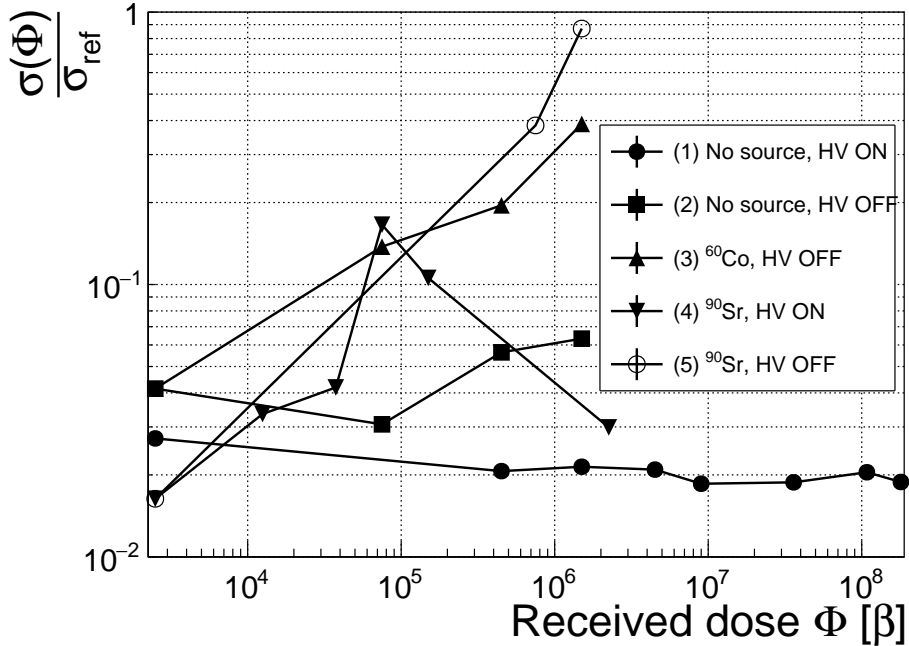


Figure 3.12: Five procedures for the “healing” process for an irradiated diamond that was exposed to α radiation at bias voltage switched on for at least 30 minutes at a rate of 10^4 s^{-1} .

The band gap energy in diamond is equal to $E_g = 5.5 \text{ eV}$ while the average energy to produce an electron-hole pair is $E_{e-h} = 13.25 \text{ eV}$. This means there is excessive energy deposited in the diamond bulk. The incident α -particle stops within $\sim 10\text{--}15 \mu\text{m}$ of the bulk, transferring all its energy to the lattice during deceleration. A part of this energy directly ionises the carbon atoms, creating free electron-hole pairs. The positively charged hole and the negatively charged electron in the hole attract each other via the Coulomb force and may undergo a bonding process during which a phonon is emitted.

The remaining energy, however, is converted into lattice vibrations (phonons [45, 28]). This means that the lattice within the ionisation volume (approximately $\sim 15 \mu\text{m} \times \sim 2 \text{ nm}$ in size) is briefly heated up. The hot plasma then cools down to the temperature of the surrounding material by heat dissipation, (i.e. phonon transport). The free electron binds the free hole into a bound state (not recombination) – the exciton [33]. The exciton binding energy is 80 meV. At higher temperatures, the lattice provides enough energy to excite the electron from the exciton state back to the conduction band. At lower temperatures, however, the exciton lifetime increases, which means that it will take a longer time for the electrons to get re-excited to the conduction band. The re-excitation lifetime at room temperature is $\sim 30 \text{ ps}$, increasing to $\sim 150 \mu\text{s}$ at 50 K [28]. This means that some of the bound electrons will not even start drifting within the period of $\sim 10 \text{ ns}$, which is the expected carrier drift time. When they are finally freed, the current they induce is already hidden in the electronics noise.

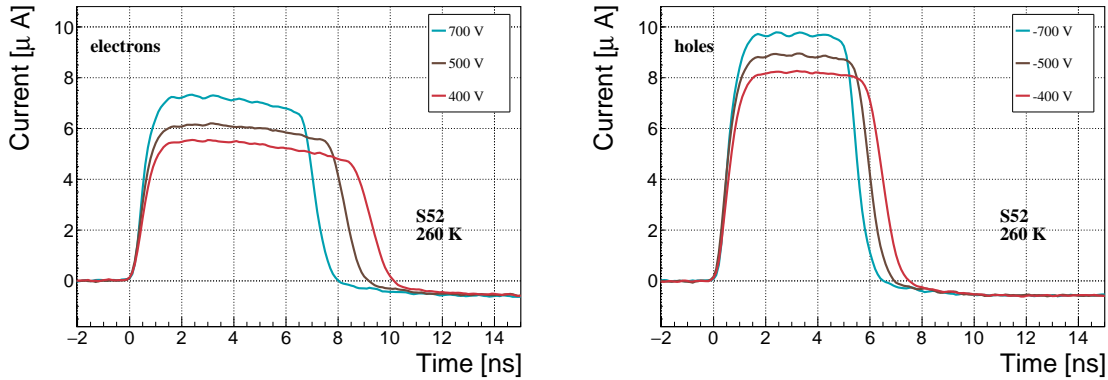


Figure 3.13: Varied bias voltage at a fixed temperature

1489 The effective area of the observed current pulse is therefore smaller than that of a
 1490 pulse induced by all the carriers drifting at the same time. This in effect reduces the
 1491 measured collected charge. The longer the time constant, the lower the measured
 1492 collected charge, as shown in figure 3.17 below.

1493 3.4.1 Temperature-variant α -TCT before irradiation

1494 Three sCVD diamond samples have been tested at a range of temperatures using
 1495 the α -TCT technique. At each temperature point, the bias voltage is set to several
 1496 positive and negative values. A set of 300 pulses is recorded at every data point
 1497 and averaged offline. The resulting averaged pulses of sample S37 at the 260 K
 1498 temperature point and a bias voltage of ± 400 V, ± 500 V and ± 700 V are shown in
 1499 figure 3.13. The pulses induced by holes as charge carriers are shorter than those
 1500 induced by electrons, which means that holes travel faster in diamond. The area of
 1501 the pulse, however, is the same for both polarities, which corresponds to the fact that
 1502 the same amount of charges is drifting in both cases.

1503 Figure 3.14 shows pulses at a bias voltage set to ± 500 V across the range of
 1504 temperatures between 4 K and 295 K – room temperature (RT). Several conclusions
 1505 can be drawn by observing their shape. First, the pulse shapes change with decreasing
 1506 temperature. The pulse time gets shorter, hinting at the faster carrier drift velocity
 1507 v_{drift} . Second, between 150 K and 75 K there is a significant change in shape - the
 1508 time constant of the rising edge increases significantly and the pulse area decreases.
 1509 From 75 K down to 4 K there is no significant observable change. Last, the top of
 1510 the pulse at the S52 is not flat, which means that a portion of the drifting charge is
 1511 lost along its way. This is due to charge trapping, likely by means of crystal defects
 1512 or impurities.

3.4. TEMPERATURE LIMITATIONS

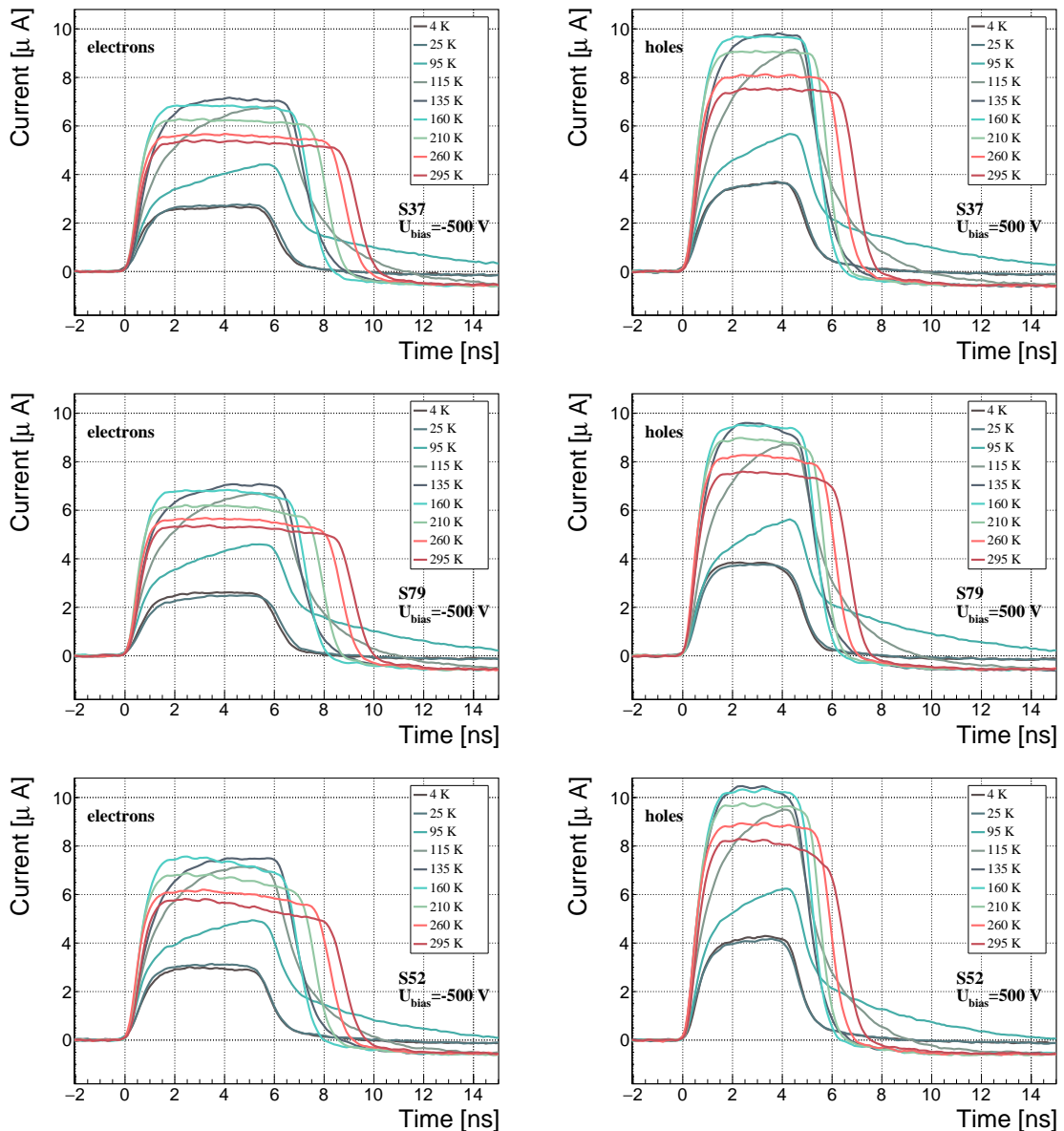


Figure 3.14: Several data points between 4 K and 295 K at a bias voltage of ± 500 V

3.4.2 Temperature-variant α -TCT after irradiation

The irradiated S79 and S52 have been re-tested in the cryostat after irradiation. The aim was to see how their pulse shapes change with decreasing temperature, in particular the decaying top of the pulses (see figure 3.15). The decay time gives information on trapping of charge carriers while travelling through the diamond bulk. A variation of the decay time constant as a function of temperature might help to reveal the type and depth of the charge traps. To observe these effects or lack thereof, a number of requirements has to be met. First, the diamond samples are intentionally not primed prior to the experiment because priming would improve the pulse shapes and possibly change the decay time constant of the signal. Second, keeping in mind that the pulse shape of irradiated diamonds changes with time, the duration of the measurement of an individual data point has to be short – of the order of 30 seconds. Last, the sequence of the bias voltage settings is important, the reason for which is explained below.

Unfortunately it is not possible to avoid temporal pulse changes. For instance, one measurement point takes approximately one minute. After the measurement, the bias voltage polarity is swapped for a few seconds to bring the diamond back into its initial state. But a few seconds with respect to a minute is not enough. Therefore, when the bias voltage is set to the next value, there is still some residual effect of the previous measurement. Similar to the effects of polarisation, this effect is also decreasing the pulse height. This can be observed in figure 3.15, which shows the resulting pulses of S52 for bias voltages of ± 200 V, ± 300 V, ± 400 V and ± 500 V at 230 K and 260 K. In this case the measurements sequence is: 230K (200 V, 300 V, 400 V, 500 V, -500 V, -400 V, -300 V), 260 K (-200 V, -300 V, -400 V, -500 V, 500 V, 400 V, 300 V). The changes in pulse shapes for holes at 230 K and 260 K cannot be attributed to the temperature change. Instead, the explanation could lie in diamond “polarisation”. This means that, when exposed to an electric field with α measurements ongoing, the diamond builds up an internal electric field of inverse polarity, which effectively reduces the overall electric field. This internal field does not dissipate when the external bias voltage is switched off. It can be said that the diamond becomes “polarised”. When switching the polarity of the external bias voltage, the internal and external electric field point in the same direction at the beginning, increasing the overall electric field and with it the pulse height. In figure 3.15, this happens when switching from 500 V (figure 3.15a) to -500 V (figure ??) at 230 K. The built up polarisation contributes to the pulse having a sharp rising edge and a high amplitude. This effect decays during the next two voltage points. There would be a handful of ways to avoid this polarisation effect in the data:

1. After every data point invert the bias voltage and leave it to return to a neutral state for the same amount of time,
2. Make a hysteresis of data points, going from minimum negative to maximum positive bias several times,

3.4. TEMPERATURE LIMITATIONS

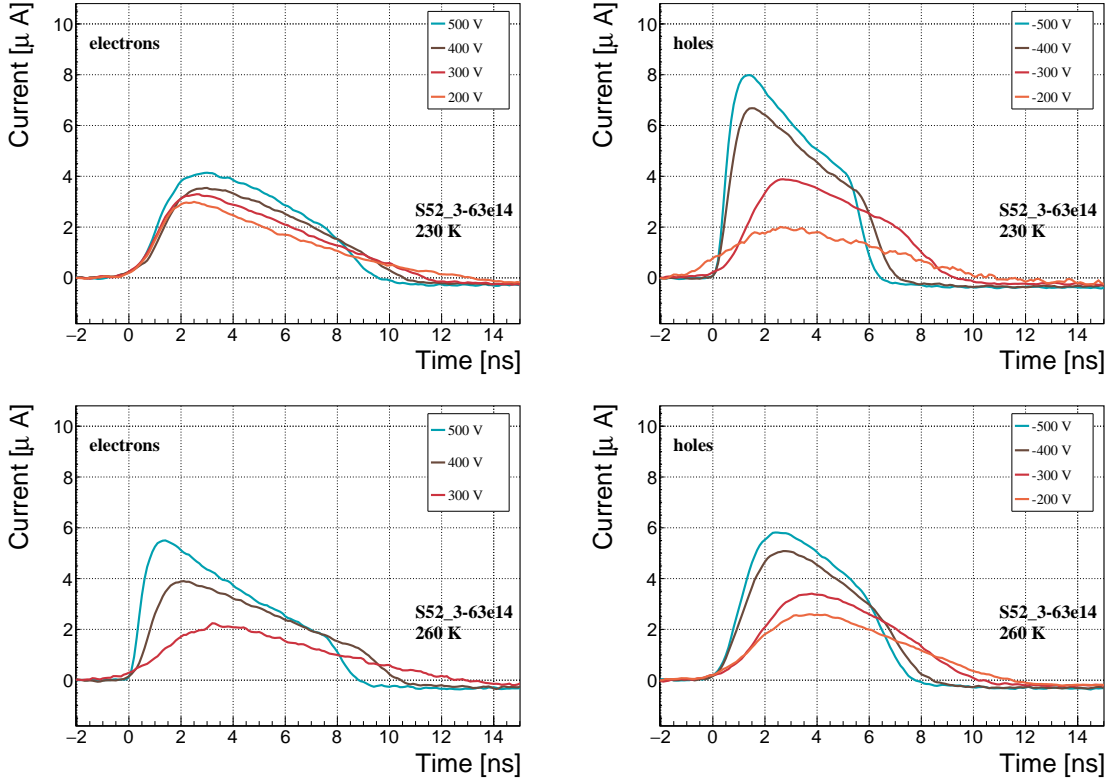


Figure 3.15: Varied bias voltage at a fixed temperature for an irradiated sample

1555 3. Reduce the measurement time at every bias voltage setting.

1556 Unfortunately, options (1) and (2) are very time consuming and would increase the
 1557 overall experiment time to over one day. The third option would worsen the resulting
 1558 averaged pulses. In the end an alternative option was chosen: alternating the start-
 1559 ing bias voltage and the sequence at every temperature point. With this option, a
 1560 meaningful systematic error in analysing the pulse shapes can be attained.

1561 Figure 3.16 shows the irradiated S52 and S79 as well as the non-irradiated S37
 1562 for comparison, all at a bias voltage of ± 500 V and at several temperature points
 1563 between 4 K and RT. It is evident that the radiation damage affected the shape of
 1564 the pulses across all temperatures.

1565 3.4.2.1 Collected charge as a function of temperature

1566 The area below the current pulse is proportional to the charge collected by the dia-
 1567 mond detector. The collected charge is observed as a function of temperature. First,
 1568 the amplitude values of the averaged pulses at a bias voltage of ± 500 V and across the
 1569 temperature range between 4 K and 295 K have to be integrated. Then a calibration
 1570 factor is used to derive the charge for all data points. This factor is obtained using
 1571 a Cx charge-sensitive amplifier. The resulting values for electrons and holes are plot-
 1572 ted in figures 3.17a and 3.17b, respectively. Thesis [28] gives a model that explains

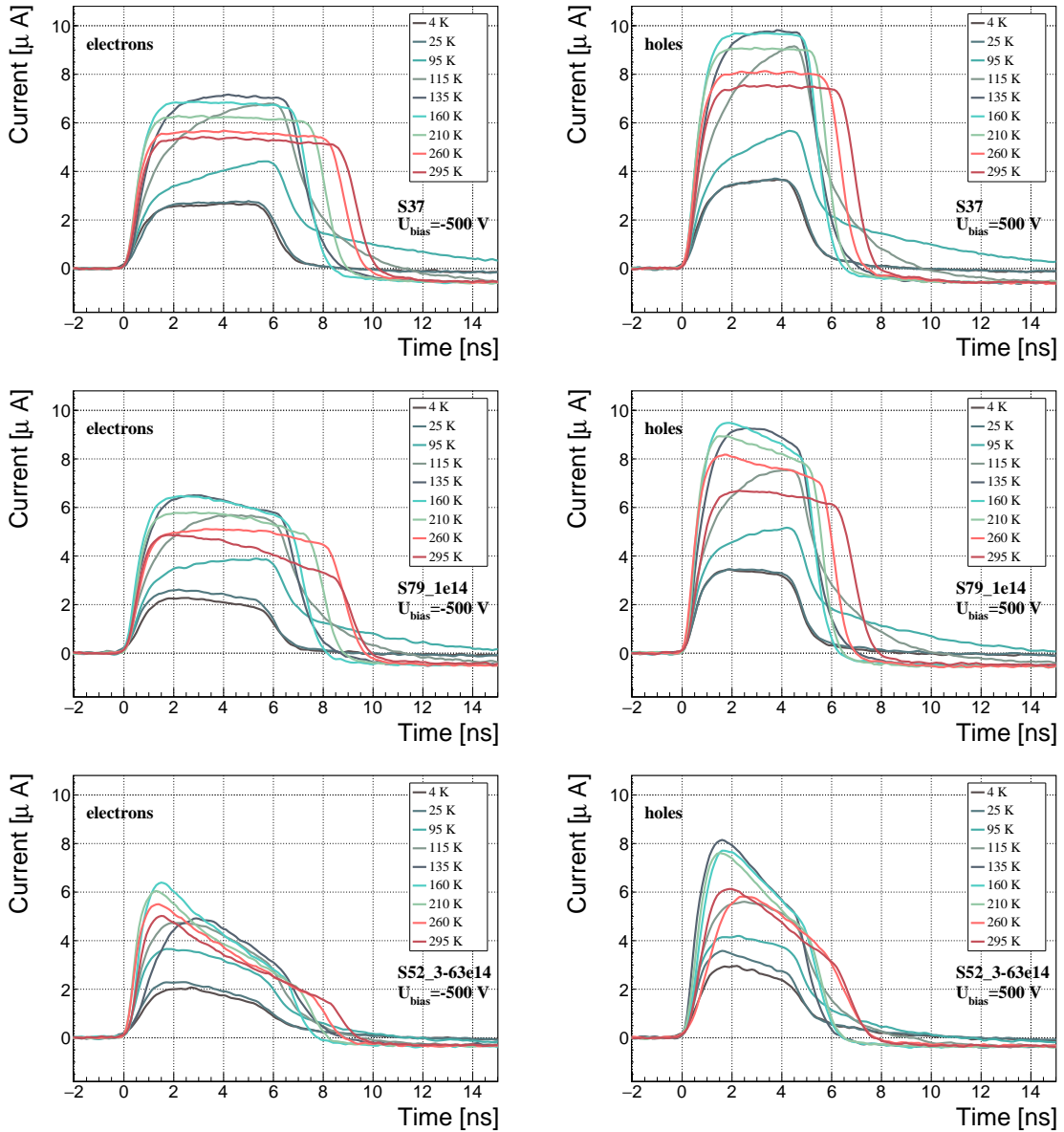


Figure 3.16: After irradiation: several data points between 4 K and 295 K at a bias voltage of ± 500 V

1573 the drop in charge below 150 K. The new contribution are the data points for the
 1574 irradiated samples. The values for them are lower than the those of non-irradiated
 1575 samples, which is expected.

1576 The values for all samples are fairly stable in the range between 4 K and 75 K
 1577 and between 150 K and 295 K. However, in the values for the irradiated S52 some
 1578 excursions can be observed. This is due to the sequence of the measurement steps,
 1579 which introduced a hysteresis effect and is explained in the preceding text.

1580 The collected charge drops significantly from 150 K down to 75 K. In the non-
 1581 irradiated samples the values in the lower temperature range are approximately 0.30

3.4. TEMPERATURE LIMITATIONS

of the values at the high range. For the irradiated ones this difference is lower – a factor of 0.35 for S79 and 0.5 for S52. An interesting detail is that the ratio between the values for non-irradiated samples and their irradiated counterparts at the lower range is different than at the higher range. Looking at the values for the electron collection in figure 3.17a: for S52 the lower ratio is equal to 1.28 and the higher equal to 1.7. For S79 these ratios are 1.00 and 1.09, which means that the difference in charge collection between 4 K and 75 K before and after irradiation is negligible.

3.4.2.2 Charge trapping

The carriers drifting through the bulk get stopped by the charge traps with a certain probability. This trapping happens uniformly throughout the diamond, decreasing the number of carriers in the charge cloud. Therefore the absolute number of trapped carriers decreases. At the same time the absolute number of trapped carriers per unit of length decreases. The resulting function for the number of drifting carriers per unit of length is a decaying exponential function:

$$I(t) = I(0) \cdot e^{-\frac{t-t_0}{\tau}} + I_0, \quad (3.6)$$

where $I(0)$ is the initial induced current, I_0 is the end current, t is time, t_0 is temporal displacement of the pulse and τ is the decay time constant. This value tells how long it takes before the amplitude of the pulse decreases to 63 % of its initial height.

The decaying exponential function has been fitted to the decaying top of the averaged pulses at bias voltages of ± 400 V and ± 500 V across all temperatures excluding the transitional range between 75 K and 150 K. The resulting decay time constants τ for an individual temperature point are not equal, which stems from the fact that the pulses change with time due to “polarisation”. This counts as a systematic error. Therefore the fitted τ for ± 400 V and ± 500 V are averaged into one value representing the measurement at that temperature point. Figure 3.18a shows the fitted τ for the five samples between 4 K and 295 K. In principle, the time constants should be infinite for a perfect and non-irradiated sample. Here a slightly tilted top of the pulse due to space charge is already successfully fitted with an exponential function, resulting in a τ of the order of (200 ± 20) ns⁻¹. Consequently the fitting method is not adequate for non-irradiated samples. For the irradiated samples, the fit becomes increasingly more meaningful. As seen in figure 3.18a, the fitted values of the irradiated samples are fairly stable across all temperatures. There is a slight increase in the decay time constant of the S52 from (6.0 ± 0.5) ns⁻¹ above 150 K to (8.5 ± 0.9) ns⁻¹ below 75 K. On the other hand, this step is not observable in the S79 data. With only one sample exhibiting this behaviour, the effect is not significant enough. Judging by the data acquired, the samples would need to be irradiated to doses above $1 \times 10^{14} \pi$ cm⁻² to quantify this effect in detail. So far this effect will not be regarded as significant for the scope of this thesis. Building on this assumption, the conclusion is that the signal decay time constant for irradiated sCVD diamond is constant across the temperature range between 4 K and 195 K, excluding the transitional range between 75 K and 150 K.

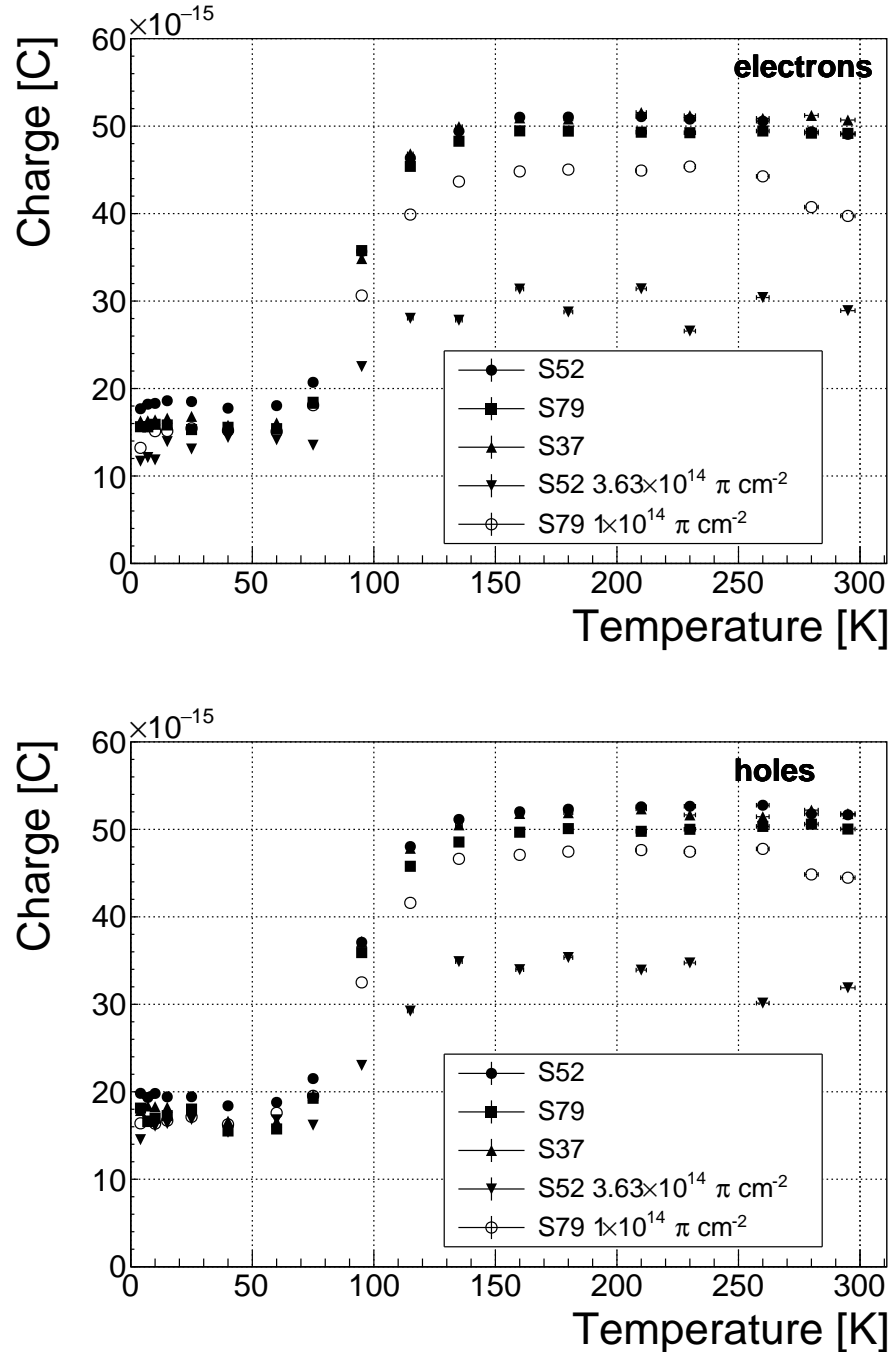


Figure 3.17: Collected charge as a function of temperature

1622 Taking into account the conclusions above, all the values can be averaged into one
 1623 decay constant. Figure 3.18b shows these values for all samples as a function of the
 1624 received $\pi_{300 \text{ MeV}}$ radiation dose. To estimate the carrier lifetime with respect to the
 1625 radiation dose received, a similar model is used than that in section 3.5. This model
 1626 states that the inverse of the carrier lifetime is linearly decreasing with increasing

3.4. TEMPERATURE LIMITATIONS

1627 radiation dose:

$$\frac{1}{\tau} = \frac{1}{\tau_0} + \kappa_\tau \cdot \Phi \quad (3.7)$$

1628

$$\tau = \frac{\tau_0}{\kappa_\tau \tau_0 \Phi + 1} \quad (3.8)$$

1629 where τ_0 is the lifetime for a non-irradiated sample (real lifetime, therefore of the order
1630 of 400 ns^{-1}), τ is the lifetime of an irradiated sample, Φ is the received radiation dose
1631 and κ_τ the lifetime degradation factor. For these data the fitted factor is equal to
1632 $\kappa_\tau = (3.6 \pm 0.8) \times 10^{-16} \text{ s cm}^2 \pi_{300 \text{ MeV}}^{-1}$. Using this factor, the steepness of the decay
1633 in the pulse shape with respect to radiation dose can be estimated. This can help
1634 when designing a system where current pulse shape is an important factor.

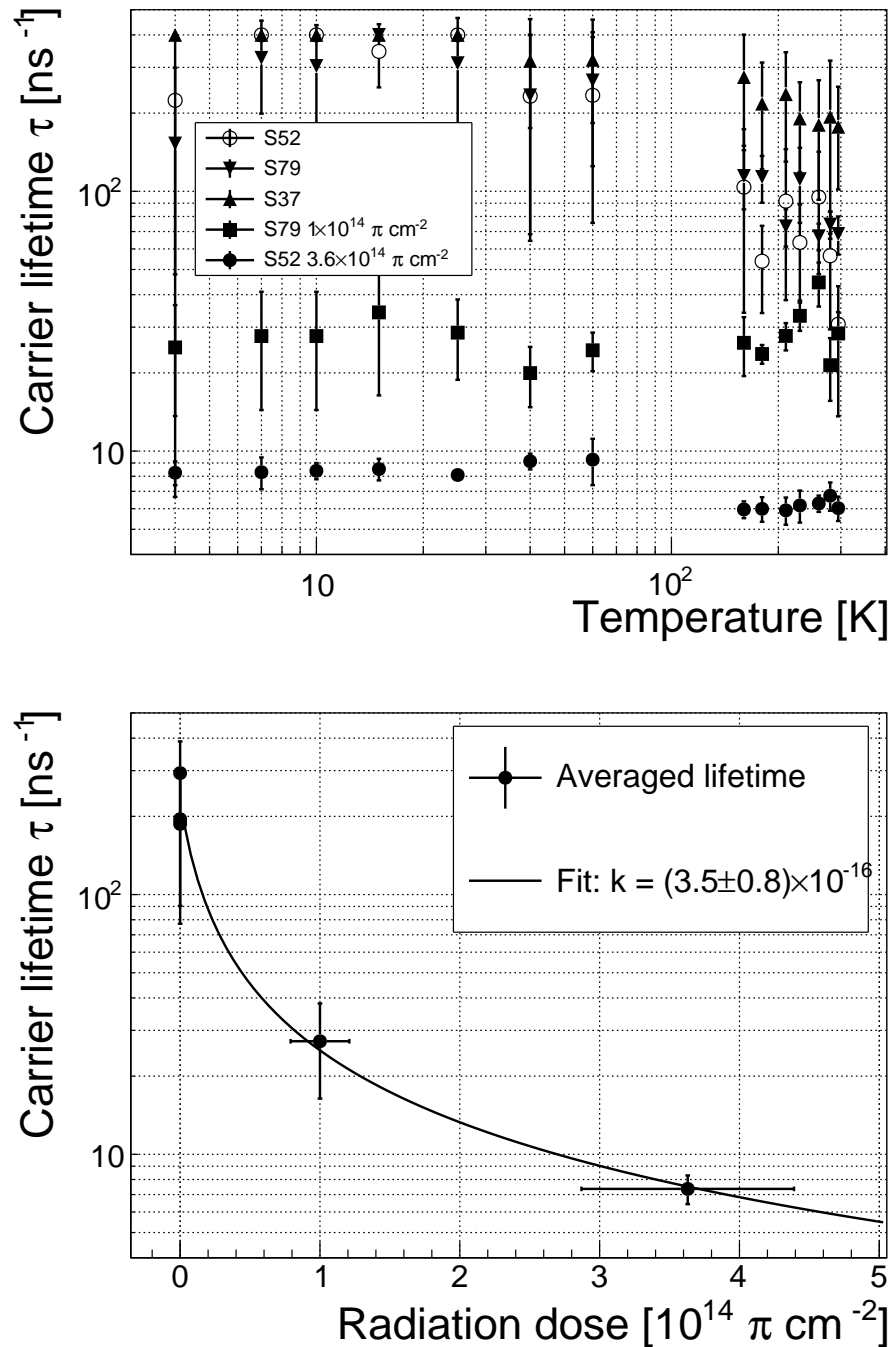


Figure 3.18: Charge carrier lifetime decreases with irradiation, but is stable across the range of temperatures between 4 K – 75 K and 150 K – 295 K. The first figure shows the carrier lifetime as a function of temperature whereas the second figure depicts the carrier lifetime averaged over all temperatures and plotted against the π irradiation dose

3.5. CONCLUSION

3.5 Conclusion

1636 This chapter gives an overview of the capabilities and limitations of diamond as
1637 a particle detector. Three effects on diamond were studied – noise, radiation and
1638 temperature, the focus being on the latter two.

1639 Two sCVD diamond detectors were irradiated with 300 MeV pions. They were
1640 tested alongside a non-irradiated sample to observe the changes in the ability to detect
1641 α , β and γ radiation. Their charge collection efficiency was measured in a test beam
1642 facility using . The results were compared to the results from the RD42 collaboration
1643 and a DPA model. A radiation damage factor $k_\lambda = (3.0 \pm 1.0) \times 10^{-18} \mu\text{m}^{-1} \text{cm}^{-2}$ was
1644 obtained for $\pi_{300 \text{ MeV}}$ particles. The data point was not in agreement with the data
1645 provided by RD42 nor with the model. However, the irradiation process and the low
1646 number of tested samples hold a relatively high statistical uncertainty. In addition,
1647 there was no diamond surface treatment done in between the measurements, as is the
1648 case in the study conducted by RD42. The results obtained in the course of these
1649 measurements will also be fed into the existing pool of data in the RD42 collaboration.

1650 The next step was to test the long-term capabilities for α detection. The shape
1651 of the ionisation profile was investigated to determine the behaviour of the charge
1652 carriers in the irradiated diamond. An exponential decay was observed in the pulses
1653 of irradiated samples, proving that there are charge traps in the bulk that were created
1654 during irradiation. Then a long-term stability test was carried out. The results show
1655 that the irradiated diamond detectors do not provide a stable and reliable long-term
1656 measurement of α particles. This might be due to a space-charge build-up in the
1657 bulk, which changes the electric field, affecting the charge carriers. A procedure to
1658 improve the pulse shape using β and γ radiation was proposed.

1659 Finally, the diamond sensors were cooled down to temperatures between 4 K and
1660 295 K. Their response to α particles was observed. The results of the non-irradiated
1661 and irradiated samples were compared. The effect of reduction for the number of
1662 drifting charges due to exciton recombination was observed in both sets of data.
1663 The second set had a superimposed effect of charge trapping during the drift, which
1664 was represented by an exponential decay in the signal. The decay time constant
1665 did not change with temperature. Therefore all temperature points for individual
1666 samples were averaged and the decay time constants were plotted against the received
1667 radiation dose. A damage factor equal to $\kappa_\tau = (3.5 \pm 0.8) \times 10^{-16} \text{ s cm}^2 \pi_{300 \text{ MeV}}^{-1}$ for
1668 non-primed diamonds was defined.

1669

Chapter 4

1670

Charge monitoring

1671

The ATLAS Diamond Beam Monitor

1672 Particle detectors in high energy physics experiments need to meet very stringent
1673 specifications, depending on the functionality and their position in the experiment.
1674 In particular, the detectors close to the collision point are subject to high levels of
1675 radiation. Then, they need to operate with a high spatial and temporal segmentation
1676 to be able to precisely measure trajectories of hundreds of particles in very short
1677 time. In addition, they need to be highly efficient. In terms of the structure, their
1678 active sensing material has to be thin so as not to cause the particles to scatter
1679 or get stopped, which would worsen the measurements. This also means that they
1680 have to have a low heat dissipation so that the cooling system dimensions can be
1681 minimised. Finally, they need to be able to operate stably for several years without
1682 an intervention, because they are buried deep under tonnes of material and electronics.

1683 The material of choice for the inner detector layers in the HEP experiments is
1684 silicon. It can withstand relatively high doses of radiation, it is highly efficient (of the
1685 order of $\sim 99.9\%$) and relatively low cost due to using existing industrial processes
1686 for its production. Its downside is that, with increasing irradiation levels, it needs to
1687 be cooled to increasingly low temperatures to ensure a stable operation. This is not
1688 the case with diamond. In addition, diamond has a lower radiation damage factor,
1689 which means it can operate in a radiation-heavy environment for a longer period.

1690 The ATLAS Diamond Beam Monitor (DBM) [] is a novel high energy charged
1691 particle detector. Its function is to measure luminosity and beam background in the
1692 ATLAS experiment. Given its position in a region with a high radiation dose, di-
1693 amond was chosen as the sensing material. The monitor's pCVD diamond sensors
1694 are instrumented with pixellated FE-I4 front-end chips. The pCVD diamond sensor
1695 material was chosen to ensure the durability of the sensors in a radiation-hard envi-
1696 ronment and the size of its active area. The DBM is not the first diamond detector
1697 used in HEP, but it is the largest pixellated detector installed so far (see figure 4.1).
1698 It was designed as an upgrade to the existing luminosity monitor called the Beam
1699 Conditions Monitor (BCM) [] consisting of eight diamond pad detectors, which is

4.1. LUMINOSITY MEASUREMENTS

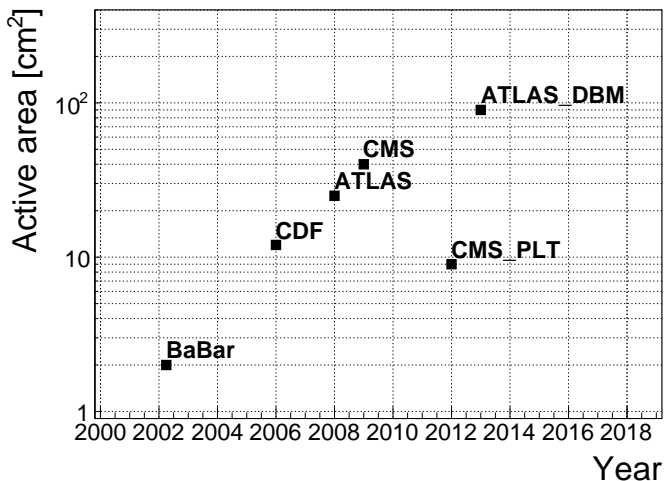


Figure 4.1: Diamond detectors installed in high-energy physics experiments in the last decade, sorted by the active sensor area. The first four detectors from the left are radiation monitors whereas the right two are pixel trackers.

able to perform precise time-of-flight (ToF) measurements. The DBM complements the BCM's features by implementing tracking capability. Its pixelated front-end electronics significantly increase the spatial resolution of the system. Furthermore, the DBM is able to distinguish particle tracks originating in the collision region from the background hits. This capability is a result of its projective geometry pointing towards the interaction region. This chapter first describes the principles of luminosity measurements. It then explains how the DBM will carry out this task. Finally, some results from tests and from the real collisions are presented.

When a particle traverses a sensor plane, a hit is recorded in the corresponding pixel. Thus, a precise spatial and timing information of the hit is extracted. With three or more sensors stacked one behind the other, it is also possible to define the particle's trajectory. This is the case with the DBM. Its projective geometry allows the particles to be tracked if they traverse the sensor planes. The DBM relates the luminosity to the number of particle tracks that originate from the collision region of the ATLAS experiment. Particles that hit the DBM from other directions are rejected as background radiation.

4.1 Luminosity measurements

Luminosity is one of the most important parameters of a particle collider. It is a measurement of the rate of particle collisions that are produced by two particle beams. It can be described as a function of beam parameters, such as: the number of colliding bunch pairs, the revolution frequency, the number of particles in each bunch and the transverse bunch dimensions. The first four parameters are well defined. However, the transverse bunch dimensions have to be determined experimentally

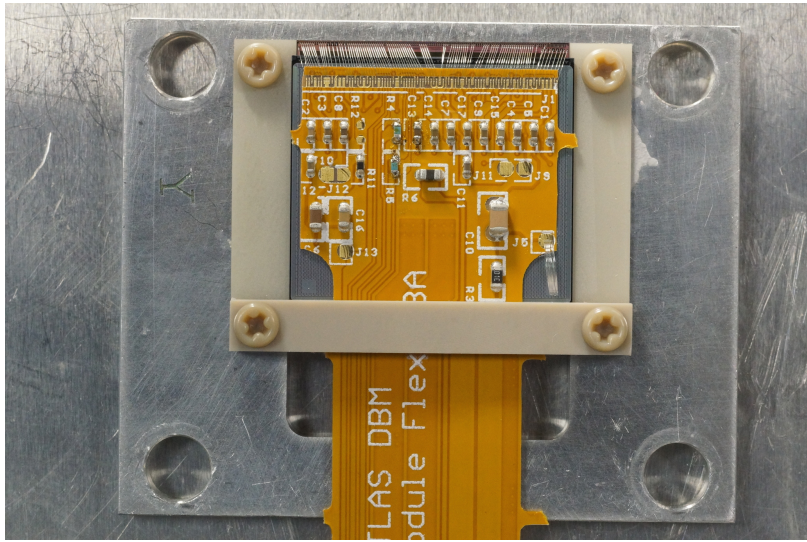


Figure 4.2: DBM module, top-down view. Visible is the flexible PCB with signal and power connections, the silicon sensor and a part of the FE-I4. Wire bonds from the PCB to the FE-I4 and to the sensor are also visible.

1723 during calibration. The ATLAS experiment uses the *van der Meer scan* [] during
1724 low-luminosity runs to calibrate the luminosity detectors. This scan is performed
1725 by displacing one beam in a given direction and measuring the rate of interactions
1726 as a function of the displacement. Transverse charge density of the bunches can be
1727 estimated on the basis of the interaction rate. The calibrated luminosity detectors
1728 can then operate during high-luminosity runs.

1729 One approach to luminosity monitoring is to count the number of particles pro-
1730 duced by the collisions. The luminosity is then proportional to the number of detected
1731 particles. A detector has to be capable of distinguishing individual particles that fly
1732 from the interaction point through the active sensor area. If the detector has at least
1733 three layers, it can reconstruct the particles' tracks, which in turn yields more infor-
1734 mation on the their trajectory. This is one reason why detectors with a high timing-
1735 and spatial segmentation are more suitable for these applications. The second reason
1736 is that, with a high spatial segmentation, the detector will not saturate even at high
1737 particle fluencies.

1738 4.2 Diamond pixel module

1739 The two most important parts of the diamond pixel module (seen in figure 4.2) are
1740 the sensor, which detects ionising radiation, and the pixellated front-end chip, which
1741 collects the ionised charge with a high spatial segmentation, processes the recorded
1742 data and sends them to the readout system. This section describes these two main
1743 parts of the module and their interconnection.

4.2. DIAMOND PIXEL MODULE

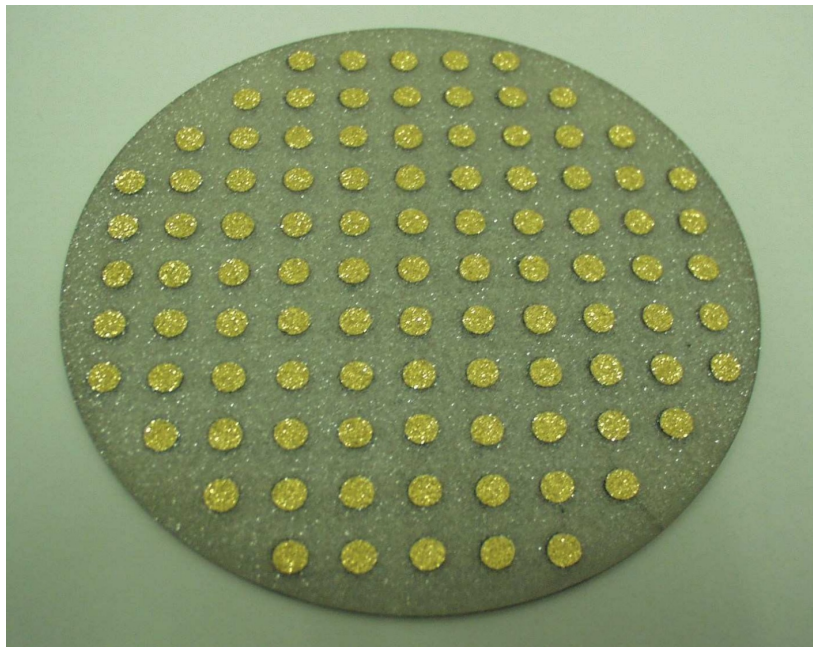


Figure 4.3: A pCVD wafer. The golden dots on the surface are the electrodes that are applied during the qualification test. The wafer is measured across the surface to find the regions with the highest efficiency.

¹⁷⁴⁴ 4.2.1 Sensors

¹⁷⁴⁵ The DBM modules are instrumented with two types of sensors – pCVD diamond and
¹⁷⁴⁶ silicon. The silicon sensors are used as a fallback solution because there were simply
¹⁷⁴⁷ not enough high-quality diamond sensors available. In addition, a comparative study
¹⁷⁴⁸ of irradiation damage between silicon and diamond can be made with such a hybrid
¹⁷⁴⁹ system.

¹⁷⁵⁰ **Diamond sensors** The target material for this application is pVCD diamond. The
¹⁷⁵¹ reason for this is that the active area of an individual sensor must be approximately
¹⁷⁵² 4 cm², which is too large for the sCVD diamond. pCVD material is also a bit
¹⁷⁵³ cheaper, which makes a detector with a large active area more feasible to build. The
¹⁷⁵⁴ material is provided by three companies: DDL, E6 and II-IV and it is grown in
¹⁷⁵⁵ 15 cm wafers, as seen in figure 4.3. The target thickness of the wafers is 500 µm and
¹⁷⁵⁶ the minimum required charge collection efficiency is 40 % (CCD \geq 200 µm). They
¹⁷⁵⁷ need to be operated at bias voltages between 600–1000 V. On one side there is a
¹⁷⁵⁸ single gold electrode applied across the whole surface. On the other side a pixellated
¹⁷⁵⁹ metallisation is added.

¹⁷⁶⁰ **Silicon sensors** are standard $n^+ - in - n$ planar sensors with a 200 µm thickness
¹⁷⁶¹ and were mostly fabricated at CiS [], a company from Ertfurt, Germany. They are
¹⁷⁶² designed to have nearly a 100 % efficiency when non-irradiated. Their bulk resistivity
¹⁷⁶³ is between 2–5 kΩcm and they were diffusion oxygenated at 1150 °C for 24 hours to

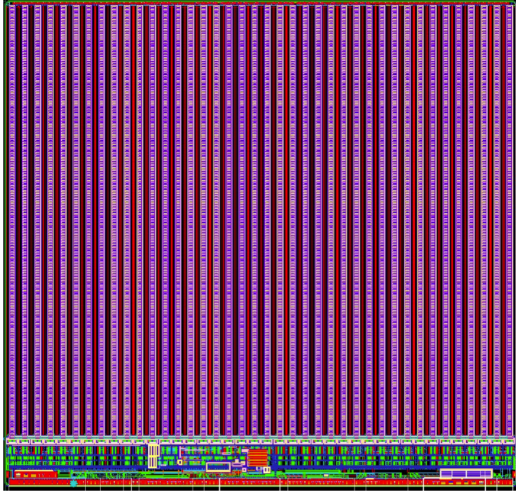


Figure 4.4: FE-I4 layout, top-down view. The pink area are pixels grouped into columns, the green area below is the common logic and the red strip at the bottom are the wire bond pads.

1764 increase their radiation hardness. One side is segmented into pixels. Guard rings at
1765 the edges of the sensor provide a controlled drop in potential, reducing the possibility
1766 of shorts at maximum design bias voltages of the order of 1000 V.

1767 4.2.2 Front-end electronics

1768 The FE-I4 (front-end version four) [] is an ASIC pixel chip designed specifically for
1769 the ATLAS pixel detector upgrade. It is built as a successor to the current pixel chip
1770 FE-I3, surpassing it in size of the active area ($4\times$ larger) as well as the number of
1771 channels/pixels ($10\times$ more). 336 such FE-I4 modules are used in the newly installed
1772 pixel layer called the Insertable B-Layer (IBL) []. The DBM is also instrumented
1773 with these chips. The FE-I4's integrated circuit contains readout circuitry for 26880
1774 pixels arranged in 80 columns on a $250\text{ }\mu\text{m}$ pitch and 336 rows on a $50\text{ }\mu\text{m}$ pitch. The
1775 size of the active area is therefore $20.0\times16.8\text{ mm}^2$. This fine granularity allows for a
1776 high-precision particle tracking. The chip operates at 40 MHz with a 25 ns acquisition
1777 window, which corresponds to the spacing of the particle bunches in the LHC. It is
1778 hence able to correlate hits/tracks to their corresponding bunch. Furthermore, each
1779 pixel is capable of measuring the deposited charge of a detected particle by using
1780 the Time-over-Threshold (ToT) method. Finally, the FEI4 has been designed to
1781 withstand a radiation dose up to 300 MGy. This ensures a longterm stability in the
1782 radiation hard forward region of the ATLAS experiment.

1783 Each pixel is designed as a separate entity. Its electrical chain is shown in figure
1784 4.5. The bump-bond pad – the connection to the outside of the chip – is the
1785 input of the electrical chain, connected to a free-running amplification stage with ad-
1786 justable shaping using a 4-bit register at the feedback branch. The analog amplifier is
1787 designed to collect negative charge, therefore electrons. The output is routed through

4.2. DIAMOND PIXEL MODULE

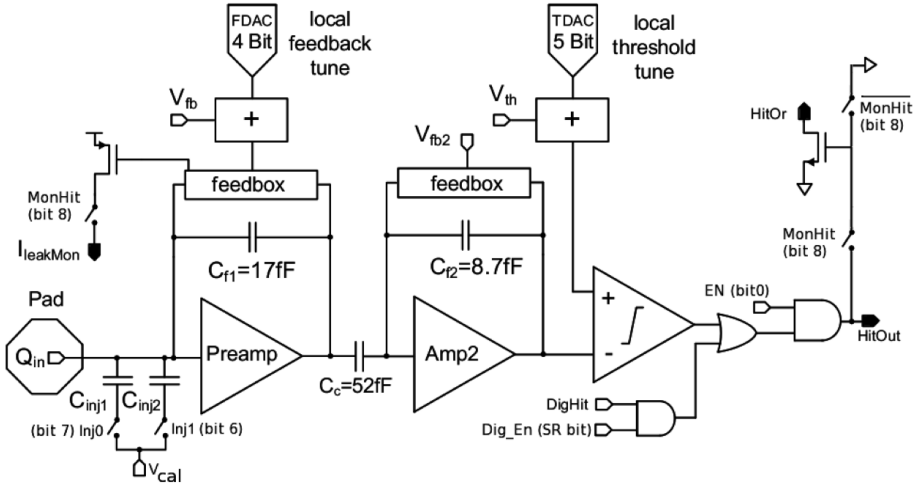


Figure 4.5: Schematic of an analog pixel. Courtesy of the FE-I4 collaboration.

1788 a discriminator with an adjustable threshold. This value in effect defines the level at
 1789 which the circuit will detect a hit. In addition, there is a counter of the clock cycles
 1790 (25 ns sampling) during which the signal is above the discriminator threshold. The
 1791 value of the counter is proportional to the collected charge. The logic gates at the end
 1792 of the chain are used to enable/disable the pixel and to issue a so-called HitOr flag –
 1793 this signal is set whenever at least one of the pixels was hit and is used as a trigger
 1794 for the readout. The output of the chain – HitOut – is routed into the logic of the
 1795 chip where it is buffered and eventually sent out to the readout system. The module
 1796 receives all its commands from the system via a 40 MHz LVDS line. The commands
 1797 are either settings for the pixel registers or triggers that start the data readout. The
 1798 data are sent via an LVDS line at up to 320 Mbit/s, but by default at 160 Mbit/s,
 1799 four times faster than the clock of the device. This allows the chip to clear out its
 1800 buffers before new data are recorded, thus avoiding dead time and data pile-up. The
 1801 FE-I4 has been successfully tested for trigger rates of up to 300 kHz.

1802 The DBM uses pCVD diamond with $d_C = 500 \mu\text{m}$ thickness and silicon with
 1803 $d_{Si} = 200 \mu\text{m}$ thickness as a sensor material. The resulting most probable value
 1804 (MPV) of the deposited charge for a minimum ionising particle (MIP) is calculated
 1805 with the formula $Q_s = d \cdot E_{e-h}$ and equals 18000 electrons and 17800 electrons,
 1806 respectively, at a full charge collection efficiency. Unfortunately this is not the case
 1807 with the pCVD material, whereby the expected charge collection efficiency is of the
 1808 order of 50 % – around 9000 e. This value further decreases with received irradiation
 1809 dose. Therefore in order to detect the particles depositing energy on the far left side
 1810 of the landau spectrum, the threshold has to be set to a significantly lower value.
 1811 On the other hand, if the threshold set too low, it also detects the electronic noise
 1812 and stores a false noisy hit. With the typical noise amplitudes being in the range of
 1813 120–200 e, a safe threshold range would be between $Th = 1000\text{--}3000$ e. The target
 1814 for the DBM is to lower the threshold down to 800 e.

The analog amplifier is implemented in two stages to get a fast rise time at a low noise and a low power consumption. The output signal of the analog amplifier has a triangular shape with a fast rise time and a long decay. The shape can be adjusted by tuning the amplifier feedback loop. Its length is proportional to the collected charge, but it needs to be calibrated first. This is done by means of two injection capacitors, $C_{\text{inj}1}$ and $C_{\text{inj}2}$, seen in figure 4.5 with well defined capacitances. First, the charge $Q_{\text{cal}} = V_{\text{cal}} \cdot (C_{\text{inj}1} + C_{\text{inj}2})$ is injected into the analog chain. Then the length of the output pulse is measured and finally the feedback value is changed to either lengthen or shorten the pulse in order to get to the required duration t_{cal} . The typical values are $Q_{\text{cal}} = 5000 - 16000$ e at the time $t_{\text{cal}} = 5 - 10$ ToT. The target values depend on the sensor, the type of a radioactive source and the application. Therefore the initial threshold Th at 1 ToT and the calibrated value Q_{cal} at t_{cal} ToT give us a linear scale of collected charge with respect to time over threshold. However, in practice this relation is nonlinear for lower thresholds, but since the goal of the measurements is to track the particles rather than to measure their deposited energy precisely, this is sufficient.

4.3 Module assembly and quality control

Parts for the detector arrived separately and were assembled into modules at CERN’s DSF lab after being checked for production faults. The assembled modules underwent a series of quality control (QC) and burn-in tests to determine their quality, efficiency and long-term stability.

4.3.1 Assembly

A single-chip module consists of a pixel module, a flexible PCB and the supporting mechanics (a ceramic plate and an aluminium plate). The chip arrives already bump-bonded to the sensor, be it diamond or silicon. First it is glued to the ceramic plate on one side and to the PCB on the other using either Araldite 2011 or Staystik 672/472. The choice of glue was a topic of a lengthy discussion. Staystik is re-workable and has a very high thermal conductivity. The latter is important because the FE-I4 chips tend to heat up significantly and need a good heat sink. The problem is that it has a curing temperature of 160/170 °C. This temperature may cause some unwanted stress build-up between the FE-I4 and the diamond sensor due to different coefficients of thermal expansion, pulling them apart. This would disconnect the pixels, yielding large regions of the module insensitive to radiation. To avoid this, an alternative glue was tried. Araldite 2011 can be cured at lower temperatures – down to RT – but it has a lower heat conductivity. In the end Araldite is used as the safer option. However, due to the longer curing, the whole assembly process using Araldite is extended to two working days. After curing, the module is wire-bonded and attached to the aluminium plate using screws made up of a radiation-resistant PEEK plastic. They have to be tightened with a great care, because their screw head is only 0.2–0.6 mm

4.3. MODULE ASSEMBLY AND QUALITY CONTROL

away from the sensor edge – the sensor displacement tolerance during gluing is of the order of 0.5 mm. Finally, the module is put in an aluminium carrier which protects it from mechanical damage or electrostatic discharges.

4.3.2 Testing

The modules are tested in the lab using an RCE readout system and a moving stage with two degrees of freedom. They are placed onto the stage and connected to the readout system and the power supplies. After ensuring the low- and high voltage connectivity they are checked for the signal connectivity. If everything is operational, a series of automated tests is run. Each of these tests calibrates a certain value within a pixel, whether it is the signal threshold or the value for integrated charge. These are tuned in a way that the response to a predefined calibration signal is uniform for all pixels across the sensor. This procedure is referred to as *tuning*.

When the modules are tuned, they are tested using a ^{90}Sr radioactive source. Two things are checked: 1) operation of all pixels and 2) sensor efficiency. The first test is carried out by moving the module slowly under the source while taking data so that the whole surface is scanned uniformly. The resulting occupancy map reveals any pixels that are not electrically coupled to the sensor via bump bonds. This is an important step in the DBM QC procedure, because it turned out that a significant portion of the flip-chipped diamond sensors exhibited very poor connectivity. The disconnected regions on the faulty modules ranged anywhere from 0.5–80 % of the overall active surface. In two cases the sensor was even completely detached from the chip. Therefore the pixel connectivity turns out to be the most important qualification factor in the QC procedure. Unfortunately the only way to check it at the moment is to fully assemble a module and test it using a radioactive source. If the module turns out to be of poor quality, it is disassembled and sent for rework. The turnover time of this operation is of the order of one month, which affected the DBM installation schedule significantly.

Only the modules that passed the pixel connectivity test undergo the second test stage in which the sensor’s efficiency was estimated. A scintillator is placed underneath the module and is used as a trigger. A particle that crosses the DBM module and hits the scintillator, triggers the module readout. In the end, the number of triggers is compared to the number of hits/clusters recorded by the module. The resulting ratio gives an estimate of the sensor’s detection efficiency. The real sensor efficiency can only be measured in a particle beam and using a beam telescope as a reference detector. Nonetheless, the *pseudo-efficiency* gives a rough estimate of the sensor’s quality.

The results for the DBM QC are shown in section 4.4. All in all, 79 modules went through the QC procedure – 43 diamond modules and 36 silicon modules, 12 of the latter only for testing purposes. Figure 4.6 shows their production with time. 18 diamond modules and 6 silicon modules were in the end chosen to be made up into DBM telescopes and installed into ATLAS.

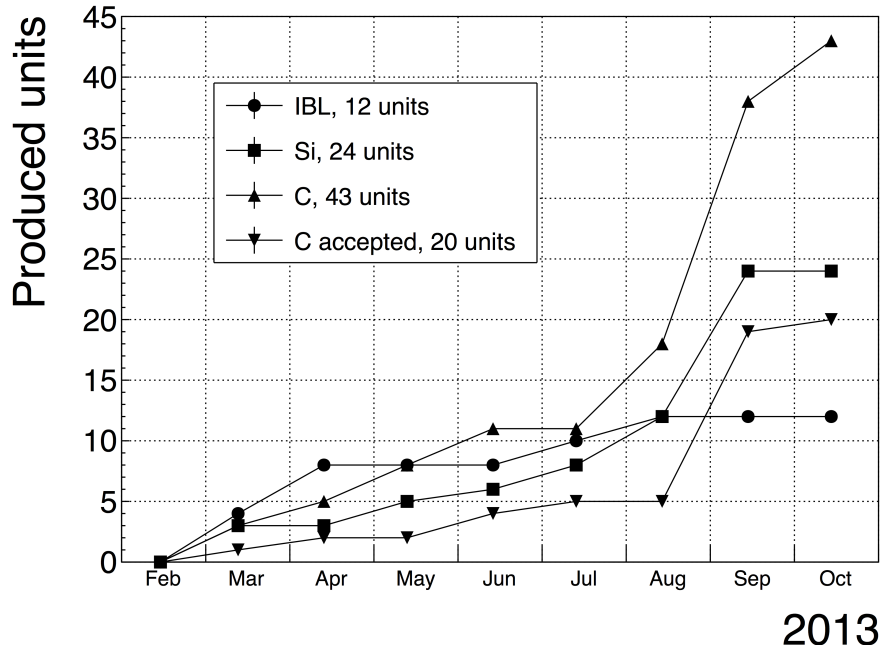


Figure 4.6: Module production with time

1895 A very important issue is the so called erratic current. This term describes the
 1896 leakage current in a pCVD diamond that becomes unstable. It can develop gradually
 1897 or can be triggered with a β source. Spikes appear in the otherwise stable leakage
 1898 current. They can be up to three orders of magnitude higher than the base current.
 1899 Sometimes the current also suddenly increases for a few orders of magnitude and stays
 1900 at that level (e.g. from the initial 1 nA to 3 μ A). The amplitude differs in magnitude
 1901 from sensor to sensor. This effect is still not fully explained, but the hypothesis
 1902 is that the charges find a conductive channel along the grain boundaries, causing
 1903 discharges. These discharges are picked up by the pixel amplifiers in the FE-I4. A
 1904 single discharge can trigger a group of up to \sim 500 pixels, resulting in a *blob* on the
 1905 detector occupancy map. Sometimes the conductive channel stays in a conductive
 1906 state, making one or more pixels always to fire. These pixels only use the bandwidth
 1907 of the readout channel, so they have to be masked out during measurements.

1908 4.3.3 Installation and commissioning

1909 The DBM modules that passed the QC tests were assembled into telescopes – sets of
 1910 three modules one behind the other with a spacing of 50 mm. Of the 18 diamond and
 1911 6 silicon modules, 6 diamond and 2 silicon modules were built. A special care was
 1912 taken when choosing the sets of three diamonds. The modules with a similar pseudo-
 1913 efficiency, leakage current, maximum stable high voltage and shape of disconnected
 1914 regions were grouped together. After assembly into telescopes, the modules were
 1915 tested for their connectivity. Then the high voltage was applied and the leakage
 1916 current was observed. This was an important point to check because all three modules

4.4. PERFORMANCE RESULTS

1917 shared the same high voltage channel. Any instabilities on one of the modules would
1918 cause problems on the other two. This would for instance happen if one of the modules
1919 had a much lower breakdown voltage.

1920 Due to time constraints, the telescopes were not built at the same time but in-
1921 stead the production was pipelined. As soon as two telescopes were ready, they were
1922 transported to Point 1 – the site where parts of the ATLAS detector were being put
1923 together. There they were prepared for installation onto the pixel detector struc-
1924 ture that had been extracted from ATLAS due to pixel detector commissioning. The
1925 commissioning was nearing completion, so the technicians were preparing the detec-
1926 tor for re-insertion. The cylindrical structure was being closed off by four new service
1927 quarter-panels (nSQPs). This meant that with every day the access to the place
1928 of installation of the DBM was more difficult. The first two telescopes were still put
1929 into place when only one nSQP was in place. This allowed the installation process
1930 to be carried out from both sides. This proved to be helpful, because the process
1931 was lengthy and had to be done with great precision. It involved tightening several
1932 screws on both sides of the telescopes, adding thermal paste on the aluminium joints
1933 and removing the protective covers, revealing the fragile wire bonds. At the same
1934 time the surrounding electronics and cables had to be left untouched. The lessons
1935 learnt with the first part of the installation were helpful when installing the other tele-
1936 scopes. The last two were fitted onto the structure when three nSQPs were already
1937 in place, leaving only a narrow opening for access. The whole procedure was carried
1938 out blind. After every installation, the telescopes were tested again. First, the low
1939 voltage connectivity was checked and a set of tests was run on the FE-I4 front-end
1940 chips. An eye diagram was made to estimate the quality of the signal transmission.
1941 Then a ^{90}Sr source was used to perform a source test on three modules at the same
1942 time. Leakage current was observed during the source test. The final test included
1943 running four telescopes (all on one side) at a time. All the tests were successful and
1944 the DBM was signed off.

1945 4.4 Performance results

1946 This section gives an overview of the performance results of the DBM modules
1947 achieved during the QC and the test beam campaign. The source tests were per-
1948 formed to check for disconnected regions in the sensors and to measure the diamond's
1949 pseudo-efficiency. Only the modules with minimal disconnected regions and maxi-
1950 mum pseudo-efficiency were chosen for installation.

1951 4.4.1 Source tests

1952 All modules went through the same procedure when tested using a ^{90}Sr source – to
1953 check for disconnected regions and to measure the pseudo-efficiency.

1954 The setup consisted of a placeholder for the ^{90}Sr source, an X-Y moving stage
1955 with a holder for the module and a scintillator with a photomultiplier placed below

1956 the source and the module. The scintillator was used as a trigger – when it detected a
1957 particle, it triggered the readout of the module. If the module was placed in between
1958 the source and the scintillator, the particle had to traverse the module to hit the
1959 scintillator. Therefore, in the case of a module with a 100 % efficiency the triggered
1960 data read out by the module would need to contain at least one hit in the module. In
1961 reality the β particles scatter around the setup and sometimes hit the scintillator from
1962 other directions, without incident the module. This produces empty triggers. The
1963 phenomenon sets the limitation of measuring with a radioactive source as compared
1964 to the measurements in a test beam, in which the particles in principle always travel
1965 in one direction and their scattering is minimal.

1966 The test for disconnected regions was carried out by moving the module under the
1967 source in X and Y direction so that the exposure over the whole plane was uniform.
1968 This resulted in an occupancy scan seen in figures 4.7a and 4.7b. The silicon module
1969 had a very uniform occupancy plot. So much so that the features of the overlaying
1970 flexible PCB can be observed. The rectangular shadows are the passive components
1971 whereas the lines are the traces in the PCB. Furthermore, a circular-shaped edge of
1972 the PCB can be seen on the bottom right side of the plot. These darker areas are
1973 such because fewer electrons can penetrate the material with a high density. In the
1974 case of the diamond, the features of the PCB can be observed as well, but are much
1975 less distinguishable. In principle, the plot is much more granulated – less uniform.
1976 This high variance in the diamond’s detection ability is due to the grain boundaries
1977 in the pCVD material which trap the drifting charges, rendering some regions much
1978 less efficient.

1979 The pseudo-efficiency test was carried out by placing the module directly below the
1980 source and collimating the particles so that their trajectory was incident the module
1981 in the middle. For every trigger by the scintillator, a script checked whether there
1982 was a hit recorded in the module or not. The resulting ratio between the number
1983 of triggers and number of hits recorded in the module is a pseudo-efficiency – an
1984 estimation of the sensor’s efficiency. It cannot give a precise value due to the triggers
1985 produced by scattered particles, but at least gives a rough estimate.

1986 Figure 4.8a shows the distribution of disconnected regions across all tested mod-
1987 ules. Silicon modules were performing as expected, with a minimum number of dis-
1988 connected pixels. The majority of the silicon modules yielded the pseudo-efficiency
1989 of $(94.3 \pm 0.2) \%$. Silicon sensors being 99.99 % efficient, this value was underesti-
1990 mated by about 5 %. The measured pseudo-efficiency of the diamond modules was
1991 $(65 \pm 7) \%$, with outliers down to 10 %. The value depended on the diamond quality,
1992 the set threshold and the applied bias voltage. The latter two settings were varied to
1993 check the behaviour of the modules under various conditions.

1994 4.4.2 Test beam results

1995 The first two assembled prototype DBM modules, MDBM-01 and MDBM-03, were
1996 tested at DESY, Hamburg, in a test beam facility. The aim of the measurements was

4.4. PERFORMANCE RESULTS

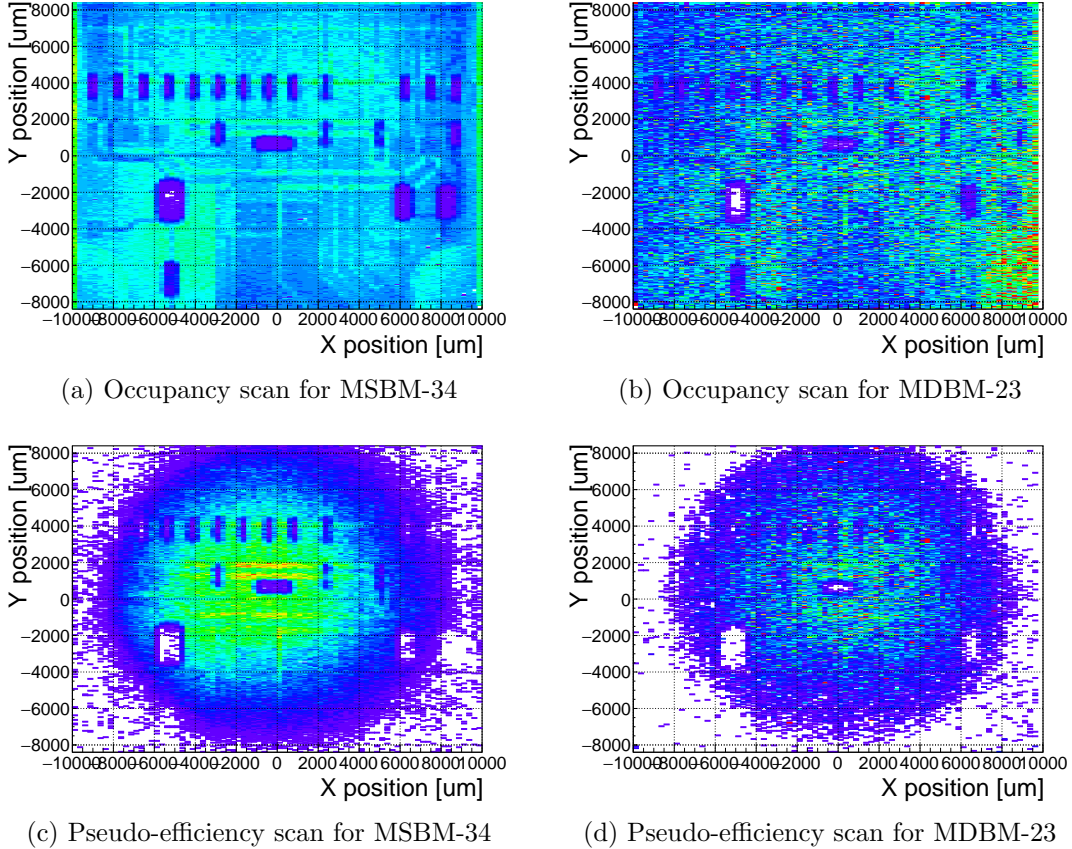
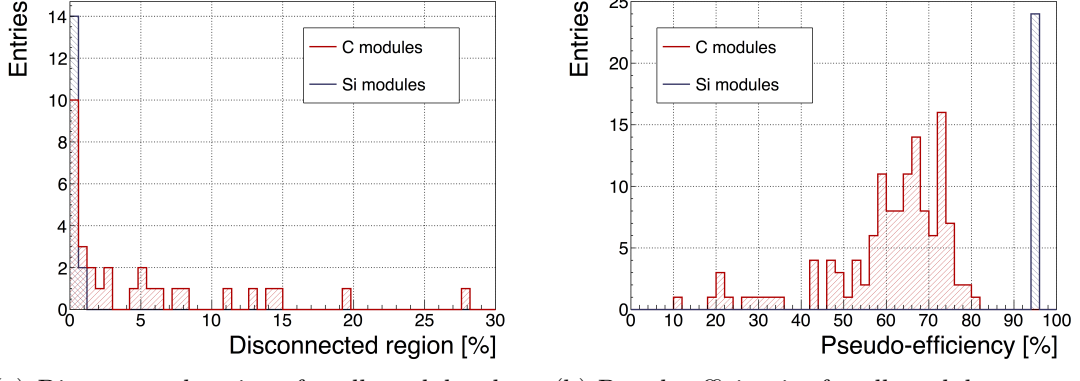


Figure 4.7: Occupancy and pseudo-efficiency scans for the silicon (left) and diamond sensor (right) to check for disconnected regions and estimate the sensor’s efficiency. Shadows of the electronic components are clearly visible because fewer electrons were able to traverse through such a higher amount of material.

to measure their efficiency, the spatial distribution of the efficiency and the effect of the beam on the disconnected regions. A silicon module MSBM-02 was measured to crosscheck the measurements. Since the silicon module is almost 100 % efficient, it was used as an “anchor” – the efficiency of the diamond module was measured relative to that of the silicon module. Two beam telescopes were used as reference systems: Kartel [], built by JSI institute from Ljubljana, and EUDET Aconite []. Both are instrumented with six Mimosa26 pixel planes and capable of tracking particles with a 2 μm pointing resolution.

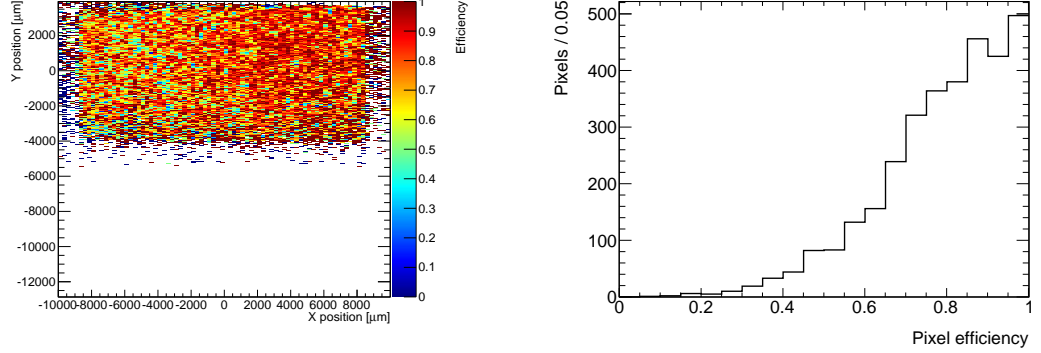
The test beam prototypes did not meet the acceptance criteria for production DBM modules in the following areas: first, the stated CCDs were slightly below 200 μm , which would be the DBM minimum. Secondly, the applied bias voltages ranged from 1–2 V/ μm . In addition, the threshold cut could only be set to 1500 electrons, which is higher than the DBM minimum (1000 e). Nonetheless, the resulting module efficiencies were still in the range between 70–85 %.

To analyse the test beam data, Judith [] software framework was used. Judith is



(a) Disconnected regions for all modules derived from the occupancy scans (b) Pseudo-efficiencies for all modules at various threshold and voltage settings

Figure 4.8: Measurements of pseudo-efficiency and disconnected regions for all modules that went through the QC procedure



(a) This is an efficiency distribution. Each bin corresponds to a single pixel. The triggering scintillator of the Kartel telescope was smaller than the DUT. Hence, the recorded hits can only be seen in the top half of the sensor.

(b) Pseudo-efficiencies for all modules at various threshold and voltage settings

Figure 4.9: An efficiency study of a prototype DBM diamond module in a test beam. The statistics are low (~ 10 hits/pixel) as the data was collected during a short run.

2012 capable of synchronising data streams from several detector systems only connected
 2013 via a trigger system, reconstructing tracks and calculating efficiency for the DUTs. It
 2014 was also used to reconstruct and analyse the acquired Kartel test beam data together
 2015 with the silicon and diamond module as DUTs. A sample of the analysed data is
 2016 shown in figures 4.9a and 4.9b.

4.5. OPERATION



Figure 4.10: This photo highlights four telescopes installed onto the nSQPs and around the pipe

2017 4.5 Operation

2018 4.5.1 Positioning

2019 The DBM is placed in the forward region of the ATLAS detector, very close to the
2020 beam pipe (see figure 4.11). The mechanical structure that holds the sensor planes is,
2021 due to its shape, referred to as a DBM telescope. A telescope is a system that consists
2022 of several pixel sensors placed in series one behind the other. Each DBM telescope
2023 houses three diamond pixel modules. Eight DBM telescopes reside approximately
2024 1 m away from the collision region, four on each side. They are tilted with respect
2025 to the beam pipe for 10°. This is due to a specific phenomenon connected to erratic
2026 (dark) currents in diamond. Studies have shown [1] that the erratic leakage currents
2027 that gradually develop in diamond can be suppressed under certain conditions. For
2028 instance, if a strong magnetic field is applied perpendicular to the electric field lines
2029 in the diamond bulk, the leakage current stabilises [2]. The DBM was designed to
2030 exploit this phenomenon. The magnetic field lines in the ATLAS experiment are
2031 parallel to the beam. Hence, an angular displacement of the sensor with respect to
2032 the beam allows for the leakage current suppression. However, the DBM telescopes
2033 still need to be directed towards the interaction region. Taking these considerations
2034 into account, a 10° angle with respect to the beam pipe was chosen. The influence

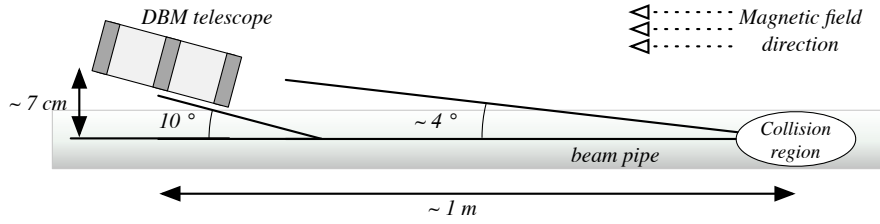


Figure 4.11: Position of the DBM in the ATLAS experiment

of the magnetic field on the particle tracks at this angle is very low as the field lines are almost parallel to the tracks. The tracks are therefore straight, which reduces the track reconstruction complexity.

4.5.2 Data taking during collisions

The DBM has been commissioned in ATLAS and is now taking data. Several issues still need to be resolved regarding the readout systems. Unfortunately, due to issues with the low voltage power supply regulators, six out of 24 modules were damaged during operation: four silicon and two diamond modules. The system configured the modules into an unsteady state whereby they drew twice as much current as the allowed maximum. This current most probably fused the wire bonds within minutes. This has left only five diamond telescopes fully operational. The preliminary data obtained using the remaining telescopes show that the background rejection could indeed work.

The first step of the system test was to take data during collisions and check the occupancy in the individual modules. The occupancies were plotted side by side for comparison. Figure 4.12 shows some of the occupancy values. At the time, the readout system was not yet configured to read out all telescopes in parallel.

The second step was to test the detector's capability of particle tracking. Only one telescope was used to take data with the beam. If all three planes of the telescope were hit during a bunch crossing, a linear line was fitted to the hits. This line represented the particle's trajectory. It was projected towards the interaction point. Two parameters were calculated where the line is the closest to the interaction point: the radial distance and the longitudinal distance between the line and the interaction point (see figure 4.13). This was done for the events with two colliding bunches as well as for events with only one, non-colliding bunch. The tracks recorded during the events with two colliding bunches could either come from the collisions or could be background scattering. Tracks recorded during a non-colliding bunch, on the other hand, are definitely background particles since, in principle, there should be no collisions taking place.

A comparison of the data acquired (see figures 4.14a and 4.14b) showed that, for the colliding bunches, the majority of the reconstructed tracks had the origin in the

4.5. OPERATION

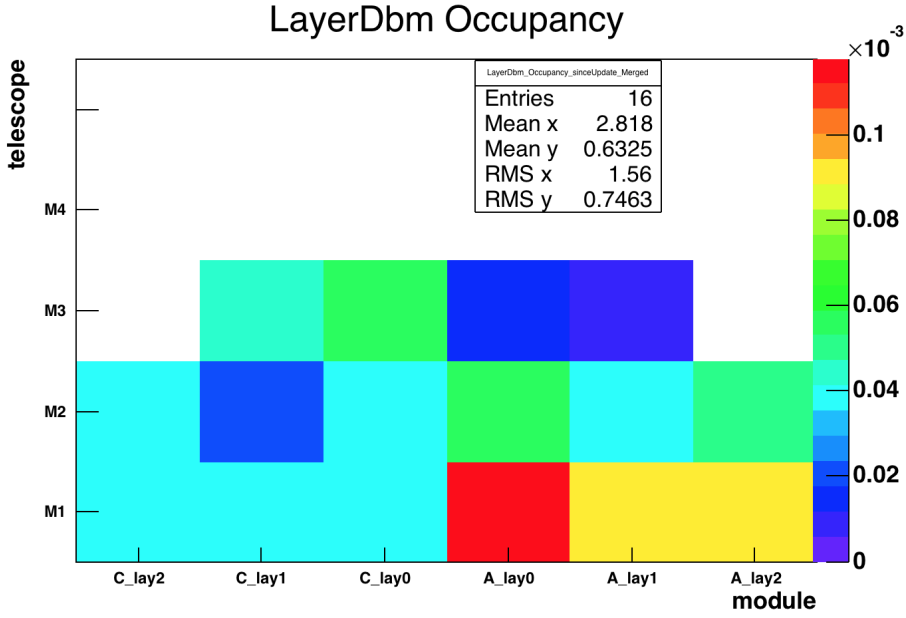


Figure 4.12: Occupancy of individual modules during collisions. Only 16 modules were taking data.

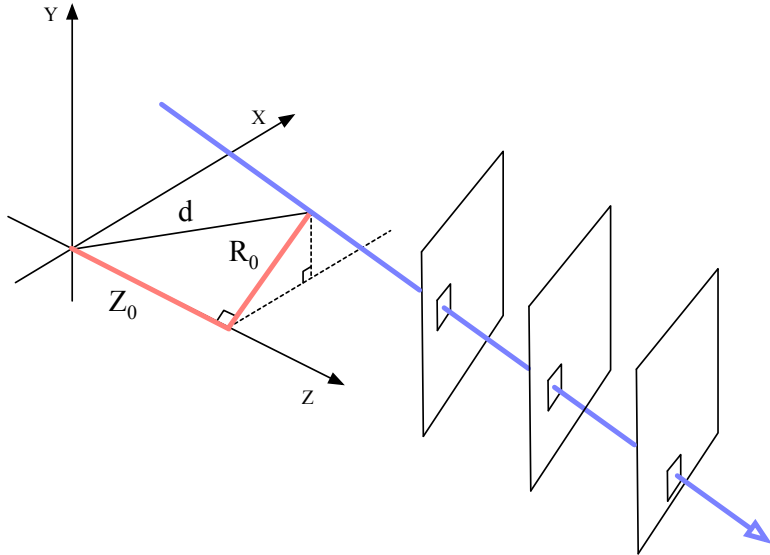
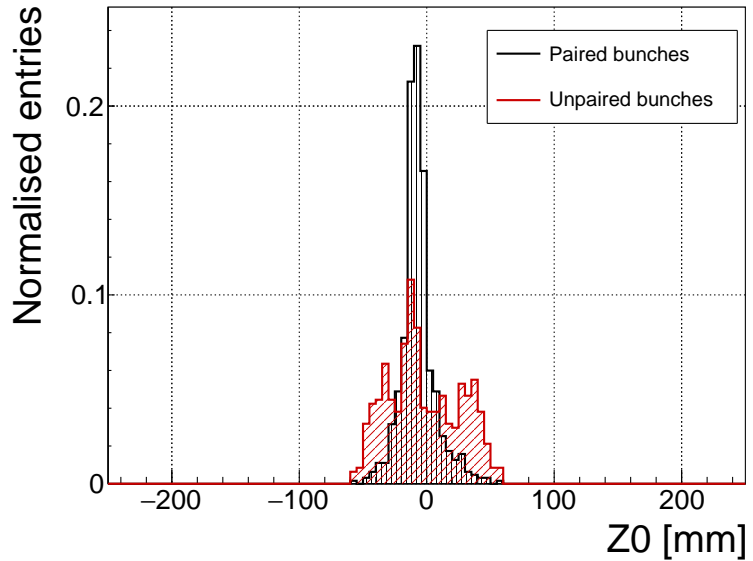
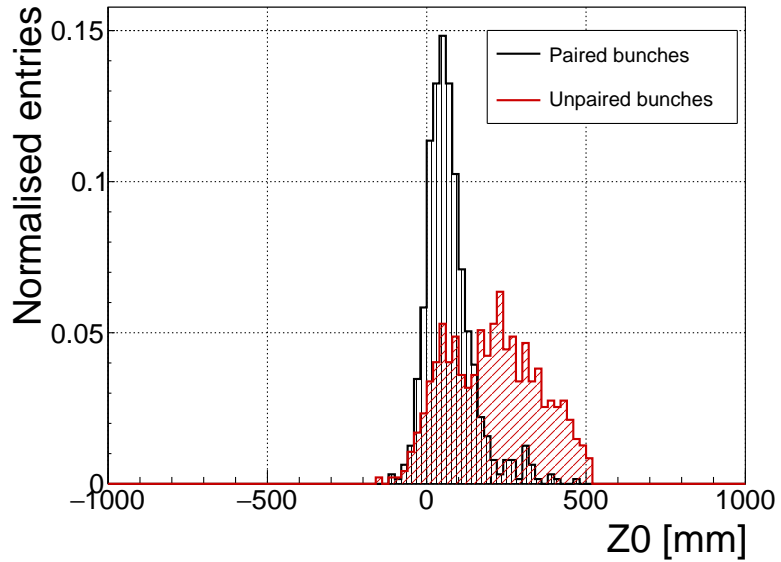


Figure 4.13: A diagram showing the radial distance R_0 and longitudinal distance Z_0 of the trajectory from the interaction point at the minimal distance d . Z is the axis along the beam line. Three module planes intercept a particle and reconstruct its trajectory.

interaction point, with an expected spread in Z and R . For non-colliding bunches, the distribution is more spread out. In the Z_0 plot the distribution has one peak in the middle, which means that the empty RF buckets still held some particles. The



(a) Radial distance of the particle trajectories from the interaction point



(b) Longitudinal distance of the particle trajectories (along the beam path) from the interaction point

Figure 4.14: These two plots show two parameters of particle tracks recorded by one of the DBM telescopes: radial and longitudinal distance of the projected tracks from the interaction point.

²⁰⁶⁹ two peaks on the sides, however, show that a significant number of tracks had their
²⁰⁷⁰ origin at the radius of the beam pipe. Therefore these tracks were made by stray
²⁰⁷¹ protons colliding with the beam pipe. These collisions are unwanted as they do not
²⁰⁷² produce any meaningful physics while still damaging the ATLAS detector by means
²⁰⁷³ of the scattered radiation.

2074 **4.6 Conclusion**

2075 The Diamond Beam Monitor has been designed as an upgrade to the existing lu-
2076 minosity detectors in the ATLAS experiment. It is the first diamond pixel tracking
2077 detector installed in a high-energy physics experiment. The pixelated front-end elec-
2078 tronic chips ensure precise spatial detection of the charged high-energy particles.
2079 The projective geometry allows for particle tracking and background rejection. The
2080 detector is placed in a high-radiation forward region of the experiment. Therefore,
2081 radiation hardness of the chosen pCVD diamond sensors is an important requirement.
2082 The tests carried out in the test beam and in the laboratory confirmed that enough
2083 detector-grade DBM modules have been built to be installed in the experiment. The
2084 DBM is now running in ATLAS during collisions. Further improvements have to be
2085 made on the readout firmware before it is included in the main readout stream.

2086

Chapter 5

2087

Current monitoring

2088

Real-time particle identification

2089 Diamond sensors have a very fast signal response due to their low capacitance. The
2090 electrical signal created by drifting charge carriers retains its shape without significant
2091 distortion. When the sensor is used together with a fast current amplifier with a high
2092 broadband limit (~ 2 GHz) and a readout device with a similar limit, the information
2093 about the drifting charges is retained. For instance, a proton creates the free e-h pairs
2094 along its trajectory. The electrons and holes start drifting immediately. Those closest
2095 to the electrodes recombine quickly whereas those at the opposite side contribute to
2096 the induced signal for longer. The resulting signal is therefore a triangular pulse
2097 with a steep rising edge and a gentle falling edge. It is possible to determine the
2098 drift velocity of the charge carriers by measuring the width of the pulse, as was done
2099 in chapter ??. Furthermore, it is possible to determine with a certain probability
2100 what is the type of incident radiation, judging by the shape of the induced pulse.
2101 This, however, only applies to sCVD diamond material. Its uniform carbon lattice
2102 allows the ionisation profiles to retain their shape, unlike in pCVD material, laden
2103 with grain boundaries, or in even in silicon where the shape is deformed due to p-n
2104 junction non-uniformities.

2105 This chapter describes an application that carries out particle identification by
2106 means of the pulse shape analysis. It was developed for measuring activity of a
2107 neutron reactor. In this case the device has to be able to filter out the photon
2108 background with a rate several orders of magnitude higher than the neutron rate.
2109 Overall detected rate in a neutron reactor can easily exceed 10^8 particles $\text{cm}^{-2}\text{s}^{-1}$,
2110 depending on the distance of the detector from the reactor core. The device has to
2111 be able to cope with such high rates. It also needs to be dead time free or at least
2112 close to that, to minimise the counting error. At these rates, it still has to be able to
2113 identify the types of pulse. This type of online analysis cannot be done in software.
2114 It has to be implemented in an FPGA.

5.1 MOTIVATION

2115 5.1 Motivation

2116 Pulse shape analysis (PSA) is a common software tool for analysing sensor response
2117 to incident particles. It is usually done by means of software that runs over big
2118 amounts of data that have been acquired and saved to storage. This offline analysis
2119 can be repeated and improved. However, the saved data take up a lot of storage
2120 space. In addition, saving raw waveform data requires a system capable of a high
2121 data throughput and fast data storing. For instance, an oscilloscope can save up
2122 to 100 signal waveforms per second. This means that there is a high measurement
2123 dead time. To avoid the high dead times, the software algorithms can be ported
2124 to the FPGA where they analyse the incoming signal in real time. The signal is
2125 then discarded and only the analysis results are saved, decreasing the storage space
2126 significantly.

2127 The offline pulse shape analysis has already been used for particle identification
2128 with a diamond sensor [29, 24]. An effort has been made to implement an online and
2129 real time application for this analysis by porting the algorithms into an FPGA. This
2130 section first describes the device specifications Then it describes in detail the PSA
2131 algorithms and the structure of the code. Afterwards it discusses the performance
2132 results, which showcase the limitations of the device. Finally it describes the data
2133 acquired with radioactive sources and in neutron reactors.

2134 5.2 Requirements

2135 Chapter ?? shows that the shape is heavily dependent on several factors, such as
2136 environmental temperature and received irradiation dose. At temperatures lower
2137 than 150 K the signal from an α starts deteriorating due to recombination of charges
2138 in the charge cloud. Sensor irradiation, on the other hand, introduces charge traps,
2139 which cause the signal to decay exponentially. These two factors are a significant
2140 limitation for particle identification. Priming can improve the charge collection and
2141 longterm stability of the pulse shapes. To improve the measurement further, a high
2142 bias voltage has to be applied, increasing the measurement SNR.

Factor	Operating range
Sensor material	sCVD diamond
Sensor thickness	500 μm
Temperature	150 K – 400 K
Radiation dose	$1 \times 10^{13} \text{ neq cm}^{-2}\text{s}^{-1}$
Charge carriers	holes
Bias voltage	$\sim 1 \text{ V } \mu\text{m}^{-1}$
Signal-to-noise	5

2144 Table 5.1: Limitations to particle identification

2145 **5.3 Device specifications**

2146 The ROSY box has a single BNC input with the termination $50\ \Omega$ or $1\ M\Omega$ with a
2147 DC or AC coupling. The analog chain has a 250 MHz bandwidth limit. The input
2148 range can be set from $\pm 50\text{ mV}$ up to $\pm 5\text{ V}$. The signal offset can be set to any value
2149 within this range. The ADC samples this signal with an 8-bit precision at a rate of
2150 up to 5 GSPS. The PSA uses the highest sampling to achieve width measurement
2151 resolution of 0.2 ns. The spectroscopic application does not need such a fine timing
2152 resolution and therefore operates at a reduced sampling rate of 0.8 ns. The amplitude
2153 resolution depends on the chosen input range, but at 256 ADC counts per sample, it
2154 can be as low as 0.39 mV s^{-1} at the range of $\pm 50\text{ mV}$ and as high as 39 mV s^{-1} at
2155 the range of $\pm 5\text{ V}$.

2156 The logic structure of the PSA is designed using VHDL and runs on Xilinx Vir-
2157 tex 5. The PSA is capable of a maximum counting rate of 1.56×10^8 pulses per second,
2158 yielding a 6.4 ns double pulse resolution. The analysis is more time consuming; the
2159 maximum throughput rate of the pulse shape analysis is $\sim 5 \times 10^6$ pulses per sec-
2160 ond. This means that after every pulse, the device has a dead time of approximately
2161 (200 ± 15) ns, depending on the width of the pulse being analysed. Any pulse arriving
2162 during the analysis of the previous one will be counted, but not analysed. Any two
2163 pulses with the distance between the rising edges lower than 6.4 ns will be counted
2164 as a single pulse.

2165 The device is very sensitive to noise pick-up. Therefore the setup must be designed
2166 to minimise the pick-up by means of proper shielding, use of high-quality cables etc.
2167 The relatively low bandwidth limit filters out some high-frequency noise, but not the
2168 ringing or higher noise spikes. That is the task for the PSA.

2169 **5.4 Pulse parameters**

2170 A signal pulse on the input is parametrised during the analysis process. The PSA
2171 measures its amplitude, area, width and the slope of its falling edge (see figure 5.1).
2172 The amplitude is the difference between the baseline and the highest sample in the
2173 pulse and is given in ADC counts as an 8-bit value. The area is defined as the sum
2174 of amplitudes of all samples between two defined boundaries within the pulse. The
2175 width is defined as the number of samples with a value higher than a set amplitude
2176 threshold. If the threshold is at half the maximum amplitude, the resulting width
2177 is *full width at half maximum* (FWHM). The falling slope is the maximum negative
2178 difference between values of two samples and is given in ADC counts per sample.
2179 These parameters can also be used as *qualifiers* for accepting or discarding a pulse.
2180 All four parameters limited by the low and high limit are called a *qualifier set*. For
2181 instance, a rectangular pulse by an α particle will always have the same FWHM and
2182 a very steep slope. In comparison, a photon will have a lower falling slope value and
2183 a narrower FWHM. Therefore the low and high cut on these two qualifiers will make
2184 it possible to discriminate between the two pulses. Another qualifier is a *form factor*

5.5. APPLICATIONS

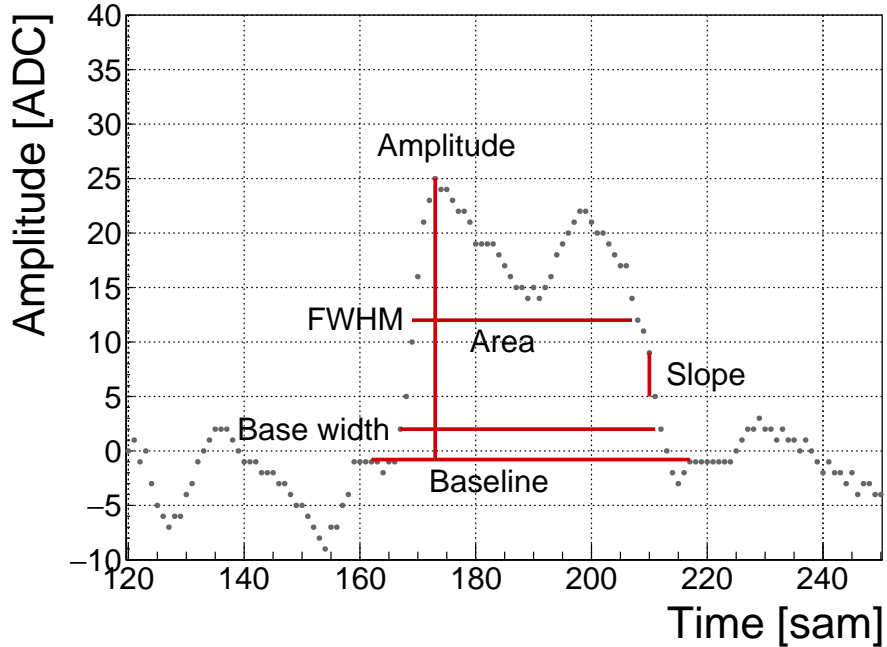


Figure 5.1: A pulse and its parameters

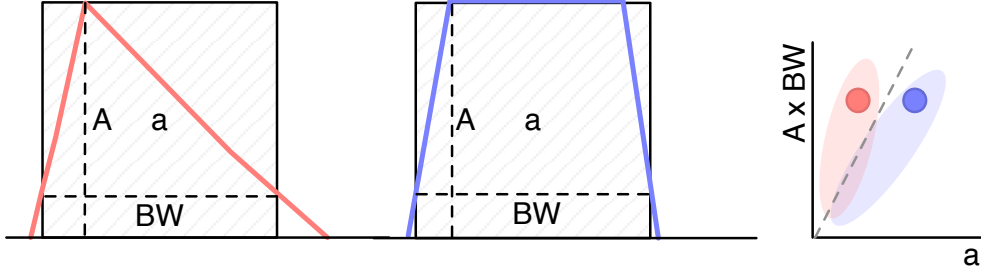


Figure 5.2: Form Factor is the ratio between the measured area (a) and the calculated area ($A \times BW$) of the pulse. The calculated area is significantly larger than the measured area for a triangular triangular pulse, but less so for the rectangular one. The red and blue dot in the right plot are the value entries of the two pulses shown. The red and blue oval shapes depict the regions for the values expected from triangular and rectangular pulses. By carefully choosing the linear qualifier (dashed line) and taking only the entries below the cut rectangular pulses can be identified.

and is defined as the ratio between the measured area and the amplitude multiplied by the width. By comparing the measured and the calculated area the difference between a triangular and a rectangular pulse can be inferred (see figure 5.2).

2188 **5.5 Applications**

2189 The FPGA firmware is designed for systems instrumented with CIVIDEC amplifiers
2190 and CIVIDEC sVCD diamond detectors. Three applications are available: *Spectroscopy*,
2191 *Pulse Shape Analysis* and *Counter*, each optimised for a specific task. Their
2192 capabilities are described below. The firmware runs in ROSY, a readout system
2193 produced by CIVIDEC.

2194 **Spectroscopy** is a tool for measuring energy spectra of radioactive sources. It is
2195 used in combination with the CIVIDEC Cx spectroscopic charge amplifier. The
2196 signal from the charge amplifier is analysed in real time. The FPGA measures the
2197 maximum amplitude of the signal. The amplitude value is ready at the end of the
2198 pulse and is stored in the amplitude histogram. Immediately after, the analysis is
2199 reset and the system is ready for a new acquisition. Upon request from the software,
2200 the histogram is read out, during which the analysis is paused. In addition to the
2201 histogram building, the firmware can also store raw pulse waveforms, which can be
2202 then read out by the software. The maximum allowed throughput is 1 million counts
2203 per second.

2204 **Pulse Shape Analysis** is a tool for measuring energy spectra of radioactive sources,
2205 with an additional feature. It can identify the type of radiation detected by the
2206 diamond detector. By means of the pulse analysis it can subtract the background
2207 radiation and only measure the signals from the defined radiation source. It is used
2208 in combination with the CIVIDEC C2 fast current amplifier. The firmware receives
2209 a current pulse from the detector and digitises it. The pulse is then analysed and
2210 parametrised. The analysis module measures its maximum amplitude, full width
2211 at half maximum (FWHM), baseline amplitude, falling slope and its area. Then
2212 it compares the obtained pulse parameters with the qualifiers set by the software
2213 and determines what type of radiation hit the diamond detector. Depending on the
2214 qualifiers, the pulse can either be *accepted* or *rejected*. The firmware then stores the
2215 parameters of the analysed pulse into histograms. Two histograms exist for each
2216 parameter: one for all pulses and one for accepted pulses. In addition, there is one
2217 2D histogram (a scatter plot), which can plot two parameters one with respect to the
2218 other. Upon request from the software, all histograms are read out, during which the
2219 analysis is paused. The maximum allowed throughput is 1 million counts per second.

2220 **Counter** is a tool that measures the count rate and the mean time during counts.
2221 It is used in combination with the CIVIDEC Cx, C6 or C2 amplifier. It contains
2222 one histogram which holds the information about the mean time during counts. The
2223 counter is operational also during the readout of the histogram. The highest counting
2224 rate with enabled histogram writing is $3 \times 10^7 \text{ s}^{-1}$.

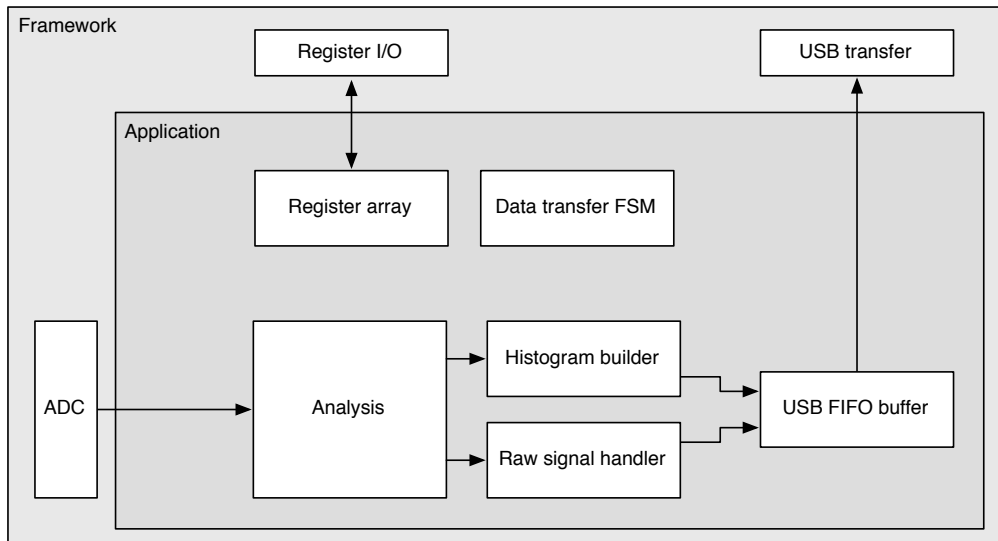


Figure 5.3: Firmware design structure

5.6 Description of the firmware

The applications are built on top of the Picotech platform. The base code handles the communication between the software and the hardware. Furthermore, it provides the interface to the ADC data, the input/output registers and the USB data transfer. The applications have a set of modules that handle the data input and output and a module for signal analysis (see figure 5.3).. The data handling modules are very similar in all the applications to ensure compatibility of the communication between software and firmware and the readout data format. The analysis module, however, is different from one application to the other. The data handling layer is the same for all applications and consists of the final state machine (FSM), the histogram builder, the raw signal handler, the USB FIFO buffer and the register array.

The firmware is written entirely in VHDL. The diagram in figure 5.3 shows the module architecture. The ADC provides the module with 32 digitised signal samples every clock cycle (6.4 ns). The signal is routed directly to the pulse analyser and into the raw signal handler. The analyser outputs are connected to the I/O registers and to histogram buffers. Both the histogram buffers and raw signal buffers are connected to the USB FIFO through a multiplexor. The firmware communication to the controller is done via input/output (I/O) registers (control and status registers, counters) and serially via USB (histogram data, waveforms).

5.6.1 Design constraints

Speed The ADC provides 32 8-bit samples on every 6.4 ns clock cycle. It is not possible to e.g. sum all 32 values in a single cycle, because the summation takes too long to complete. This is why the summation has to be pipelined and carried out

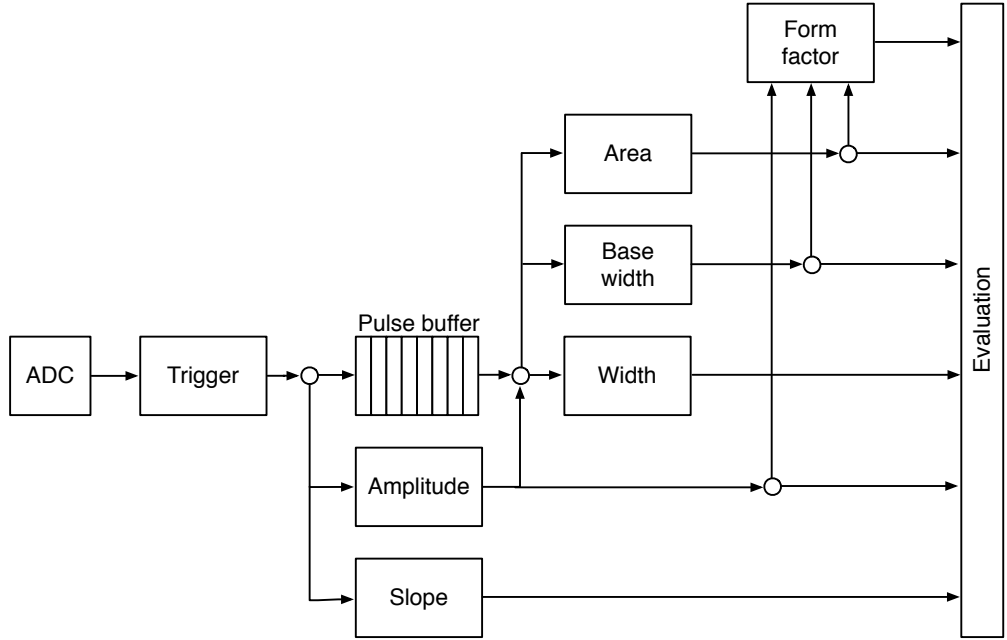


Figure 5.4: Code design plan

in three cycles. This adds up to the analysis duration, which in turn decreases the maximum pulse rate.

Firmware size The PSA application makes use of a number of FIFO and RAM buffers to store the pulse waveforms and histograms. 48 32k block RAM modules have been used for the implementation, maxing out the available block RAM memory space on this FPGA. The analysis algorithm also takes up a significant portion of the FPGA. Many of the operations are carried out on 256-bit long numbers received from the ADC, which quickly fills up the available logic. This is also why the place and route procedure takes a long time.

Power consumption The reduction of the power consumption is not crucial for the intended applications.

5.6.2 Analysis module

This module is different for different applications. The Pulse Shape Analysis (PSA) application has the most complex module design. The spectroscopy application only uses a small part of that design and the Counter application an even smaller one.

The analysis (or parametrisation) is carried out in several steps, as shown in figure 5.4. The triggering block starts the readout upon signal threshold crossing. The maximum slope of the falling edge is observed. The Amplitude block calculates the pulse height and retains the maximum amplitude while pushing the signal into the pulse buffer. Then the whole pulse is clocked out of the buffer while its FWHM,

5.6. DESCRIPTION OF THE FIRMWARE

2268 baseline width and area are measured. Finally, the Form factor is calculated. At the
2269 end the Evaluation block takes in all the parametrised information and classifies the
2270 pulse according to user-defined cuts.

2271 **Triggering** module handles signal polarity swapping, triggering on threshold and
2272 defining the trigger window. The real-time processing algorithm allows for a pos-
2273 itive or an inverted input signal. However, the PSA only handles positive-polarity
2274 pulses. Therefore a negative signal is swapped in the *triggering* block. Signal analysis
2275 and readout are then triggered when the signal crosses a user-defined threshold. In
2276 addition, the signal has to be over the threshold for a defined number of samples.
2277 This is to avoid triggering on noise spikes. A double clock cycle delay is used on the
2278 signal to make sure that the recorded signal window will include the rising edge of
2279 the pulse as well as some baseline before it. A *trigger active* signal marks a window
2280 that contains the whole pulse including some baseline signal before and after it. The
2281 trigger can be vetoed by three signals: if the pulse analysis is still taking place, if
2282 the input signal exceeds the maximum voltage range or if the data transfer FSM is
2283 pausing the analysis due to data transfer to the controller.

2284 **Amplitude** block calculates the pulse height from the difference between the pulse
2285 and the baseline. It also finds the position of the maximum amplitude within the
2286 clock cycle. It receives 32 8-bit samples from the triggering block every clock cycle.
2287 Time delays in the logic prevent it to find the maximum value of the 32 samples
2288 within one clock cycle (6.4 ns). Therefore the decision logic has been pipelined in
2289 three stages, which means that the final maximum value is ready three clock cycles
2290 after the end of the pulse.

2291 **Pulse buffer** is a FIFO that stores the signal while its amplitude is being measured.
2292 At the end of the pulse the FIFO is read out so that the remaining measurements
2293 can take place.

2294 **Width** block uses the maximum amplitude to determine the *half-maximum* and to
2295 measure the FWHM. To do so, it counts the samples that are above the half-maximum
2296 amplitude. However, this method might also count high enough noise spikes before
2297 or after the pulse. Hence an improved method, which “cleans” the measurement of
2298 unintentional additional noise, has been implemented. It is described in section 5.6.3.

2299 **Baseline width** block is the same as the Width block, but it measures the width
2300 either at 50 %, 25 %, 12.5 % or 6.25 %, depending on the setting in the register. It
2301 also makes use of the special method described in 5.6.3 to avoid overestimations due
2302 to including noise in the measurement.

2303 **Area** block measures the pulse area by summing up the amplitude values of the sam-
2304 ples in the pulse. The boundaries of the summation are defined with the crossing of
2305 the amplitude above a certain threshold. Only the samples between those boundaries
2306 are summed up. The boundaries can be set at 50 %, 25 %, 12.5 % or 6.25 % of

2307 the maximum amplitude of the pulse. The area measurement makes use of the same
2308 routine as the FWHM and Baseline width block to remove the potential outlying
2309 samples.

2310 **Falling slope** block measures the highest negative difference between amplitudes of
2311 two adjacent samples, thus getting the maximum negative slope of the pulse. It is an
2312 experimental routine, only used for academic purposes.

2313 **Form factor** block is used as a special qualifier for particle identification. It com-
2314 pares the weighted measured area of the pulse with its weighted calculated “form”,
2315 which is defined as the multiplication of the measured amplitude and baseline width.
2316 The equation is as follows:

$$x \cdot a - y \cdot A \cdot BW \geq 0, \quad (5.1)$$

2317 where a is the measured area, A is the amplitude, BW is the baseline width and x
2318 and y the weighting factors for the measured and calculated area, respectively. The
2319 output of the block is the boolean result of this equation.

2320 **Evaluation** block takes in all the parameters from the analysis blocks and compares
2321 them against the user-defined qualifiers. If the parameters are within the bounds,
2322 the pulse is accepted, otherwise it is rejected. The corresponding counters within the
2323 block are incremented.

2324 5.6.3 Area and width measurement

2325 The routine for measuring pulse area and width must have a specific algorithm imple-
2326 mented to carry out the measurements correctly. The core point is that the routine
2327 precisely defines the edges of a pulse. It does so by means of *vector cleaning*, pre-
2328 sented in figure 5.5. An important input, beside the ADC data and the measurement
2329 threshold, is the position of the sample with the highest amplitude.

2330 The signal arrives from the ADC as a set of 32 8-bit samples every every clock cycle
2331 with a period of 6.4 ns. All 32 samples are compared against the width measurement
2332 threshold. If a sample value is equal or higher than this threshold, a binary 1 is set
2333 in a 32-bit *vector* on the position corresponding to the position of the sample in the
2334 incoming ADC data set. The resulting vector might also include some noise at the
2335 edges of the pulse, depending on the height of the width measurement threshold. The
2336 old routine simply counts the binary ones in this vector to get the pulse width. This
2337 works well for measuring the FWHM because the threshold was high. However, for
2338 width measurements at 25 %, 12.5 % or 6.25 % of the pulse height this might already
2339 become a problem, because the noise might be counted in as well. This is why the
2340 new routine cleans the outliers in this vector before counting the remaining ones in
2341 the clean vector.

2342 The routine starts from the position of the maximum height. It follows the vector
2343 in both ways and finds the first falling edge (0 at this position and 1 at the previous

5.6. DESCRIPTION OF THE FIRMWARE

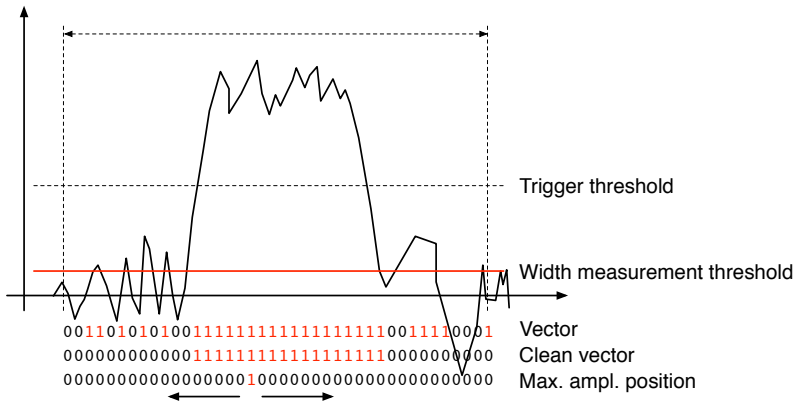


Figure 5.5: A sample pulse. The first vector shows which samples are above the width measurement height. The second vector is a clean vector. The third line shows the position of the maximum amplitude. The vector cleaning algorithm starts from the maximum amplitude and continues in both ways along the vector.

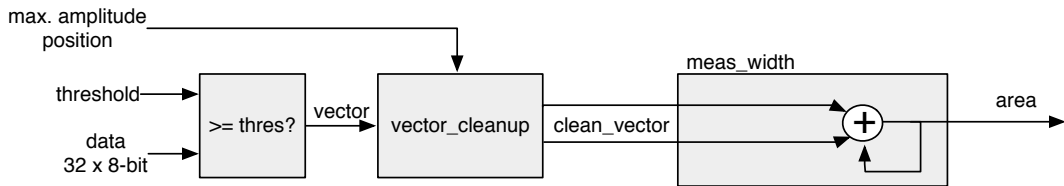


Figure 5.6: This block counts the remaining binary ones in the clean vectors and outputs this value as the pulse width.

one). From there on it rewrites any binary 1 with a binary 0. The resulting clean vector only has one bunched set of binary ones which are summed, yielding a precise pulse width. The area measurement is similar - it only integrates over the samples marked in the clean vector. Both measurement routines, for area and for width, are implemented separately so that the area routine can have a different threshold set.

This section explains how the algorithm is designed. First, the idea for it was tested using Excel and was only afterwards ported to the VHDL. The underlying algorithm first cleans the vector. Then it passes the cleaned vector either to the width or area measurement (see figures ?? and ??). The width measurement module only sums the ones in the vector whereas the area measurement module sums the data samples marked by the cleaned vector. Both modules issue a *valid* signal when they finish the measurement.

5.6.3.1 Vector cleaning

This is the most important block. Its inputs are: *vector*, *parsing active*, *position of the max. amplitude (PA)* and its delay (*DA*). PA is a 32-bit binary number that shows the position of the sample with the maximum amplitude within the data block whereas

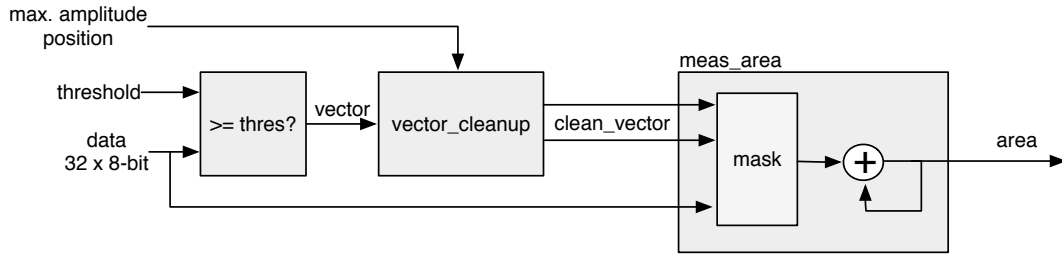


Figure 5.7: This block masks the input data with the clean vector and sums the remaining samples.

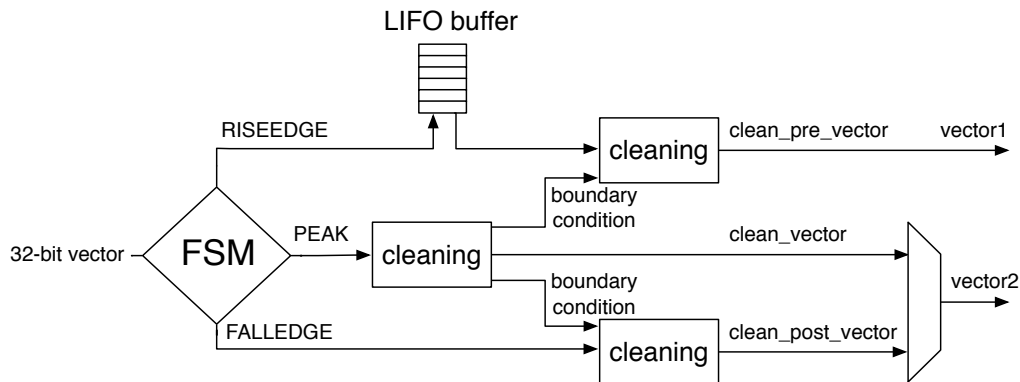


Figure 5.8: Vector cleaning routine outputs two vectors - one forward in time and one back in time from the peak of the pulse.

2360 the DA tells us how many clock cycles after the start of the parsing this PA block
 2361 is. The vector cleaning module is designed as a final state machine (FSM) with the
 2362 states IDLE, RISEEDGE, PEAK, FALLEDGE and READY. The FSM is idle until it
 2363 receives the *active* signal from the external module, marking that the vector parsing
 2364 has commenced. It switches to RISEEDGE, which starts two procedures: 1) it fills
 2365 the vector of the pulse's rising edge into a last-in-first-out (LIFO) buffer and 2) counts
 2366 down from the DA value. When this counter reaches 0, the FSM changes its state to
 2367 PEAK because the current vector on the input is the one containing the maximum
 2368 amplitude. This data block is sent through the *peak algorithm*, which cleans the
 2369 vector. The FSM switches to FALLEDGE state. Now both the previously buffered
 2370 vector of the rising edge and current vector of the falling edge go through the *pre-*
 2371 *and post- algorithm* where they are cleaned, but they get their boundary conditions
 2372 from the *peak algorithm*. The output of this module is therefore two cleaned vectors
 2373 in parallel – one forward in time and the other backwards.

2374 5.6.3.2 Algorithm

2375 The underlying algorithm is sequential - it carries out a logic operation on vector bit
 2376 on position 0, uses the output of this operation for the operation on bit on position

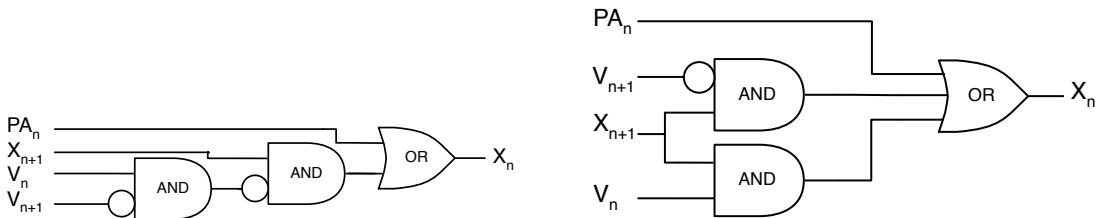


Figure 5.9: One logic step in the algorithm chain before and after Karnaugh minimisation.

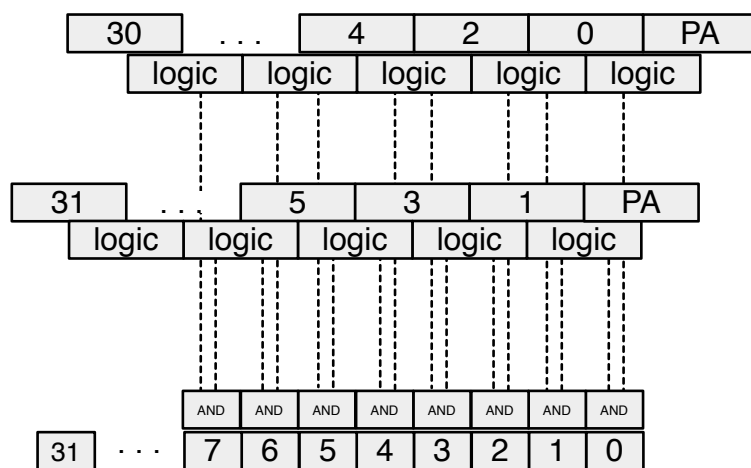


Figure 5.10: Vector is divided into two 16-bit logic chains. The algorithm logic is then run on the two chains separately. The results are then merged into one 32-bit clean vector by using a set of AND gates.

2377 1 and so on. This means that it has to carry out 32 logic operations per clock
 2378 cycle. With each operation taking approximately 0.3 ns, the whole logic chain takes
 2379 approximately 10 ns to complete. With only 6.4 ns per clock cycle, this means timing
 2380 errors would occur. To fix the problem, a more complicated *decimated algorithm* has
 2381 been designed. It consists of two parallel logic chains. Each of the two only takes
 2382 every second bit into account (chain one: 0, 2, 4 ..., 30. Chain two: 1, 3, 5 ..., 31).
 2383 This makes the chains effectively 16 bits long. The algorithm is run on the two chains
 2384 and the results are merged together at the end as shown in figure 5.10. This effectively
 2385 reduces the number of sequential logic operations to around 18, which is within the
 2386 timing constraints.

2387 5.7 Control and data interface

2388 Communication between the device and the controller PC is done via the API func-
 2389 tions provided by the producer. In addition, the API used by CIVIDEC has access

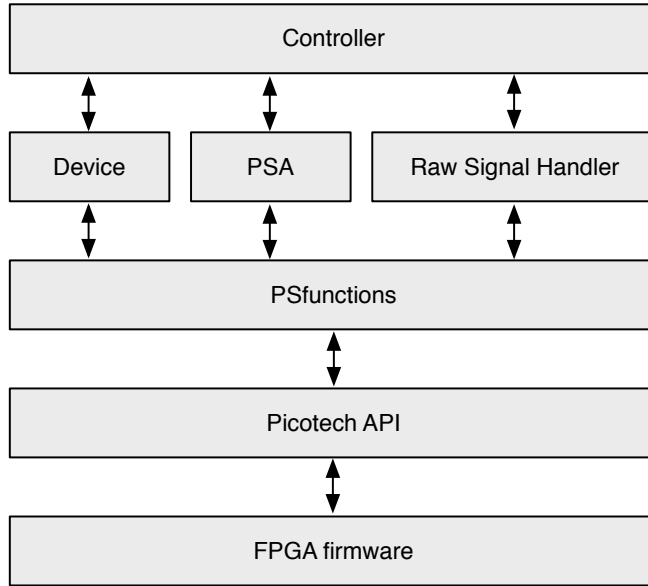


Figure 5.11: Abstraction levels of the controller software

2390 to several extra functions. These allow the user to download a customised bitfile to
2391 the FPGA, access the I/O registers and use the USB data transfer.

2392 5.7.1 Software

2393 The software has been designed in C++ in several levels of abstraction. Figure 5.11
2394 shows the structure of the classes. The classes Device, PSA and RawSignalHandler
2395 are there to make it easier to read and understand the controller code. In principle the
2396 PSfunctions can also be accessed directly by the controller, but for this the instruction
2397 sequences must be well known and understood.

2398 5.7.2 Data readout

2399 The device records the data in two forms - as signal waveforms and as histograms
2400 of analysed pulse parameters. Both are available upon request from the controller.
2401 Only one of the two can be transferred via the USB line at a time.

2402 The waveforms are saved into a FIFO buffer, which can hold up to 64 pulses of the
2403 length of ~ 500 samples. The data format for each pulse is such that it starts with a
2404 header containing the pulse timestamp and the sequential number, continues with the
2405 data samples and ends with a header containing all the measured parameters (width,
2406 amplitude, area, falling slope and form factor). When the FIFO is full, it issues a
2407 flag, which tells the controller that the data buffer is ready for readout.

2408 The histograms are implemented into the FPGA's Block RAM. Their size ranges
2409 from 256 to 4096 bins (an 8-bit or a 12-bit histogram, respectively), depending on the
2410 required histogram resolution. For instance, the width parameter is measured with a

5.8. PERFORMANCE RESULTS

2411 0.2 ns resolution; the expected maximum pulse width is less than 20 ns. This yields
2412 the maximum range of 100 bins, making an 8-bit histogram sufficiently large. The
2413 same reasoning is applied to the amplitude measurement. In this case the maximum
2414 range is defined by the 8-bit resolution of the ADC. The area measurement, however,
2415 yields higher values and can therefore have a more refined binning (12-bit). Finally,
2416 a single 12-bit 2D histogram is included, with 6 bits for every axis. It is used as an
2417 online scatter plot for comparing one measured parameter to another. An example
2418 for it is a comparison of the width against the area, which can help the user determine
2419 the cuts that need to be applied to the measurement.

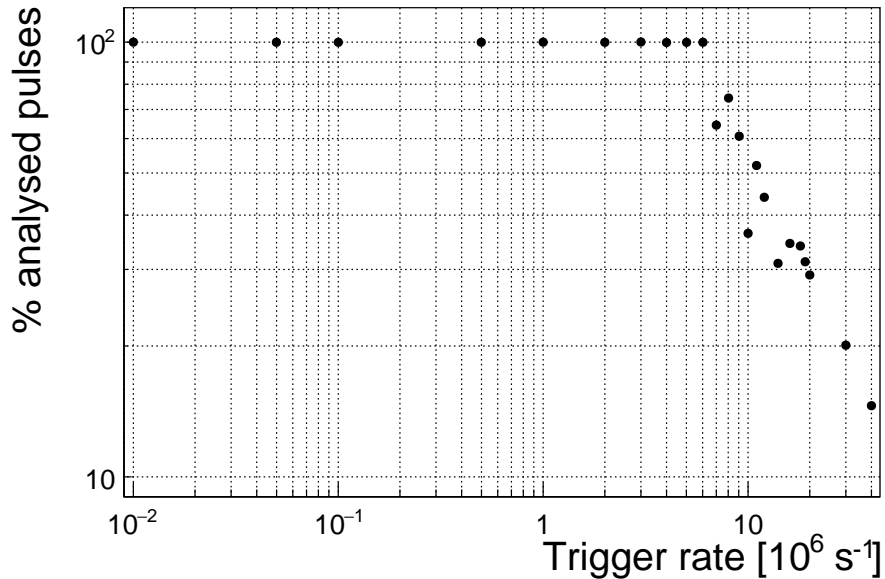
2420 5.8 Performance results

2421 The device has been tested in the lab using a pulse generator as well as several radioac-
2422 tive sources. The results show that: 1) the amplitude, area and width measurement
2423 are linear across all input ranges, 2) the highest rate of the PSA algorithm is $\sim 5 \times 10^6$
2424 pulses per second and 3) the lowest SNR where the algorithm still functions is ~ 5 .

2425 **Trigger rate** A pulse generator was used to verify the highest achievable rate at
2426 which the PSA still analyses every incoming pulse. The final state machine imple-
2427 mented in the pulse analysis module prevents the triggering block from issuing a
2428 trigger due to an incoming pulse if the previous analysis is still in ongoing. Given
2429 that all the pulses were of the same length, the analysis duration was always the
2430 same. When the time between the incoming pulses was shorter than the time of the
2431 analysis, the pulses were not analysed. Figure 5.12 shows the sharp decline in the
2432 percentage of the analysed pulses when reaching the rate of 5 MHz. Therefore the
2433 overall analysis duration for a 10 ns pulse is approximately 200 ns.

2434 **Linearity** A pulse generator was used to verify the linearity of the measurements
2435 across all input ranges. Pulse width and amplitude were varied and measured both
2436 with the oscilloscope and the PSA to check for non-linearities or inconsistencies in the
2437 PSA measurements. The resulting plots in figures ?? and 5.13c show that the PSA
2438 measurements agree well with those from the oscilloscope. The major inconsistency
2439 is observed in the lower range of the plots. It stems from the fact that the bandwidth
2440 limit of the PSA is lower than that of the oscilloscope, which affects the pulse shape.
2441 Effectively, the PSA cannot measure the rectangular pulses of the width smaller than
2442 2 ns.

2443 **Stability** The input pulse signal was superimposed with white noise generated by
2444 a noise generator with a variable gain. The mixed signal yielded pulses with an
2445 SNR ranging from 5 (very noisy) to 100 (noise negligible). The PSA then performed
2446 the pulse parametrisation at different SNRs. The resulting plots in figures 5.13b,
2447 5.13d and 5.13e show that the pulse width measurement is stable even for low SNR
2448 whereas the amplitude measurement is affected significantly. This stems from the
2449 analysis taking the highest sample as the pulse's amplitude. The area measurement,



5.8. PERFORMANCE RESULTS

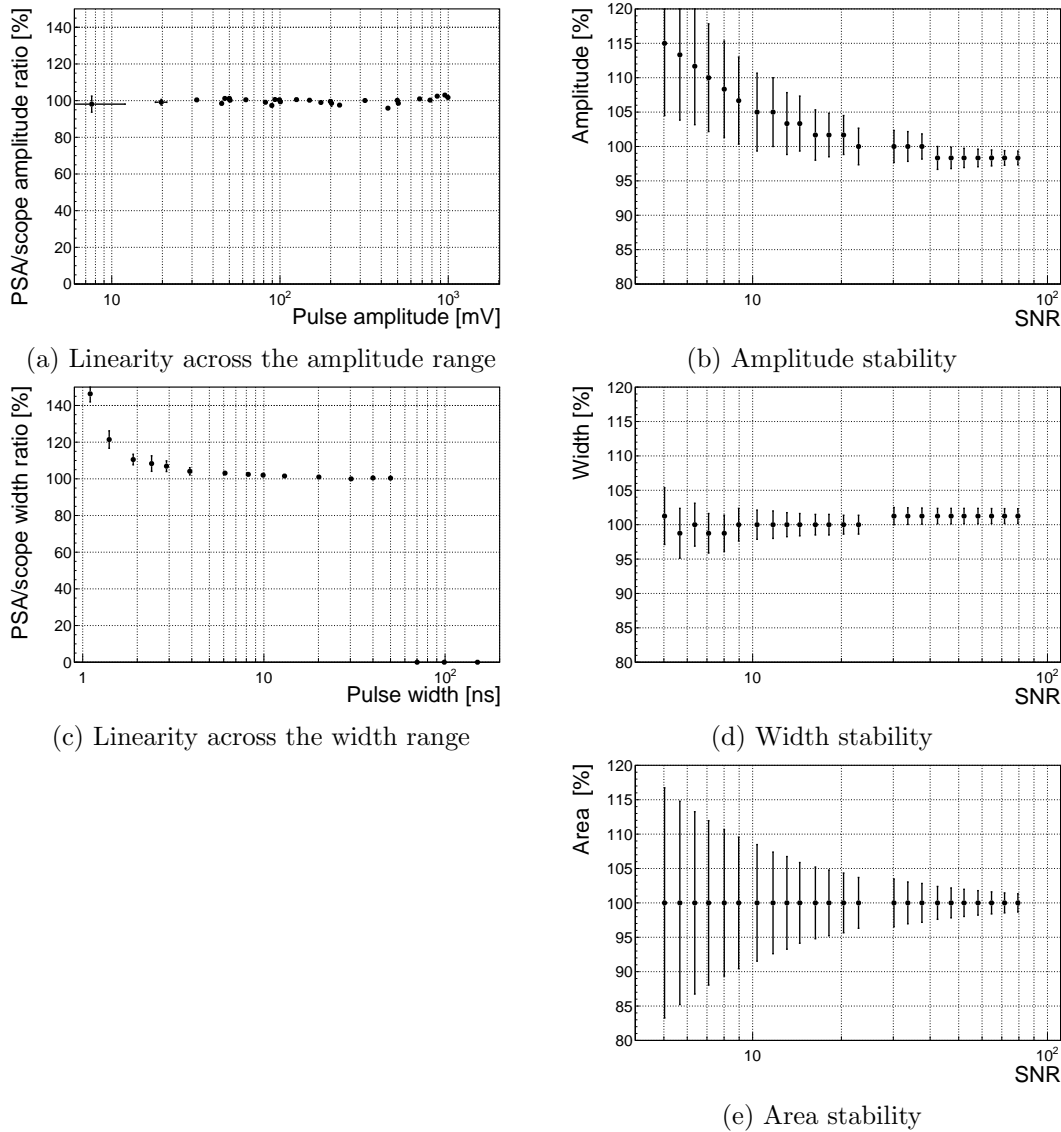


Figure 5.13: These diagrams show the linearity of the measurements and their stability with respect to analog noise.

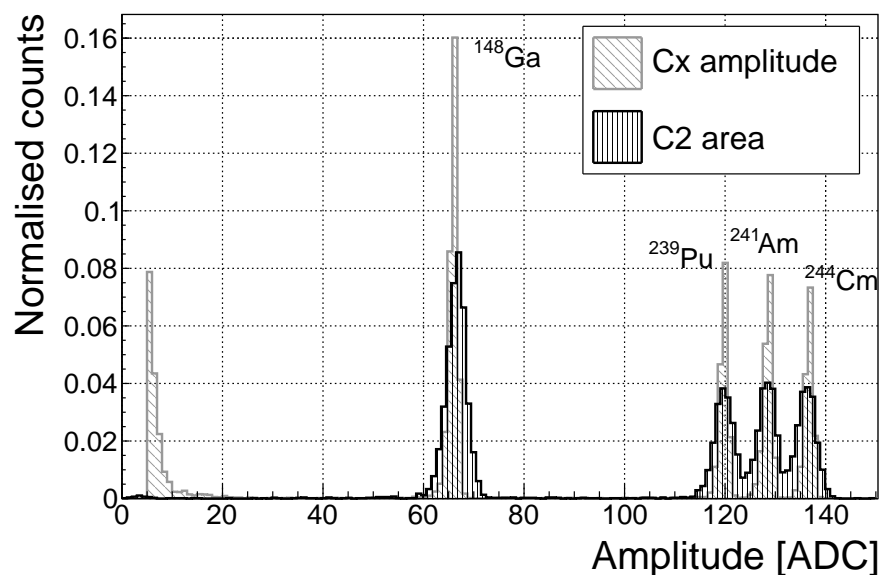


Figure 5.14: Spectrum of a $^{148}\text{Gd}^{239}\text{Pu}^{241}\text{Am}^{244}\text{Cm}$ source using a Cx and a C2 amplifier

5.9. SOURCE CALIBRATION

2465 5.9 Source calibration

2466 The operation of the pulse shape analysis has been tested using several radioactive
 2467 sources. In particular, an α , a β and a γ source have been used. Each source has
 2468 been placed on top of the diamond detector and left for a predefined time depending
 2469 on its activity. Table 5.2 shows the sources used, the time of exposure and their rate
 2470 during this time. The data for the α source have been taken for both polarities. In
 2471 addition, a long run with an α source with a sheet of paper in between the source
 2472 and the diamond has been taken. The paper stops the α particles but lets through
 2473 the photons, which helps to estimate the background photon radiation of the source.

Run	Source	Radiation	Energy [MeV]	Time [h]	Triggers	Rate [s^{-1}]	Bias [V]
2474	1 $^{241}\text{Am}^*$	α	5.5	60	958	4.4e-3	500
	2 ^{241}Am	α	5.5	17	10558	0.17	500
	3 ^{241}Am	α	5.5	18	11454	0.18	-500
	4 ^{90}Sr	β	2.3	0.42	1.07e6	1000	500
	5 ^{60}Co	γ	1.3	0.28	1.34e6	3300	500
	6 $^{239}\text{Pu Be}$	n	1-10	2.5	1.5e6	230	500

2475 Table 5.2: Measurements carried out at Atominstitut

2476 The pulses acquired during the data taking are shown in persistence plots in
 2477 figures 5.15. Figure 5.15a showing the ^{241}Am source background reveals that the
 2478 diamond detector had been contaminated, probably with chipped-off grains of the
 2479 unsealed source. This stems from the fact that α pulses are recorded despite having
 2480 a sheet of paper, which stops all the particles emitted by the source. However, the
 2481 number of α hits due to contamination is negligible - an estimated 1 h^{-1} . Another
 2482 point worth noting is the falling slope of the rectangular pulse in figure 5.15c. This
 2483 stems from the space charge that had built up during the neutron irradiation and is
 2484 discussed in section ???. Finally, figure 5.15f shows that the neutron source causes
 2485 the widest variety of pulse shapes - triangular and rectangular as well as those in
 2486 between. Pulse shapes caused by neutrons are described in detail in [44, 43].

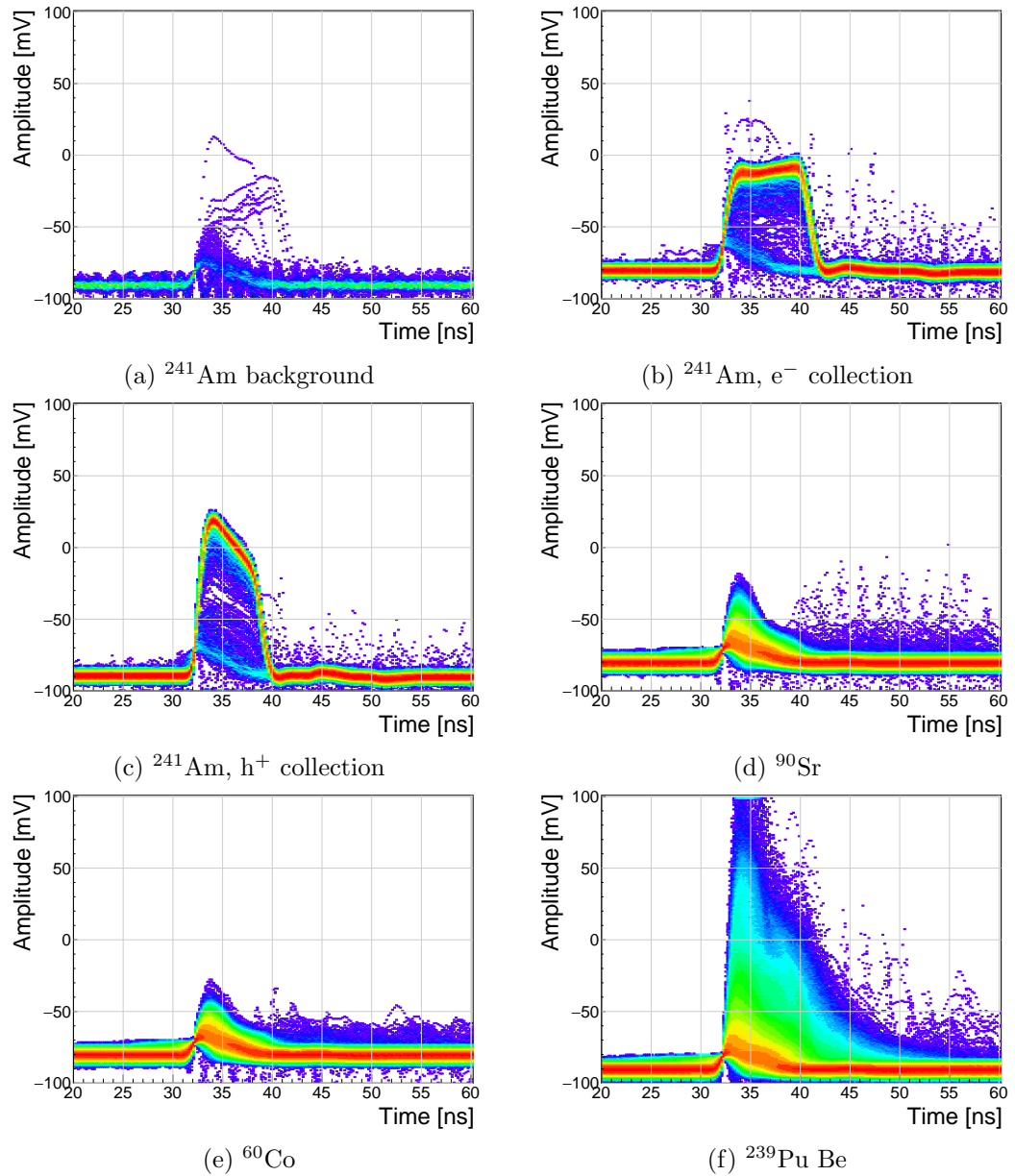


Figure 5.15: Accumulated pulses for all runs

5.9. SOURCE CALIBRATION

5.9.1 Source measurements – scatter plots

An online pulse shape analysis has been run on all the above mentioned data sets. The parameters of the pulses are plotted in 2D histograms - in form of scatter plots. The aim is to find a way to distinguish between the various types of radiation in order to only select the spectrum of a single type of particles from a spectrum of a mixed source. The energy spectrum is directly proportional to the measured area of the current pulses, therefore all the parameters are plotted against the pulse area. The parameters used are:

- FWHM
- Base width
- Amplitude
- Amplitude × Base width
- Base width – FWHM
- Falling slope

Every individual parameter can be attributed a set of qualifiers with which a certain part of the distribution can be rejected. There are two ways to apply the qualifiers. One is to set the minimum and maximum value for a specific parameter. The accepted pulses are those in between these two values. The minimum and the maximum qualifier are marked with a blue and a red line in the subsequent scatter plots. The second way is to apply a linear cut to the distribution in the scatter plot. The user can choose the slope of the line and to accept either the pulses above or below the line. The colour of the line is blue if the part above the line is accepted and red if opposite. Currently two scatter plots have this option implemented: area vs amplitude and area vs amplitude×base width. The latter represents the Form Factor, which is discussed in section 5.6.2.

The sets of plots in figures 5.16, 5.17, 5.19 and 5.20 show the above listed parameters plotted against the pulse area for ^{241}Am background, electrons and holes, ^{90}Sr and ^{64}Co source, respectively. Any distinguishable difference between the plots of two sources would suggest that that particular parameter can be used to distinguish one type radiation from the other. For the most part the photons are considered the rejected pulses (greyscale colour palette) whereas α particles or neutrons are accepted (yellow colour palette). In special cases only a certain types of neutron interactions are accepted (see section 5.10).

5.9.1.1 ^{241}Am source

The source emits α particles at ~ 5.5 MeV and photons with a range of energies. Due to the losses in the air and the electrode the measured α energy varies – between ~ 5 MeV down to 1 MeV.

Figures 5.16 and 5.17 show the pulse area distribution with respect to the aforementioned parameters, for electrons and holes respectively. Focusing on the top left plot in figure 5.16, a distinctive horizontal stripe appears at a width of 9 ns, ranging from 100 up to 630 pVs. This is the aforementioned spread of α energies. The shape of the pulse from this type of radiation retains the width even at smaller energies. Only its amplitude is decreased. This is because the free charge carriers in the diamond are traveling with the same speed in all cases, inducing rectangular pulses of the same widths.

The other cluster in the [area, FWHM] phase space comes from the background photons. The two clusters are far apart from one another with no overlap. It is therefore straightforward to define a cut in the FWHM to distinguish between the α and γ entries. This is done by means of the minimum and maximum FWHM constant qualifier, which marked red and blue in the [area, FWHM] subfigure.

The [area, amplitude] subfigure also reveals two distinguishable clusters, which can be segregated using a linear qualifier. The angle of the α stripes in the [area, amplitude] subplots is significantly smaller than that of the photon stripe. The separation is much less pronounced in the other subfigures.

There is a third barely distinguishable island visible in the top two plots, both area and width values close to zero. This island is formed by noise, which triggered the analysis.

The situation is similar when inverting the bias voltage and collecting holes (see figure 5.17). Here, however, the two clusters are much closer together even in the [area, FWHM] subfigure. This makes it more difficult to define a clear border between the two. The other five qualifiers are in this case less important than the FWHM. Nevertheless, it can be deduced from the plots that the difference BW-FWHM must be below 4 ns.

The slope is dependent of the amplitude, which can be seen in the bottom right plot, making it an unreliable qualifier in the lower area range. The amplitude, scaling with area, makes a distinguishable straight line in the middle left subfigure.

The amplitude increase with area in the [area, amplitude] subfigure is similar for photons and α particles. Therefore a linear qualifier can not be used to distinguish α radiation from γ radiation when measuring holes.

Figures 5.18a and 5.18b show a one-dimensional area distribution of the acquired data for electron and hole collection. The blue histogram represents all collected data whereas the red one marks the data whereby the pulse parameters are within the qualifiers. In both figures the α peak at 600 pVs is clearly visible, followed by a γ quasi-Landau distribution with an MPV of \sim 70 pVs and a noise peak at the very left of the area distribution. These two contributions have been rejected by the FWHM qualifier.

5.9. SOURCE CALIBRATION

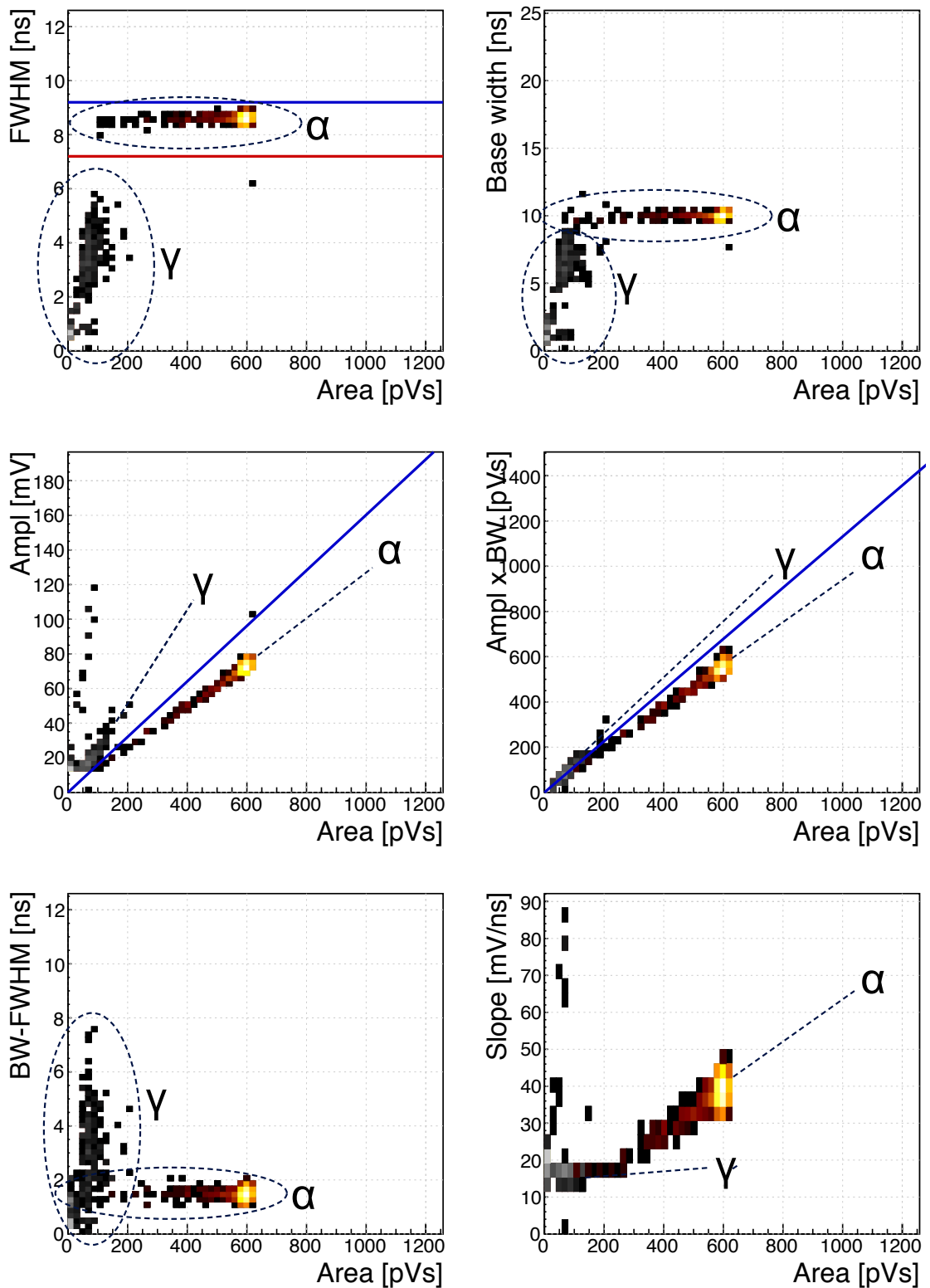


Figure 5.16: ^{241}Am , e^- collection. Qualifier: FWHM. Optional qualifiers: Amplitude, Form Factor.

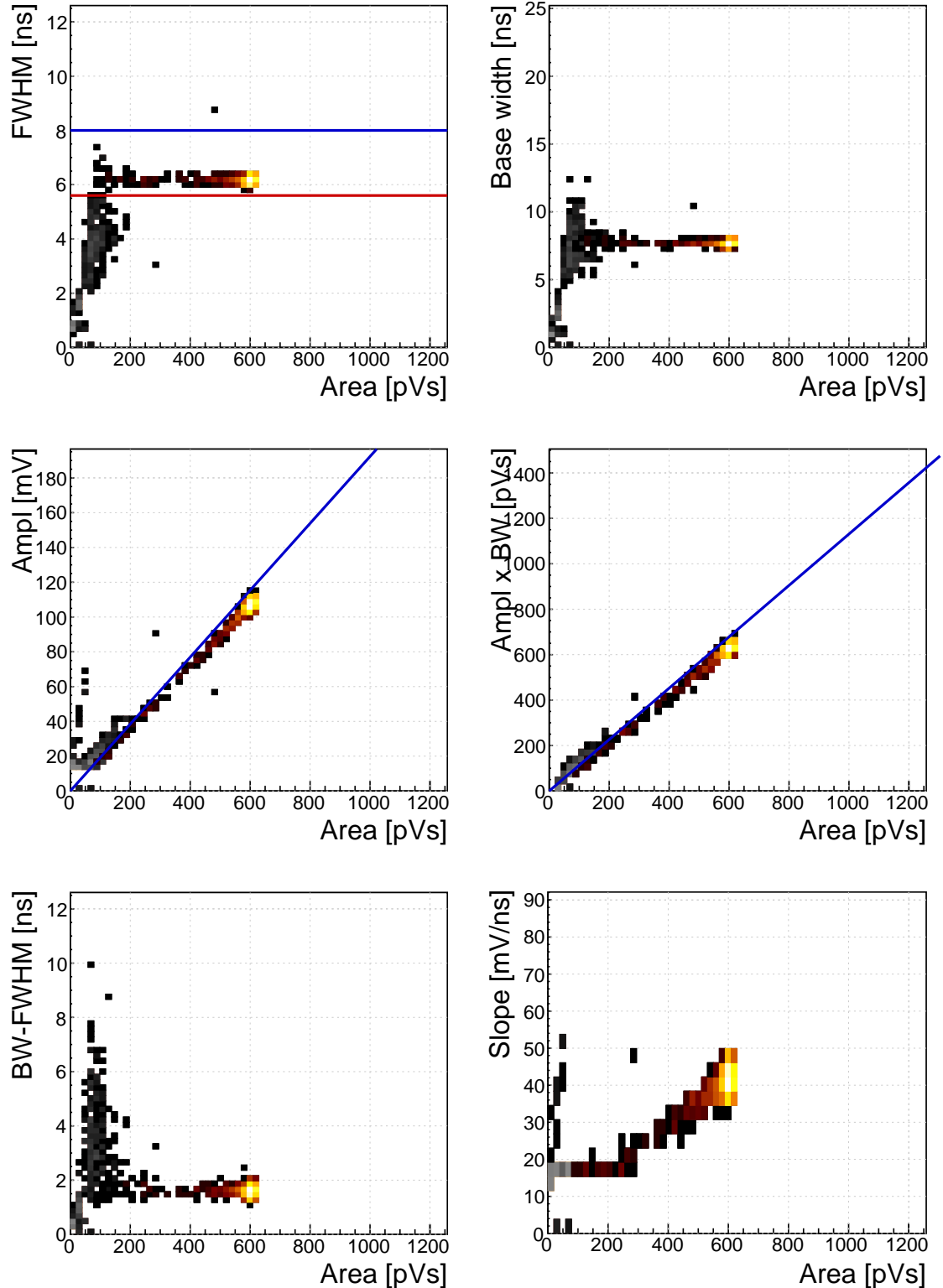
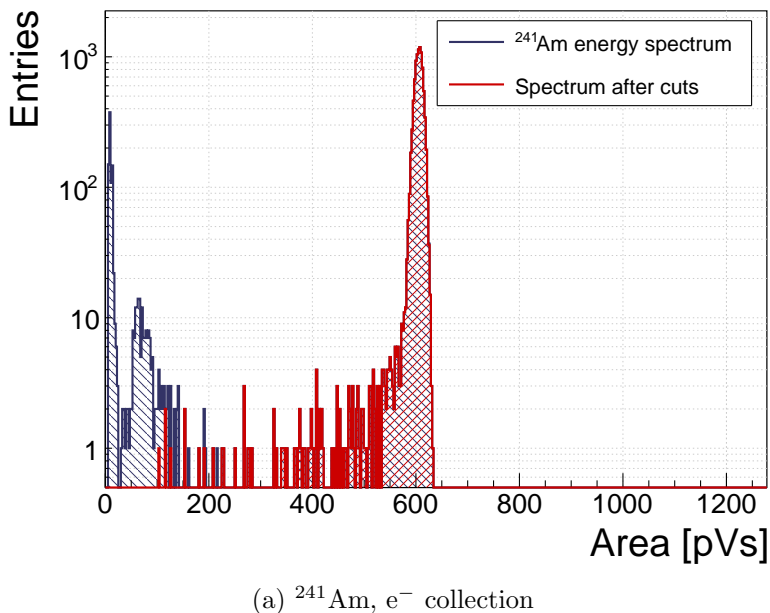
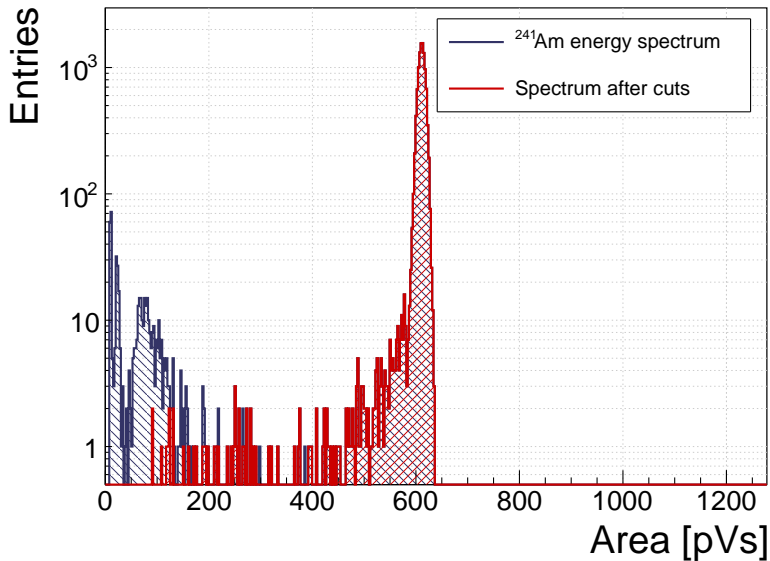


Figure 5.17: ^{241}Am , h^+ collection. Qualifier: FWHM.

5.9. SOURCE CALIBRATION



(a) $^{241}\text{Am}, e^-$ collection



(b) $^{241}\text{Am}, h^+$ collection

Figure 5.18: ^{241}Am area histograms for electron and hole collection.

2563 **5.9.1.2 ^{90}Sr and ^{60}Co source**

2564 The phase space of the ^{90}Sr source overlaps entirely with that of the ^{60}Co source (see
2565 figures 5.19 and 5.20). This renders it virtually impossible to distinguish between
2566 photons and electrons (MIPs). Comparing the [area, FWHM] phase space of the
2567 photons and alphas and the high reach of the former, the electron collection of the
2568 alphas would need to be used to distinguish between the two types of particles.

2569 The one-dimensional histograms in figure 5.21 show a quasi-Landau distribution
2570 with the MPV at ~ 70 pVs, which is in agreement with the background γ radiation
2571 emitted by the ^{241}Am source (see figure 5.18 in the previous subsection). This is
2572 however not a pure Landau distribution. Relative to the 600 pVs α peak, the expected
2573 MPV of MIPs would be ~ 30 pVs, which is not the case in these distributions. This
2574 is because the PSA device is a self-triggering system, which cuts the lower energetic
2575 particles with the trigger threshold. The resulting distribution is therefore only the
2576 top portion of the real Landau distribution. Unfortunately this is the limitation of
2577 the device, governed by the analog noise of the current pre-amplifier.

5.9. SOURCE CALIBRATION

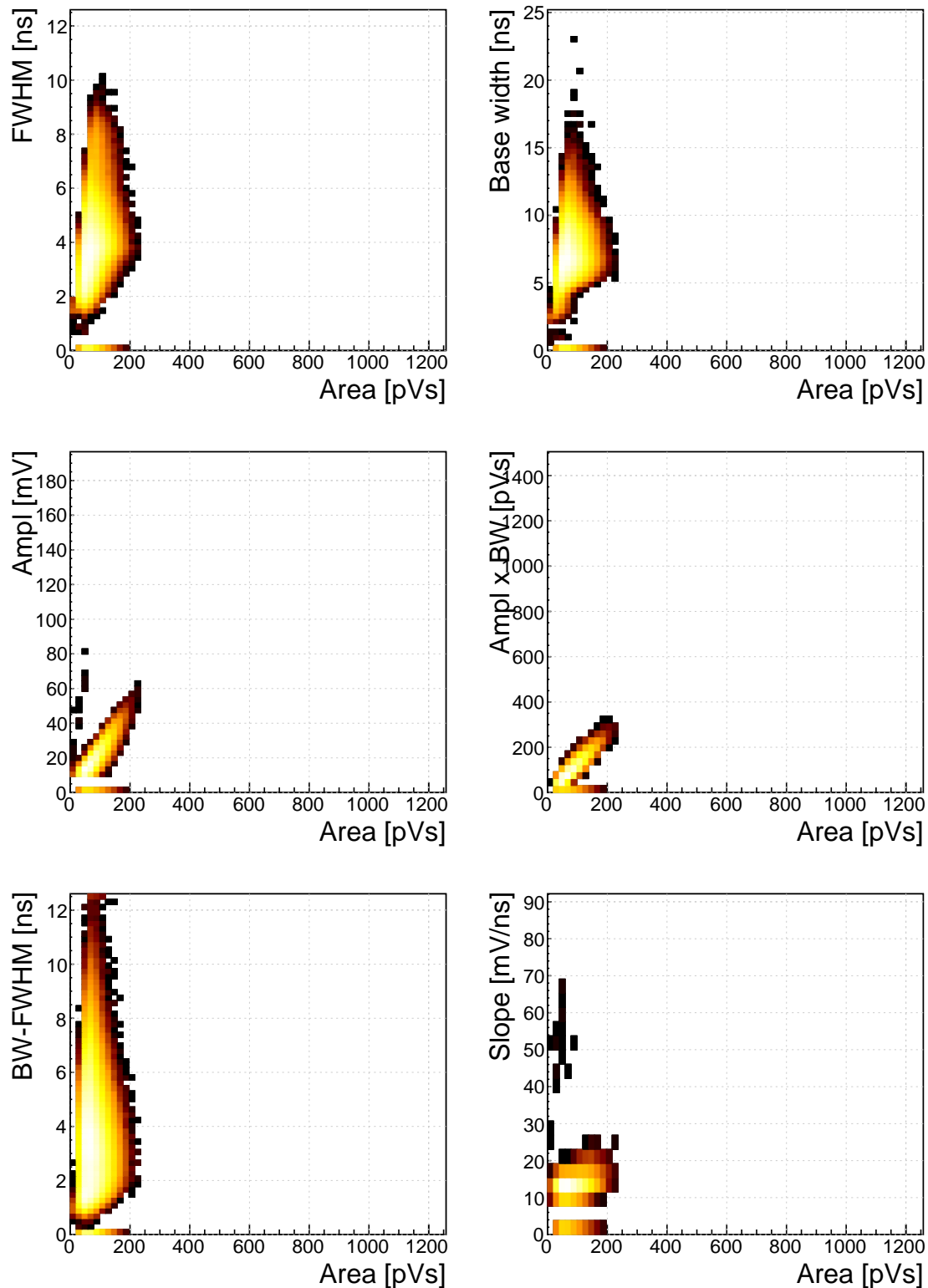


Figure 5.19: ^{90}Sr scatter plots

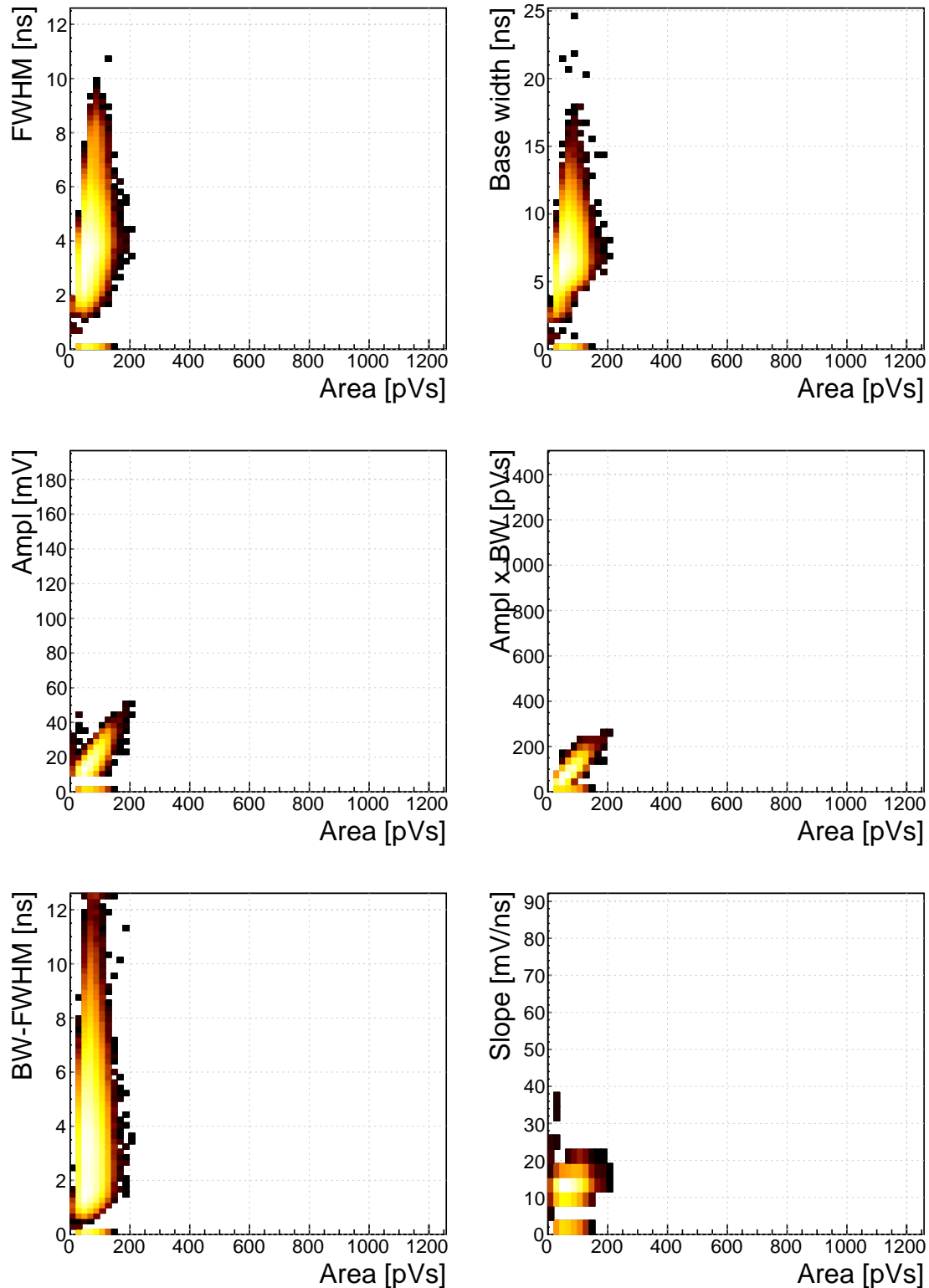


Figure 5.20: ^{60}Co scatter plots

5.9. SOURCE CALIBRATION

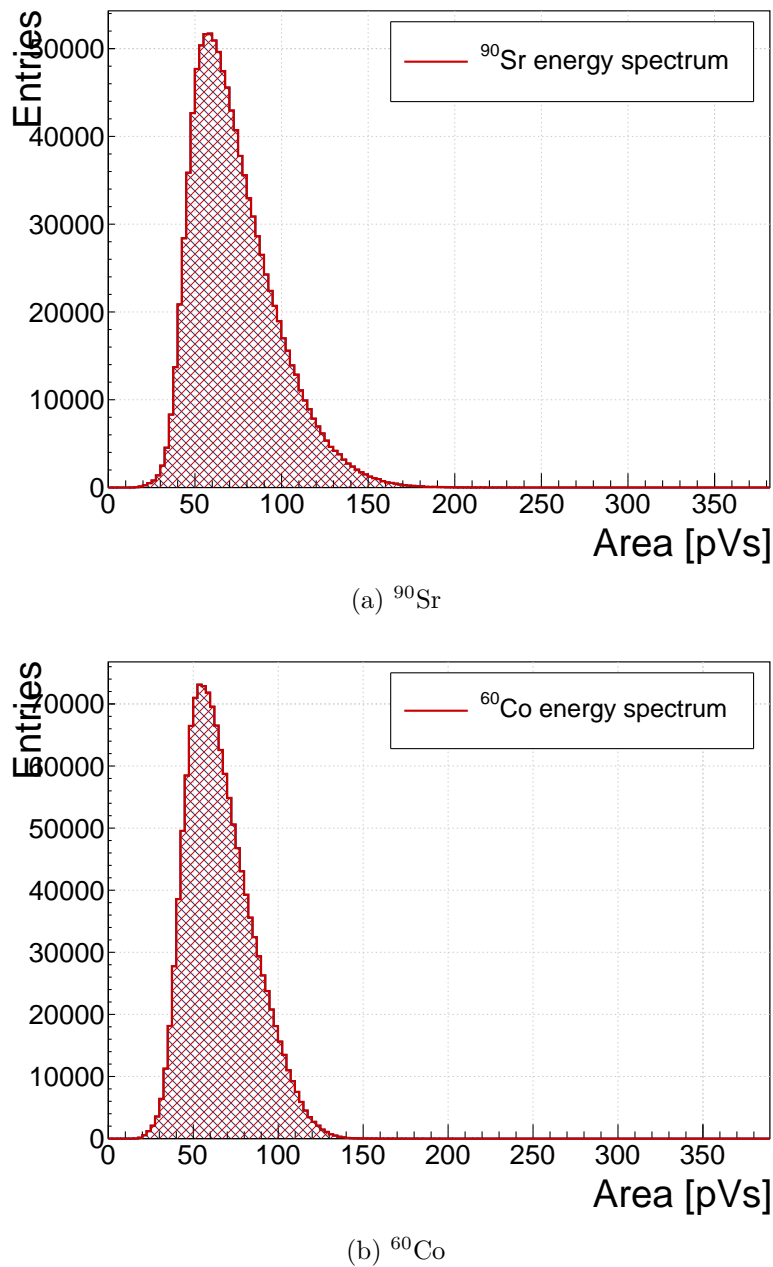


Figure 5.21: Energy distributions for γ and β particles.

2578 5.10 Applications in neutron instrumentation

2579 The real-time pulse shape analysis procedure can be applied to more complex systems.
2580 This section includes three applications where the PSA has been applied.

2581 Semiconductor-based neutron detectors provide a compact technology for neutron
2582 detection. However, the cross section of a neutron with the diamond bulk is very low,
2583 since it only interacts with the core of the atom. Diamond is mainly used to detect
2584 charged particles and photons.

2585 Research neutron reactors radiate a mix of particles, apart from neutrons also
2586 photons. The photons are considered a background radiation, concealing the neutron
2587 spectrum. When measured with diamond, the signal from neutrons is difficult to
2588 distinguish from the photon spectrum. In addition, low energy neutrons do not cause
2589 nuclear reactions in the bulk. All in all, the neutron measurements in a reactor present
2590 a challenge with diamond. However, by means of the PSA, the neutron signal can be
2591 discriminated from the photon background to some extent. The following two cases
2592 show how measurements of fast (n^+) and thermal (n^-) neutrons have been carried
2593 out by making use of the PSA.

2594 Note the changing scale on the X axis in the figures.

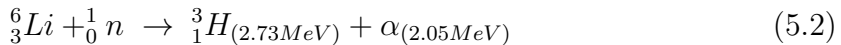
2595 5.10.1 Thermal neutron flux monitoring

2596 Research neutron reactors like TRIGA MARK II [?] at Atominstitut [?] in Vienna
2597 are capable of emitting neutrons at a wide range of energies. The neutron flux is
2598 proportional to the current power of the reactor. It is therefore instrumental to
2599 monitor the neutron flux to make sure that the reactor operation is within the specified
2600 limits. However, the byproduct of the radioactive decays in the core is γ radiation,
2601 which has an energy range that overlaps with that of neutrons, making it difficult to
2602 measure the neutron flux. This is where PSA and diamond detectors come into play.
2603 This section describes the application of thermal neutron flux monitoring by means
2604 of the PSA.

2605 Thermal neutrons do not interact with the diamond bulk due to their low ki-
2606 netic energy (of the order of 0.012 eV). Hence a converter foil has to be added to
2607 produce second order effects. Incoming neutrons interact with the foil, producing
2608 a set of secondary particles. These can then be detected upon hitting the detector
2609 bulk. Common neutron interactions that are used in thermal neutron detection are
2610 $^{10}\text{B}(\text{n},\alpha)^7\text{Li}$ reaction and $^6\text{Li}(\text{n},\alpha)^3\text{H}$ reaction (α stands for ^4_2He , see equation 5.2).
2611 The focus in this section is on the latter. With a foil installed, there are several
2612 possibilities for neutrons to interact with the detector system. Each of these inter-
2613 actions ionises the diamond bulk in its own way, resulting in a specific shape of the
2614 current pulse. A neutron can: 1) interact with the foil, producing an α and a ^3H , 2)
2615 interact with a carbon atom in the lattice, producing an α and a γ or even three α .
2616 The thermal neutrons do not have enough kinetic energy to interact with the lattice,

5.10. APPLICATIONS IN NEUTRON INSTRUMENTATION

2617 therefore the focus will be on case (1), the equation for this reaction is the following:



2618 The particles in the first case are produced outside the diamond and get stopped
2619 immediately upon hitting the sensor. The resulting pulses for both particles have a
2620 rectangular shape of the same width, because the carriers drift with the same speed
2621 in both cases. The difference is in the number of free carriers produced - the tritium
2622 creates more (proportional to the deposited energy), which in turn induces a higher
2623 pulse.

2624 TRIGA MARK II neutron reactor emits large amounts of γ radiation in the
2625 energy range up to 3 MeV. This already affects the measurements of α particles, the
2626 energy of which peaks at 2.05 MeV in the case of 6Li converter foil. However, γ
2627 background radiation can be suppressed by discriminating current pulses of photons
2628 from those induced by α particles. This idea has already been implemented in offline
2629 analysis in [29, 24]. The results show that the background photons can be subtracted
2630 successfully. In order to make sure that every single incident thermal neutron has
2631 been accounted for, the algorithm has been ported to FPGA where it detects and
2632 analyses particles in real time.

2633 5.10.1.1 Measurements

2634 ROSY readout device with the implemented Pulse Shape Analysis was put to a test
2635 at Atominstut in Vienna. Their TRIGA neutron reactor is capable of delivering
2636 thermal neutrons with the energy 0.012 eV at a rate of $10^3 n \text{ cm}^{-2} s^{-1}$, with a
2637 considerable γ background.

2638 First, the device was calibrated using an unsealed monochromatic ${}^{241}Am$ source
2639 with the emitted particle energy $E_\alpha = 5.12MeV$ (taking into account the losses in
2640 the air). Then the diamond detector was exposed to the beam. Secondary reaction
2641 products (α and 3H particles), created by neutrons hitting the converter foil, were
2642 detected by the diamond sensor, together with a significant photon background. Then
2643 the pulse identification algorithm was applied to discriminate between the reaction
2644 products and the photons.

2645 The main parts of the detector are an sCVD diamond sensor sized $4.7 \times 4.7 \text{ cm}^2$
2646 and a $1.8 \mu\text{m}$ thick LiF converter foil, both embedded in an RF-tight PCB. The
2647 diamond sensor is biased with a bias voltage of $1 \text{ V}/\mu\text{m}$ and capacitively coupled to
2648 CIVIDEC's C2 40 dB wide bandwidth current preamplifier. A 5 m long BNC cable
2649 connects the preamplifier to CIVIDEC ROSY box. The detector assembly together
2650 with the preamplifier has to be placed in front of an exit hole of the reactor.

2651 Note: this data set has been taken with an older version of the firmware, which
2652 only measured a limited number of pulse parameters.

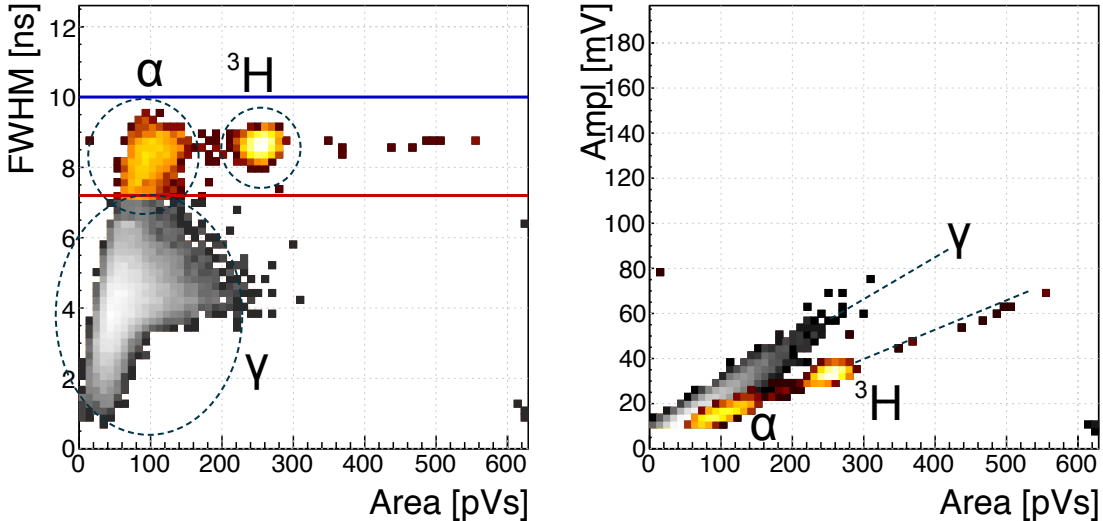


Figure 5.22: Thermal neutrons, photons. Qualifier: FWHM.

2653 5.10.1.2 Results and discussion

2654 The data collected by the PSA show a high flux of photons, which covers a wide area
 2655 range. The ^3He peak is clearly visible and has almost no overlap with the photon
 2656 cluster. The α cluster has a much lower energy and is in the same energy range
 2657 as the photons. However, if a FWHM parameter is observed, a distinction between
 2658 the photons and the α can be seen. By setting a qualifier to the right value, the
 2659 photon background is cut away, leaving only the thermal neutron decay products in
 2660 the data set (see figure 5.22). The resulting one-dimensional area histogram before
 2661 and after applied cuts is shown in figure 5.23. The blue distribution is the mixed field
 2662 of background photons, tritium and α particles. The latter are completely hidden in
 2663 the γ energy distribution. After applied qualifiers the α peak suddenly appears.

2664 5.10.1.3 Conclusion

2665 By applying the FWHM qualifier to the acquired data from the TRIGA neutron reactor,
 2666 the α and tritium particles can be identified and separated from the γ background.
 2667 The resulting cleaned data can be used to correctly count the thermal neutrons de-
 2668 tected by the diamond sensor.

2669 5.10.2 Fusion power monitoring

2670 Many research collaborations around the world are trying to develop a functional
 2671 fusion reactor, which could provide a cleaner energy source. One of them is ITER [8],
 2672 a research fusion reactor being built in France. The idea behind it is to harvest
 2673 energy from the fusion of light atoms into a heavier one. For ITER the fuel chosen

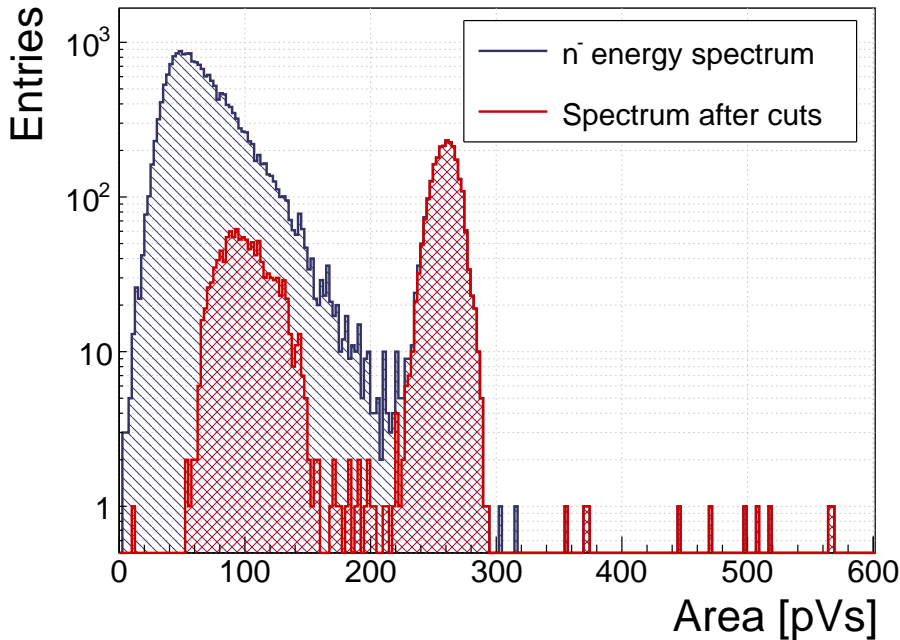


Figure 5.23: Energy spectrum after applied qualifiers reveals the tritium and α peak

2674 is a mixture of deuterium and tritium, which fuse into a helium atom at extremely
 2675 high temperatures (plasma), emitting a highly energetic neutron as a byproduct. The
 2676 equation is the following:



2677 The α particle immediately deposits its energy within the plasma. The neutron, due
 2678 to its neutral charge, continues its way out of the system where it is stopped. The
 2679 stopping power is converted into energy, which heats the water into steam, which in
 2680 turn spins the turbines, generating electricity.

2681 It is possible to monitor the activity of the reactor by measuring the flux of neu-
 2682 trons emitted. Neutron diagnostics such as neutron cameras, neutron spectrometers
 2683 and neutron flux monitors therefore provide robust measurements of fusion power. A
 2684 high γ background makes it difficult to accurately measure the neutron flux. This is
 2685 a motivation to use a diamond based detector with a real-time PSA algorithm.

2686 The neutrons emitted are 14 MeV mono-energetic fast neutrons. The most ac-
 2687 curate and efficient way to detect them with a diamond detector is by means of a
 2688 $C_{12}(n,\alpha)$ reaction with a carbon atom in the ballistic centre [30]. In this region the
 2689 positive and negative charge carriers created by α that start drifting in the opposite
 2690 directions need the same time to reach the opposite electrodes.

2691 **5.10.2.1 Measurements**

2692 The ${}^{239}\text{Pu Be}$ neutron source has been used to simulate the fusion reactor. It emits a
 2693 mixed field of neutrons and photons with a wide range of energies. The neutrons are

2694 rarely detected with diamond – the interactions happen mostly in the electrodes on
2695 either side of the detector. The α particles created by the interactions are detected
2696 by the diamond. Depending on the side of the interaction, the created pulse is either
2697 due to hole– or electron collection. These two interactions make the two distinct lines
2698 in the [area, FWHM] phase space (see figure 5.24, top left plot) at 9 ns and 6 ns.

2699 A very interesting interaction point is the ballistic centre [?] of the diamond. A
2700 ballistic centre is the position from which it takes the holes and the electrons the
2701 same amount of time to drift to the opposite electrodes. In this case the shortest
2702 possible pulse is created. Conversely, to conserve the collected charge and thus the
2703 pulse area, the pulse amplitude must be the highest at the ballistic centre. The entries
2704 in between are created by neutron interactions at random positions in the diamond,
2705 which produce pulses of various shapes.

2706 5.10.2.2 Results and discussion

2707 Coming back to the motivation, the most efficient way of counting the 14 MeV neu-
2708 trons is through the measurement of the neutrons interacting in the ballistic centre [?].
2709 To extract this type of interaction several qualifiers must be used. The first possibility
2710 is the FWHM set to 3–5 ns. However, this time the cuts on the [area, amplitude]
2711 and the [area, amplitude \times base value] phase space are preferred. First, a minimum
2712 constant amplitude qualifier is set to 22 mV (see figure 5.24, middle left plot). Then a
2713 linear amplitude qualifier is set such that only the pulses with the highest amplitude
2714 for every area value are taken. This ensures that the high pulses from the ballistic
2715 centre are chosen. Second, a maximum linear amplitude \times base value qualifier is set
2716 such that only the pulses bearing the closest resemblance to a rectangle are chosen
2717 (see figure 5.24, middle right plot). In this phase space the entries at the bottom of
2718 the distribution are bearing more resemblance to a rectangle whereas those at the top
2719 are more akin to triangles.

2720 The resulting [area, FWHM] subfigure after applied qualifiers highlights the entries
2721 with a FWHM of 4 ns, which is the width of the pulses induced by neutrons interacting
2722 in the ballistic centre. This proves that these combined qualifiers indeed pinpoint
2723 these neutron interactions. The final one-dimensional area/energy distribution of the
2724 neutrons interacting in the ballistic centre is shown in figure 5.25.

2725 The result could be further improved by further constraining the identification,
2726 e.g to define the minimum FWHM constant qualifier and the minimum slope constant
2727 qualifier.

2728 5.10.2.3 Conclusion

2729 By applying the appropriate qualifiers to the data, the neutron interactions in the
2730 ballistic centre can be identified.

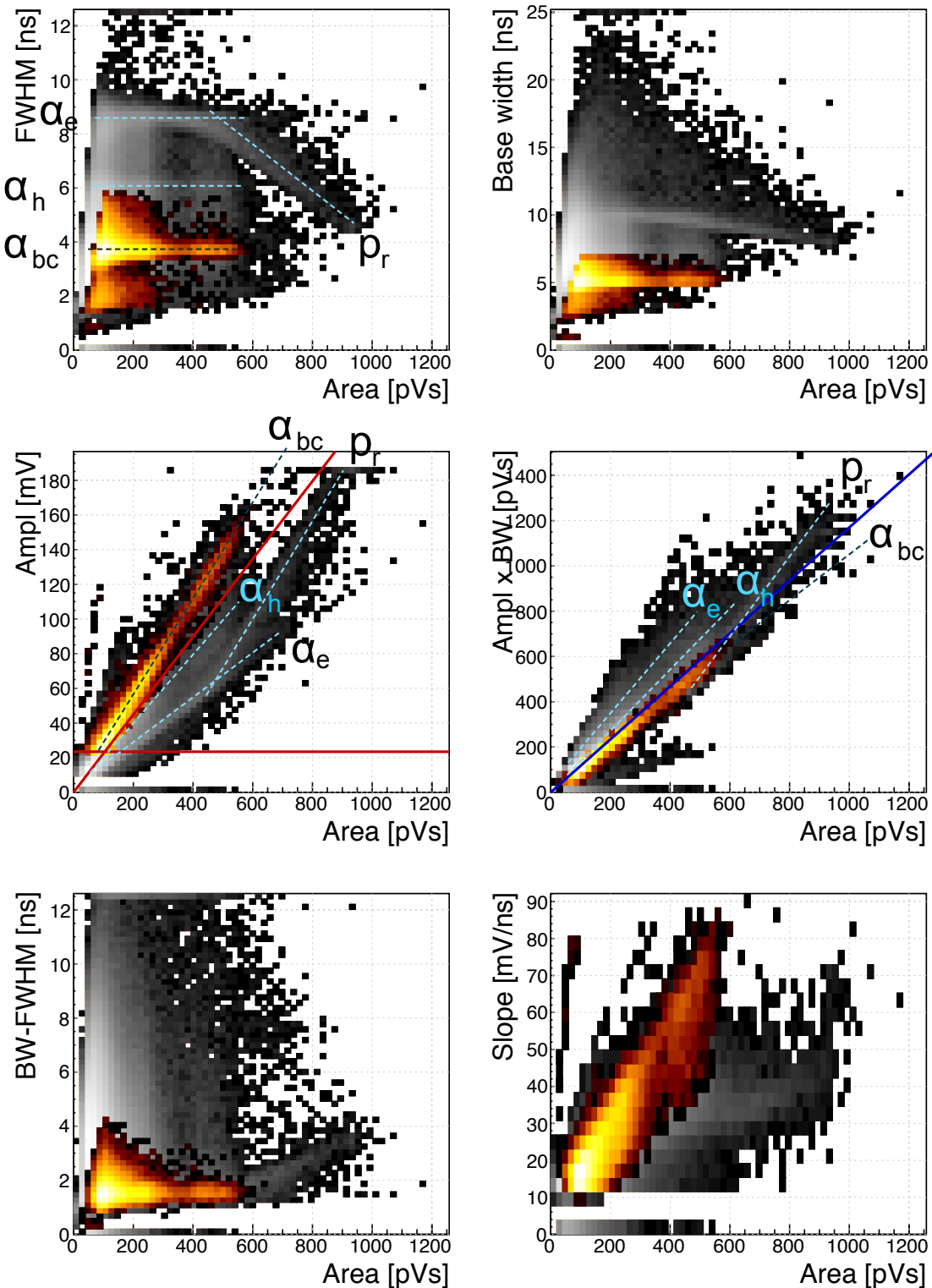


Figure 5.24: $^{239}\text{Pu Be}$. Qualifiers: BW-FWHM, FWHM, Form Factor

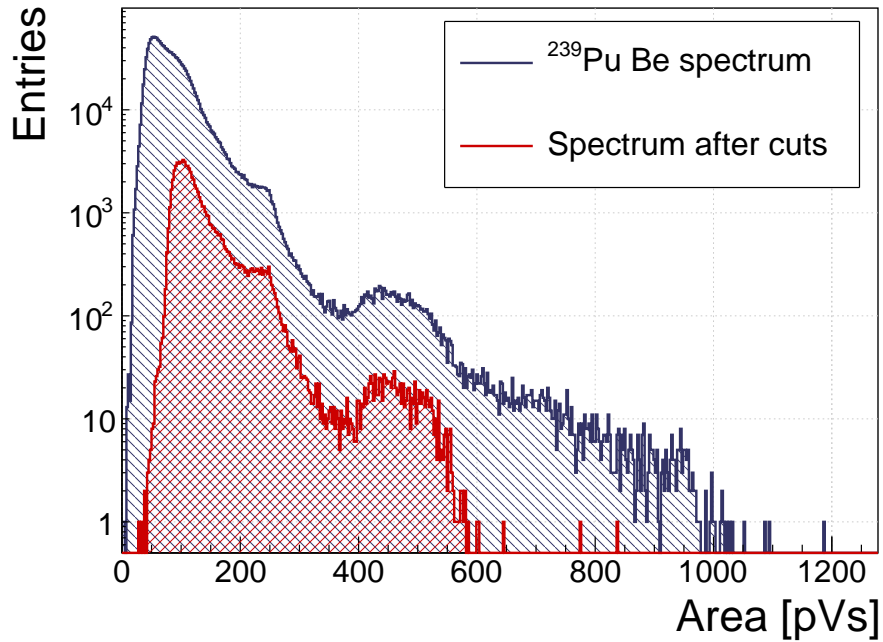


Figure 5.25: ^{239}Pu Be, energy distribution of the neutrons interacting in the ballistic centre.

5.10.3 Fast and thermal neutron monitoring

The CROCUS reactor at EPFL [3] is a research neutron reactor. The research group working on the reactor is interested in measuring neutrons with energies between 1–2 MeV, which is overlapping with the γ background energy range.

The highest output power of the CROCUS reactor is 100 W. Currently there are fission chambers that carry out the neutron counting, which is a measure of the activity of the reactor. The new goal is to measure both neutrons and photons, but separately. The pulse shape analysis is a good solution for this task. For this, a 400 μm thick diamond detector with a specially designed casing was added to measure the activity. The LiF foil was added for conversion of thermal neutrons. The ROSY box with the integrated PSA routine was used for signal analysis.

5.10.3.1 Measurements

At the highest reactor activity the system counts particles at a rate of $\sim 1.5 \times 10^5 \text{ s}^{-1}$. The results from a test run at 10 W output power are shown in figure 5.26. The data include a mixed field consisting of fast neutrons, photons and of α and ^3H particles as products of thermal neutron decay in the LiF foil in front of the detector. The energy deposited in the diamond is not as high as that from the ^{239}Pu Be source. In addition, the analog noise during this measurement is higher than in the previous application. These conditions combined make particle identification at CROCUS a challenging task.

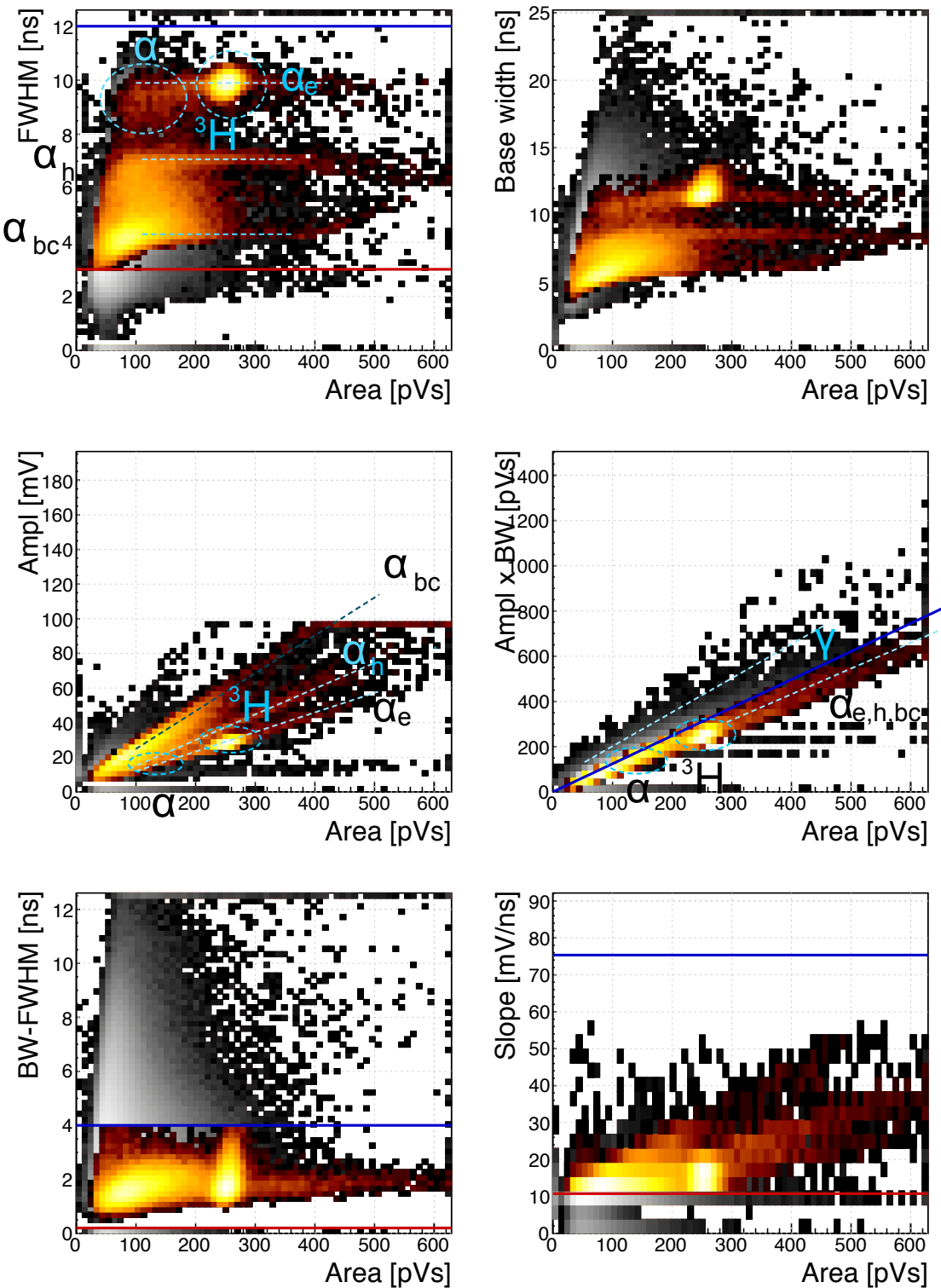


Figure 5.26: Fast neutrons, thermal neutrons, photons. Qualifiers: BW-FWHM, FWHM, Form factor, Slope.

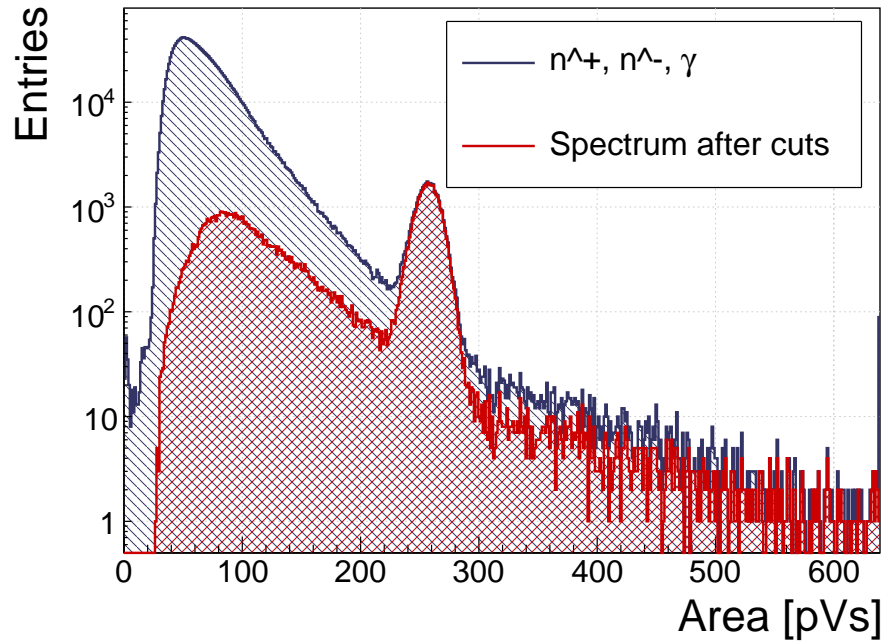


Figure 5.27: Energy spectrum in CROCUS before and after applied qualifiers

2751 5.10.3.2 Results and discussion

2752 The aim of this exercise is to identify both thermal and fast neutrons. For this the
 2753 main qualifier used is the Form Factor - the linear line in the [area, amplitude×base
 2754 value] phase space. Additional FWHM, FWHM-BW and slope constant qualifiers are
 2755 used to clean the outlying entries. The resulting accepted entries in figure 5.26 have
 2756 the distinctive three-line fast neutron signature in the [area, FWHM] subfigure with
 2757 two superimposed islands by the α and ${}^3\text{H}$ cluster produced by thermal neutrons in the
 2758 LiF foil. The γ background is sufficiently suppressed. The resulting one-dimensional
 2759 histogram of the area/energy distribution is shown in figure 5.27.

2760 5.10.3.3 Conclusion

2761 By applying the Form Factor qualifier both fast and thermal neutrons can be identi-
 2762 fied, suppressing the γ background.

2763 **5.11 Conclusion**

2764 This chapter describes a system that can identify the type of radiation in real time.
2765 The system is implemented on an FPGA in a CIVIDEC ROSY box and is used with
2766 diamond detectors. The signal from the diamond sensor is read in and analysed in the
2767 firmware. First the shape of the pulse is parametrised. Then the logic determines the
2768 type of particle according to the user defined cuts. Finally the parameters are written
2769 into a histogram, which is read out by the user. The firmware is designed to carry
2770 out the pulse shape analysis of a single pulse in ~ 200 ns, yielding a maximum pulse
2771 rate of 5×10^6 particles per second. The rate as well as the linearity the measurement
2772 stability with respect to noise have been verified using a pulse generator. Then several
2773 radioactive sources were used to calibrate the device. Finally the system has been set
2774 up in two neutron reactors to test the operation in a mixed field containing thermal
2775 neutrons, fast neutrons and photons. The identification can be optimised using a
2776 combination of qualifiers to achieve the desired effect.

²⁷⁷⁷ Bibliography

- ²⁷⁷⁸ [1] *ASIC*. http://www.embedded-systems-portal.com/CTB/CTB_images/L2/L2 ASIC.jpg.
- ²⁷⁷⁹ [2] *Atominstitut, Technical University of Vienna, Austria*.
²⁷⁸⁰ <http://ati.tuwien.ac.at/startpage/EN/>.
- ²⁷⁸¹ [3] *CROCUS neutron reactor*. <http://lrs.epfl.ch/page-55655-en.html>.
- ²⁷⁸² [4] *DRS4*. <https://www.psi.ch/drs/evaluation-board>.
- ²⁷⁸³ [5] *Element Six*. <http://www.e6.com>.
- ²⁷⁸⁴ [6] *European Centre for Nuclear Research, CERN*. <http://home.cern>.
- ²⁷⁸⁵ [7] *IHa Technologies Pte. Ltd.* <https://www.2atechnologies.com>.
- ²⁷⁸⁶ [8] *ITER fusion reactor*. <https://www.iter.org/>.
- ²⁷⁸⁷ [9] *Neutron Time-of-flight experiment*. <https://ntof-exp.web.cern.ch/ntof-exp/>.
- ²⁷⁸⁸ [10] *Paul Scherrer Institute*. <https://www.psi.ch/>.
- ²⁷⁸⁹ [11] *RD42 collaboration*. <http://rd42.web.cern.ch/rd42/>.
- ²⁷⁹⁰ [12] *TRIGA MARK II neutron reactor*. <http://ati.tuwien.ac.at/reactor/EN/>.
- ²⁷⁹¹ [13] *Xilinx Virtex 5 FPGA*. <http://www.hdl.co.jp/XCM-109/top.560.jpg>.
- ²⁷⁹² [14] *Determination of operational dose equivalent quantities for neutrons*. ICRU,
²⁷⁹³ Washington, DC, 2001.
- ²⁷⁹⁴ [15] General Atomics. *View of the TRIGA reactor*. 2015.
- ²⁷⁹⁵ [16] H. Bethe and J. Ashkin. *Experimental Nuclear Physics*, ed. E. Segre, page 253,
²⁷⁹⁶ 1953.
- ²⁷⁹⁷ [17] W. Blum, W. Riegler, and L. Rolandi. Particle Detection with Drift Chambers,
²⁷⁹⁸ volume 2 of 2. Springer-Verlag, Berlin Heidelberg, 2008.
- ²⁷⁹⁹ [18] Giorgio Brianti. SPS North Experimental Area. Technical Report CERN-SPSC-
²⁸⁰⁰ T-73-8. LabII-EA-Note-73-4, CERN, Geneva, 1973.

BIBLIOGRAPHY

- 2801 [19] Maximilien Brice. *View of the nTOF detector*. Oct 2010.
- 2802 [20] Maximilien Brice. *LHC tunnel*. Jan 2011.
- 2803 [21] P. Carazzetti and H. R. Shea. *Electrical breakdown at low pressure for planar*
2804 *microelectromechanical systems with 10- to 500 μm gaps*. *J. Micro/Nanolith.*
2805 *MEMS MOEMS*, (8(3), 031305), Jul-Sep 2009.
- 2806 [22] Daniel Dominguez. *Standard Model. Le modele standard*. General Photo, Mar
2807 2015.
- 2808 [23] CIVIDEC Instrumentation GmbH. *sCVD diamond sensor*.
2809 <http://www.cividec.at>, 2015.
- 2810 [24] E. Griesmayer, R. Bergmann, H. Böck, M. Cagnazzo, P. Kavrigin, B. Morgenbesser,
2811 and M. Villa. *A Novel Neutron Flux Monitor Based On Diamond*
2812 *Detectors at the Vienna TRIGA Mark II Reactor*. submitted to the proceedings
2813 of ICRR 2015, 2015.
- 2814 [25] E. Griesmayer and B. Dehning. Diamonds for beam instrumentation. *Physics*
2815 *Procedia*, 37:1997 – 2004, 2012. Proceedings of the 2nd International Conference
2816 on Technology and Instrumentation in Particle Physics (TIPP 2011).
- 2817 [26] Moritz Guthoff, Wim de Boer, and Steffen Müller. Simulation of beam induced
2818 lattice defects of diamond detectors using {FLUKA}. *Nuclear Instruments and*
2819 *Methods in Physics Research Section A: Accelerators, Spectrometers, Detectors*
2820 *and Associated Equipment*, 735:223 – 228, 2014.
- 2821 [27] M. Huhtinen. Simulation of non-ionising energy loss and defect formation in
2822 silicon. *Nuclear Instruments and Methods in Physics Research A*, 491:194–215,
2823 September 2002.
- 2824 [28] Hendrik Jansen, Norbert Wermes, and Heinz Pernegger. *Chemical Vapour Deposition*
2825 *Diamond - Charge Carrier Movement at Low Temperatures and Use in*
2826 *Time-Critical Applications*. PhD thesis, Bonn U., Sep 2013. Presented 10 Dec
2827 2013.
- 2828 [29] P. Kavrigin, P. Finocchiaro, E. Griesmayer, E. Jericha, A. Pappalardo, and
2829 C. Weiss. *Pulse-shape analysis for gamma background rejection in thermal*
2830 *neutron radiation using CVD diamond detectors*. *Nuclear Instruments and Methods*
2831 *in Physics Research A*, (795), 2015.
- 2832 [30] P. Kavrigin, E. Griesmayer, F. Belloni, A.J.M. Plompen, P. Schillebeeckx, and
2833 C. Weiss. $^{13}\text{C}(n,\alpha_0)^{10}\text{Be}$ cross section measurement with sCVD diamond detector.
2834 submitted to EPJA, 2016.
- 2835 [31] Claude A. Klein. Radiation-induced energy levels in silicon. *Journal of Applied*
2836 *Physics*, 30(8):1222–1231, 1959.

BIBLIOGRAPHY

- [32] Gregor Kramberger, V. Cindro, A. Gorisek, I. Mandic, M. Mikuz, and M. Zavrtanik. Effects of bias voltage during priming on operation of diamond detectors. *PoS, Vertex2012:013*, 2013.
- [33] W. Y. Liang. Excitons. *Physics Education*, 5:226–228, July 1970.
- [34] Claudia Marcelloni De Oliveira. *IBL installation into the inner detector of the ATLAS Experiment side C. General Photo*, May 2014.
- [35] M. Mikuž. *Diamond sensors for high energy radiation and particle detection*. TIPP, 2011.
- [36] W P C Mills. *The present performance of the SPS*. *IEEE Trans. Nucl. Sci.*, 26(CERN-SPS-AOP-79-9):3176–3178. 3 p, Mar 1979.
- [37] S. F. Novaes. *Standard model: An Introduction*. In *Particles and fields. Proceedings, 10th Jorge Andre Swieca Summer School, Sao Paulo, Brazil, February 6-12, 1999*, 1999.
- [38] Joao Pequenao. *Computer generated image of the whole ATLAS detector*. Mar 2008.
- [39] Heinz Pernegger. *The Pixel Detector of the ATLAS Experiment for LHC Run-2*. Technical Report ATL-INDET-PROC-2015-001, CERN, Geneva, Feb 2015.
- [40] S. Ramo. *Currents Induced by Electron Motion*. *Proceedings of the IRE*, 27:584–585, 1939.
- [41] V. Sarin. *Comprehensive Hard Materials*. Elsevier Science, 2014. p. 411.
- [42] W. Shockley. *Currents to Conductors Induced by a Moving Point Charge*. *Journal of applied Physics*, 9:635, 1938.
- [43] C. Weiss. A CVD diamond detector for (n,α) cross-section measurements. PhD thesis, TU Wien, Vienna, 2014.
- [44] C. Weiss, H. Frais-Kölbl, E. Griesmayer, and P. Kavrigin. *Ionization signals of diamond detectors in fast neutron fields. publication in preparation*, 2016.
- [45] J. L. Yarnell, J. L. Warren, and R. G. Wenzel. Lattice vibrations in diamond. *Phys. Rev. Lett.*, 13:13–15, Jul 1964.